GEORG-AUGUST-UNIVERSITÄT GÖTTINGEN

II. Physikalisches Institut

Top Quark Pair Reconstruction in the Electron + Jets Channel with a Kinematic Likelihood Fitter in the ATLAS Experiment

von

Olaf Nackenhorst

In this thesis a kinematic likelihood fitter is presented and applied to the electron + jets channel of the decay of top quark pairs. NLO Monte Carlo data of the ATLAS experiment are used to test the reconstruction performance of the fitter. The kinematic fit leads to high jet-parton assignment efficiencies compared to a random assignment and an improvement in energy reconstruction of the measured objects.

The effect of using more jets than the four with the highest transverse momentum for the top quark pair reconstruction is studied and results in a larger number of correctly reconstructed events and in better reconstructed objects. The fitter is further applied to W + jets background events and the results are compared to the signal reconstruction. The background events show the tendency to mimic the top pair decay topology due to the kinematic fit but are still well discriminated from the signal events.

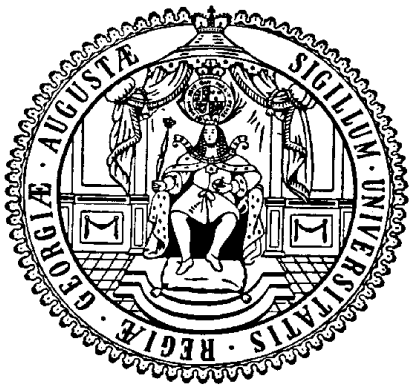

Post address:
Friedrich-Hund-Platz 1
37077 Göttingen
Germany

II.Physik-UniGö-Dipl-2010/04
II. Physikalisches Institut
Georg-August-Universität Göttingen
Juni 2010

GEORG-AUGUST-UNIVERSITÄT

GÖTTINGEN

II. Physikalisches Institut

Top Quark Pair Reconstruction in the Electron + Jets Channel with a Kinematic Likelihood Fitter in the ATLAS Experiment

von

Olaf Nackenhorst

Dieser Forschungsbericht wurde als Diplomarbeit von der Fakultät für Physik der Georg-August-Universität zu Göttingen angenommen.

Angenommen am:	25. Juni 2010
Referent:	Prof. Arnulf Quadt
Korreferent:	Prof. Ariane Frey
Nummer:	II.Physik-UniGö-Dipl-2010/04

Contents

1. Introduction

It is probably the nature of mankind that people are curios about their surroundings and that they try to understand what they observe. The questions arising from this curiosity are sometimes not easily answered and to respond adequately might take centuries or longer. One of the most fundamental ancient questions refers to the structure of matter and its interactions. Philosophers in every epoch speculated about this question and most of their ideas had in common that the underlying theory should be simple and elementary.
Nowadays physicists assume to have a pretty good understanding of what matter is composed of and of the fundamental forces of nature. During the last decades particle physicist have formulated the so called Standard Model of particle physics, which describes three of the four fundamental interactions between all known building blocks of matter - the elementary particles. The dynamics of the particles are obtained for all forces from the same underlying principles. Although not all of the fundamental forces can be described in a unified form, the present Standard Model is a big stepping stone on the way to the old dream of a Theory of Everything. It allows for understanding matter and interactions by reducing most of the known laws to a small set of fundamental particles and their interactions.
Scientists put great effort into confirming the predictions of the Standard Model and huge machines like the Large Hadron Collider have been built for this purpose. built By investigating the collisions of highly relativistic particles with giant detectors particle physicist are able to test the Standard Model and to find indications for physics beyond the Standard Model. The ATLAS detector is one of the general purpose detectors at the Large Hadron Collider. One important process which needs to be identified by the ATLAS detector is the top quark pair decay. The top quark is the heaviest known particle and has special properties which can be used to calibrate the detector or to find hints for physics beyond the Standard Model. The present Standard Model is briefly introduced in chapter 2 with an emphasis placed on top quark physics. Chapter 3 gives an overview of the Large Hadron Collider and the detection of particles with the ATLAS experiment.
The reconstruction of complex processes such as the top quark pair decay is not trivial and sophisticated statistical methods are usually applied. Not only procedures in particle physics, but every experiment involves statistical processes. Even if one keeps the conditions of an experiment constant the repetition of the experiment leads to different results and can vary from the predictions of the model. The finite size of the measured data sample and the inaccuracy of the measurement can explain the distributions of the outcome. In particle physics an additional uncertainty arises from the nature of quantum mechanics. Every process happens with a certain probability which makes the outcome of single events unpredictable. Only the initial states, the final states and the corresponding transition probabilities can be described by a theoretical model. Because physics wise the most interesting processes often occur with small probabilities one needs large data sets of measured events. The specific analysis chooses then a part of the data sample but in the end one will need a large number of measured values which are used to test the underlying theory. In the statistics of the data sample the specific value can vary on event-by-event basis and might be far away from the true value of the theory in single events, so one tries to find an estimator based on the whole data set and the knowledge about the

physical process. In this thesis a statistical tool - the kinematic likelihood fitter (KLFitter) - is presented which makes use of the maximum likelihood method and the energy-momentum conservation of the detected objects in order to find good estimators and to reconstruct complex physical processes. An introduction to kinematic fitting together with its specific realization in the KLFitter package is given in chapter 4.
The kinematic likelihood fitter is applied to one of the decay channels of the top pair decay, the electron + jets channel. The decay process and the ATLAS detector response are simulated by random sampling methods. The resulting Monte Carlo data which is used to test the performance of the KLFitter is presented in chapter 5. In this chapter the event selection of the data is described and two methods - truth matching and the extraction of transfer functions - are applied to the data. They are needed for a correct modeling of the input to the KLFitter and for evaluating the performance of the kinematic fit.
The performance of the top pair reconstruction with the KLFitter in the electron + jets channel is demonstrated in the Sections 6.1 to 6.4 of chapter 6. Kinematic limitations within the reconstruction are discussed in Section 6.5. The reconstruction of the top pair decay is expanded in Section 6.6 by considering more jets than only those with the largest transverse momentum in events with higher jet multiplicities. Finally, the KLFitter is applied to the main background process to the top pair decay in Section 6.7. The obtained modifications to the KLFitter from Section 6.6 are also tested on background and are compared to the signal results.
Eventually, in chapter 7 a conclusion and an outlook beyond the performed studies in this thesis are given. Some additional Figures and calculations are attached in the Appendix.

Units For the sake of simplicity units will be given in the Heaviside-Lorentz system in this thesis. In particular, this means

$$c = \hbar = \epsilon_0 = \mu_0 = 1 \ , \tag{1.1}$$

which leads to the consequence that energy, momentum and mass are expressed in the same units. Because the scales of particle physics are small this is chosen to be in electron Volt [eV], which is the acquired energy of an electron after it has been accelerated by an electric potential of 1 Volt:

$$1\text{eV} \approx 1.6 \cdot 10^{-19}\text{J} \tag{1.2}$$

For the same reason cross sections or related properties are given in barn [b] which describes approximately the cross sectional area of a Uranium nucleus:

$$1\text{b} = 10^{-28}\text{m}^2 \tag{1.3}$$

All other quantities which do not refer to the subatomic scale are given in SI units.

2. The Top Quark in the Standard Model

The Standard Model (SM) of particle physics [1] is one of the most successful theories in science. It has been tested with very high precision in a variety of experiments. In the SM the interactions of the fundamental particles are described by relativistic quantum field theories combining the three fundamental forces, the electromagnetic, the weak and the strong force, into a consistent structure based on gauge groups. Although all massive particles interact gravitationally, a quantum gravity could not yet be included in the SM. In Table 2.1 the relative strength and the range of all four fundamental forces are listed together with the describing theory, the mediating particles and their masses. The relative strength can give a good overview of the importance of the force in a considered scenario. Gravitation is almost 30 orders of magnitude smaller than the three forces which can be described in the SM. In the energy regime of collider experiments, gravitation can be neglected and does not impact the predictions of the SM.

Table 2.1.: To each of the four fundamental forces belongs a physical theory and mediating particles. There is no quantum theory of gravity and no graviton has been found yet. The relative strength and the range depend on the framework and are only given for illustration [1].

Force	Rel. Strength	Range	Theory	Mediator	Mass
Strong	10	10^{-15}	Chromodynamics	Gluon	0 GeV
Electromagnetic	10^{-2}	∞	Electrodynamics	Photon	0 GeV
Weak	10^{-13}	10^{-18}	Flavourdynamics	W and Z	80.4/91.2 GeV
Gravitational	10^{-42}	∞	General Relativity	Graviton	-

The fundamental forces of the SM and the known elementary particles are introduced in the following with an emphasis placed on top quark physics. Apart from this an outlook is given to physics beyond the SM.

2.1. Elemantary Particles and Fundamental Forces

In the SM all known matter consists of half integer spin particles (fermions) grouped into leptons and quarks, while all interactions are mediated by gauge bosons with integer spin one.

2.1.1. Quarks and Leptons

Both, the quarks and the leptons, are divided into three generations, ordered by their masses. In each generation a neutral and an integer charged lepton and two non-integer charged quarks are formed in pairs together into a lepton and a quark doublet. These doublets can be interpreted as the *weak isospin* doublets of left-handed particles, which means fermions with negative chirality. The weak isospin I_3 is the characteristic quantum number of the weak interaction. The first particle in the doublet has a weak isospin of $+\frac{1}{2}$ and the second of $-\frac{1}{2}$. Fermions with positive chirality, so called right-handed particles, have an isospin of 0 and thus form singlets, which do

not interact weakly (see Sec. 2.1.2).
The quark doublets consist of up/down (u/d), charm/strange (c/s) and top/bottom (t/b) quarks. The three up-type quarks with isospin $+\frac{1}{2}$ have $+\frac{2}{3}$ e charge while the down-type quarks with isospin $-\frac{1}{2}$ carry the charge $-\frac{1}{3}$ e. They carry an additional colour charge of either red, green or blue. Each of the three electrically charged leptons (l), namely electron (e), muon (μ) and tau (τ), carry a charge of one elementary charge and, together with their corresponding zero charged neutrino (ν_l), form the other weak isospin doublet.

$$\begin{array}{lccc} \text{Generation :} & \text{I} & \text{II} & \text{III} \\ \text{Quarks :} & \begin{pmatrix} u \\ d \end{pmatrix} & \begin{pmatrix} c \\ s \end{pmatrix} & \begin{pmatrix} t \\ b \end{pmatrix} \\ \text{Leptons :} & \begin{pmatrix} \nu_e \\ e \end{pmatrix} & \begin{pmatrix} \nu_\mu \\ \mu \end{pmatrix} & \begin{pmatrix} \nu_\tau \\ \tau \end{pmatrix} \end{array}$$

Each fermion comes along with an associated antiparticle with opposite electric charge, weak isospin and colour charge, but with the same mass (if CPT symmetry[1] is conserved). Left-handed antiparticles are then weak isospin singlets, while the right-handed antiparticles form doublets. Because in the quantum field theory describing the SM no quantum states with non-integer charges are allowed, quarks form hadrons. Quarks and anti-quarks combine only in pairs to mesons ($q\bar{q}$) or in triplets to baryons (qqq or $\bar{q}\bar{q}\bar{q}$). The Pauli exclusion principle demands that three quarks forming a baryon differ in at least one quantum number. This is always fulfilled because only red, green and blue quarks (or anti-quarks with corresponding anti-colour) can be combined to an (anti-)baryon. Similarly, only quark and anti-quark with corresponding colour and anti-colour combine to mesons, which makes all composed hadrons colourless.
All fermions in the SM are observed to have mass although no absolute values for the vanishing neutrino masses could yet be measured. Mass differences of neutrinos with different flavours were observed in neutrino oscillation experiments (see Sec. 2.1.2) and upper and lower limits can be given on the neutrino masses [2, 3, 4]. The masses of all known quarks and leptons [4] are listed in Table 2.2.

Table 2.2.: The measured mass values for all quarks and leptons are shown. In case of the electron and muon masses, the errors are negligible for the given accuracy.

Quarks		Leptons	
Flavour	Mass [MeV]	Flavour	Mass [MeV]
up	1.5 to 3.3	ν_e	$< 225 \cdot 10^{-6}$ (95 % CL)
down	3.5 to 6.0	e	0.511
charm	$1270\ ^{+70}_{-110}$	ν_μ	< 0.19 (90 % CL)
strange	$105\ ^{+25}_{-35}$	μ	105.658
top	$(171.3 \pm 1.63) \cdot 10^3$	ν_τ	< 18.2 (95 % CL)
bottom	$\left(4.20\ ^{+0.17}_{-0.07}\right) \cdot 10^3$	τ	1776.84 ± 0.17

[1] CPT symmetry refers to the invariance of a physical system under simultaneous inversion of charge, parity and time.

The masses of the neutrinos cannot be added to the SM in a straight forward manner, because so far only left-handed neutrinos have been observed and the Higgs coupling (see Sec. 2.1.2) involves both chiralities and manifests on a total different mass scale. The simplest satisfying solution is to assume that neutrinos are Majorana fermions, meaning that they are their own antiparticles, and then add right-handed neutrinos with large Majorana masses via the *seesaw mechanism* [5, 6, 7, 8]. If neutrinos are Majorana particles, neutrinoless double-beta decay is allowed which has not yet been observed.

2.1.2. Interactions

In the SM the electromagnetic, weak and strong interactions are described. Each of the force is obtained by the same mechanism from the underlying physical theories: Quantum Electrodynamics (QED), Quantum Flavourdynamics (QFD) and Quantum Chromodynamics (QCD).

Local Gauge Theory

The SM is mathematically described by chiral gauge theories of Lie-groups [9], to be more precise by gauge theories of the unitary group of degree one, the U(1), and of the special unitary groups[2] of degree two and three, the SU(2) and SU(3). The dimension of arbitrary unitary groups U(n) is n^2, while the dimension of special unitary groups SU(n) is reduced by one to $n^2 - 1$. The corresponding groups to the QED, QFD, and QCD are the Abelian group U(1) and the non-Abelian groups SU(2) and SU(3), respectively. The representing matrix of the symmetry group U(1) is generated by a scalar phase, while the representing n×n matrices of the symmetry groups SU(n=2) and SU(n=3) can be generated by the Pauli and Gell-Mann matrices, respectively [10]. Following the Lagrange formalism the field equations[3] and thus the interacting forces can be obtained by calculating the derivatives of the Euler-Lagrange equations. In order to do so one needs the Lagrangian density that describes the system. In the quantum field theories of the SM the Lagrangian densities are obtained from the free fields of the considered particles demanding that the Lagrangian is invariant under local gauge transformations of the specific symmetry. This introduces gauge terms of new (vector) fields of the dimension of the symmetry, which couple to the considered particles and, in addition, require their own free Lagrangian. These gauge fields can be identified with gauge bosons of spin one which mediate the particular force. The number of the mediating bosons is thus equal to the dimension of the symmetry group. The gauge bosons couple then to the quantum number of the underlying theories, the electric charge, the colour charge and the weak isospin. The local gauge invariance can only be obtained as described above if the gauge bosons are massless.

Quantum Electrodynamics and Chromodynamics

In QED the force mediating particle is the massless and electrically neutral photon. In QCD the eight vector fields correspond to massless gluons in eight different colour/anti-colour charge combinations of red, green and blue. All electrically charged particles interact electromagnetically, whereas only quarks carry colour charge and hence participate in the the strong interaction. In contrast to the Abelian QED, the matrices of the non-Abelian symmetry group of the QCD do not commute, which results in self-interactions terms for gluons and leads to a special characteristic of the strong force.

[2] The groups are called special because the representing matrices have a determinant of one.
[3] The classical analogy are the equations of motion.

It is known from the electromagnetic force that the closer interacting test charges are, the larger is the measured charge or in other words the coupling of the force (*running coupling constants*) [11]. In quantum field theory this can be visualized with charge screening by a polarized vacuum. Because gluons carry a colour charge themselves and can thus couple to themselves, for instance by splitting into pairs of gluons, the strong force behaves differently: at small distances, or high energies, the interaction weakens and particles become essentially free, which is referred to as *asymptotic freedom*. This has also the consequence that at lower energies the quarks are confined, so no free quark can be observed, which is also known as quark *confinement*.

The Weak Interaction and the Higgs Mechanism

However, it is observed that the three weak gauge bosons, the neutral Z and the charged $W^{\pm}$, are massive particles with masses of 91.1876 ± 0.0021 GeV and 80.398 ± 0.025 GeV [4], respectively. In this case, the local gauge invariance can only be maintained by introducing the Higgs mechanism [12, 13, 14], which breaks the symmetry spontaneously. This is acquired by a scalar Higgs field with non-zero vacuum expectation value. The resulting massive and self-interacting Higgs boson has not yet been discovered but would introduce particle masses to the SM. It has no spin, is CP-even and its coupling is expected to be proportional to the fermion masses and mass squared in case of W and Z bosons. Therefore the Higgs mass is connected to the W boson and top mass which is summarized with experimental and theoretical exclusions in Figure 2.1 [15].
At high energies (> 100 GeV) the electromagnetic and the weak force unify according to the Glashow, Weinberg and Salam (GWS) model to the electroweak force ($SU(2)_L \otimes U(1)_Y$) with the new quantum number $Y = 2(Q - I_3)$, the weak hypercharge. The index L indicates that only left-handed states have weak isospin and are thus involved in the weak interaction, while both chiralities carry hypercharge, the generator of U(1) [5]. The two neutral states of the resulting four gauge fields produce then one massless and one massive linear combination, which correspond to the photon and the Z boson, respectively. In other words the electroweak states are mixed via the *weak mixing angle*. The coupling constants of the electromagnetic and the weak force are thus not independent. The two W bosons carry not only an electric charge of ± 1, but also weak isospin. Subsequently, they can couple to themselves, but also to the neutral Z boson and the photon.
Since all left-handed particles carry weak isospin, they interact via the electroweak force, although the photon does not couple to the neutrinos. However, the weak eigenstates q' of the quarks are not the same as the mass eigenstates q of the physical quark, but linear combinations of each other, represented by the 3×3 Cabbibo-Kobayashi-Maskawa (CKM) matrix:

$$\begin{pmatrix} d' \\ s' \\ b' \end{pmatrix} = \begin{pmatrix} V_{ud} & V_{us} & V_{ub} \\ V_{cd} & V_{cs} & V_{cb} \\ V_{td} & V_{ts} & V_{tb} \end{pmatrix} \begin{pmatrix} d \\ s \\ b \end{pmatrix} \tag{2.1}$$

The single elements $V_{q_u q_d}$ of the matrix represent the coupling between the considered up-type and down-type quark. Experiments show, that this matrix differs slightly from the unit matrix which allows for transitions between the three quark generations due to charged weak interaction [4]. As indicated by the mentioned neutrino oscillations (see Sec. 2.1.1) not only quarks can change their flavour and generations described by the CKM matrix but also leptons can mix similarly between generations expressed in the Pontecorco-Maki-Nakagawa-Sakata (PMNS) matrix. But while the CKM matrix is almost diagonal, the leptonic mixing angles can be large.

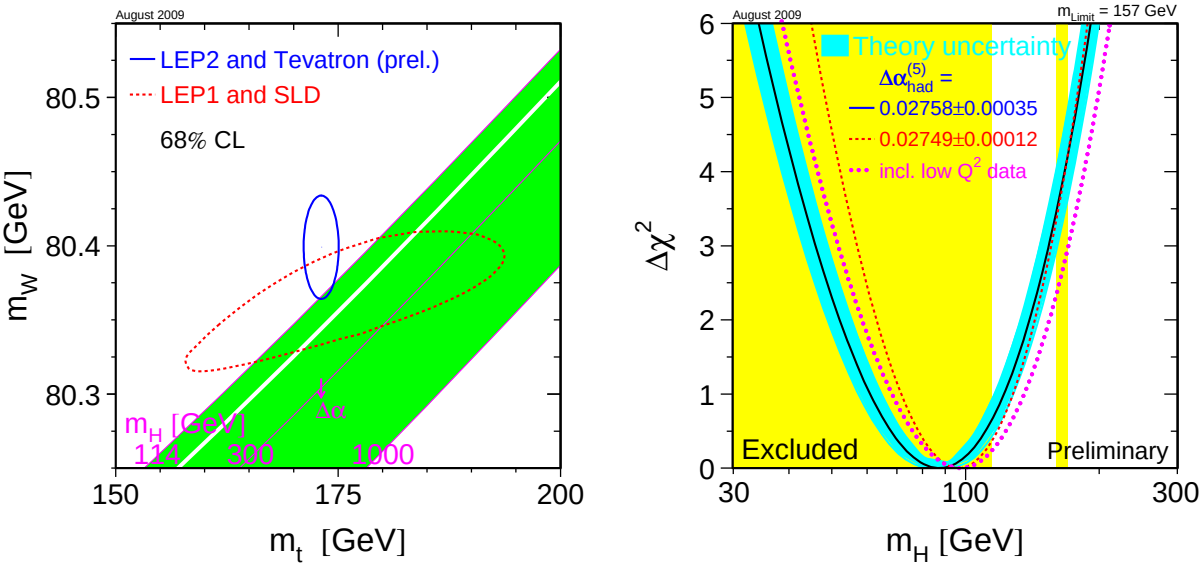

(a) In the electroweak fit of the loop corrections for the SM, favoured Higgs masses of 114 GeV $< m_H <$ 1000 GeV are shown as a function of the top quark and W boson masses (green shaded). The white region is excluded by direct searches. With 68 % ($\hat{=}$ σ) confidence level the experiments CDF, DØ and those at LEP-2 (solid contour) could constrain the Higgs mass by direct measurements, while the experiments at LEP-1 and SLD (dashed line) could exclude regions of the fit via indirect constraints on m_W and m_t. The arrow ($\Delta\alpha$) indicates the additional uncertainty of the relation if $\alpha(m_Z^2)$ changes by $\pm$ 1σ.

(b) The *blueband* plot shows the χ^2 of the electroweak fit as a function of the Higgs mass with the experimental exclusions (yellow shaded) and the theory uncertainties (blueband). The most probable value of the Higgs mass, where the χ^2 is minimal, is already excluded by the LEP experiments and the range of 160 GeV to 170 GeV is excluded by the Tevatron. The dashed curves show the fit with different assumptions for $\Delta\alpha^{(5)}_{had}(m_Z^2)$, the dotted curve shows a fit including low-Q^2 data.

Figure 2.1.: Constraints on the Higgs mass obtained via electroweak fits and experimental exclusions.

Conservation Laws

According to the Noether theorem a conserved quantity arises from each continuous symmetry of a system. Generally, a physical system is invariant under spatial, rotational and time translation with the following conservation laws of linear and angular momentum and conservation of energy. From the symmetries of the GWS and QCD the corresponding electric charge (hypercharge), weak isospin and colour charge are conserved. In addition, it is observed that the baryon number and the lepton number are always conserved in interactions described by the SM.

2.1.3. Beyond the Standard Model

There are several observations and theoretical calculations in astrophysics and particle physics that give rise to questions which can not be answered within the SM:

- Because particles and antiparticles should have been created in pairs during the Big Bang there should be the same amount of matter and antimatter in our Universe. Most of the entire known Universe consists of matter, so there must be CP violation which can not only be explained by the residual phase factor of the CKM matrix [16].

- There are astronomical observations that the matter described by the SM can explain only about 5 % of the mass and energy of the Universe. So there must be matter that does not radiate, called *Dark Matter* (~ 20 %), building a halo structure around the nuclei of the galaxies and increasing the rotational speed of the stars [17]. Supersymmetry could provide a candidate, the lightest superysmmetric particle (LSP), which is stable and interacts only weakly. Also other hypothetical particles, like the axion which is introduced for explaining the absence of CP violation in QCD, could contribute to Dark Matter.
  All the visible and Dark Matter would slow down the expansion of the Universe. However, it was discovered that the contrary is the case. As a consequence, *Dark Energy* (~ 75 %) was introduced which is conceptually similar to Einstein's Cosmological Constant and accelerates the expansion of our Universe [18].

- The desire to unify the three fundamental forces of the SM is understandable after the success of the electroweak unification. However, the three coupling constants in the SM do not converge at the grand unification (GUT) scale of approximately 10^{16} GeV. Furthermore, gravity is not included but is bound to play a role at very high energies (Planck scale $\approx 10^{19}$ GeV) [19].

- Related to the former point is the hierarchy problem: If the Higgs boson exist, its mass is renormalized by various loop corrections and unless there is no *fine tuning*, the mass can increase up to the Planck mass [20].

In fact there are theories like supersymmetry, extra dimensions or string theories, and also higgsless theories like technicolour, which can solve a few of these questions but yet no evidence for one of these theories has been found.

2.2. Top Quark Physics

The top quark is the most recently discovered quark and plays a special role in the SM because of its large mass of $173.1 \pm 0.6(\text{stat.}) \pm 1.1(\text{syst.})$ GeV [21]. Long before its discovery in 1995 [22, 23] at the DØ and CDF experiments at the Tevatron, the existence of the top quarks was predicted. In 1973 Kobayashi and Maskawa postulated a third generation of quarks to explain CP violations in kaon decays [24], which was confirmed after the top quarks isospin partner, the bottom quark, had been found in 1977 [25]. Due to its large mass, which results in a short lifetime of only $4.2 \cdot 10^{-25}$ s, the top quark decays before it hadronizes in the time scale of strong interactions of 10^{-23} s. Consequently, not only one had to reach very high centre-of-mass energies in colliders to produce the top quark, but also no bound states of the top quark exist and it can be only indirectly measured by its decay products. On the other hand this allows for the unique opportunity to observe a bare quark.
Although the top mass is known with high precision, the charge and the spin of the top quark predicted by the SM are not confirmed by measurements. However, the hypothesis of an exotic top quark with charge of $-\frac{4}{3}e$ could be excluded with 95 % confidence level [26, 27, 28]. Due to the short lifetime of the top quark, the spin correlations in the top quark pair production (Sec. 2.2.1) is directly propagated to the decay products, but could not be determined with

sufficient confidence yet [29, 30]. Because of the (V-A) structure of the weak interaction, the W boson in the top quark decay is expected to be only left-handed (30 %) or longitudinally polarized (70 %) [31]. Studying the W-helicity is thus also of particular interest.
Besides studying its properties, understanding top quark physics also opens the gate to new physics. As mentioned in Section 2.1.2, the large top quark mass leads to a strong coupling to the Higgs field, of which one can take advantage in electroweak fits. In order to predict or constrain the Higgs mass one needs a precise measurement of the top quark mass [15]. Because the complex decay signature is similar to that of many supersymmetric events, the top pair decay is a background process for searches for physics beyond the SM. Moreover, the top quark decay can be used for calibrating the detectors due to its well known topology. This is of particular importance in the beginning of new experiments.

2.2.1. Top Quark Production

Top quarks can be produced in pairs via the strong interaction or as single particles via the weak interaction. Although the cross section for both productions is at the LHC of the same order of magnitude, the strong production is of special interest, because it can be more easily separated from background.

Top Pair Production

There are four leading order (LO) Feynman diagrams for the strong top production representing two different production processes (Fig. 2.2). At the LHC the top pair production is dominated

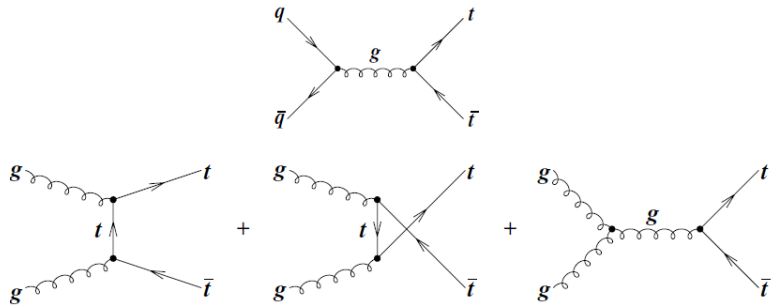

Figure 2.2.: Leading order Feynman diagrams for top quark pair production via the strong interaction

by gluon-gluon fusion (85%) while $q\bar{q}$-annihilation contributes to about 15% at 10 TeV. This can be understood by looking at the parton model of the proton in Figure 2.3.
The proton consists not only of its three valence quarks but also of gluons interacting between the valence and sea quarks. Depending on the energy scale Q, at which the proton is probed, the gluons are observed to split into $q\bar{q}$-pairs which are called sea-quarks. Each gluon or quark carries only a fraction, the so called *Bjorken* x, of the protons' total momentum. The parton density functions (PDFs) $x \cdot f(x, Q^2)$ describe the probability density to find a parton with a certain momentum fraction x at a scale Q^2.
In Figure 2.4 the PDFs for different quarks and for gluons are shown. It can be seen that for small x the contribution from gluons is much larger than from quarks. At the energies of the

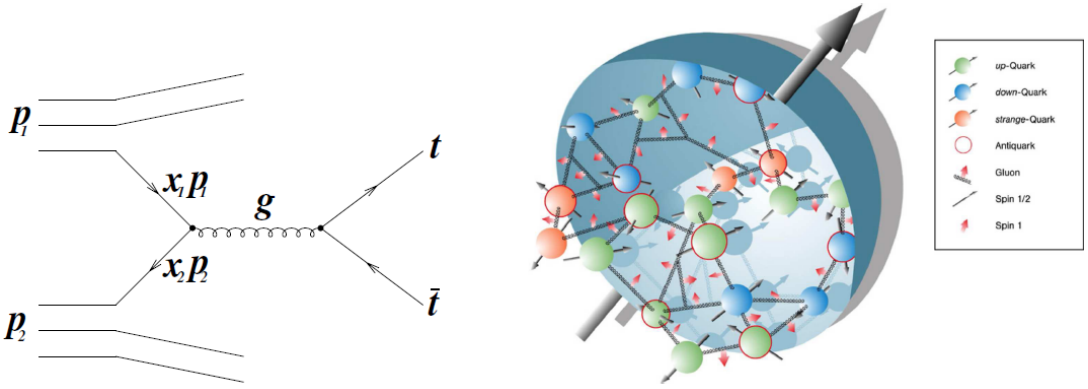

Figure 2.3.: A proton consist not only of the three valence quarks, but also of many quark-antiquark pairs and gluons. Thus the interacting partons carry only a fraction of the total momentum of each colliding proton.

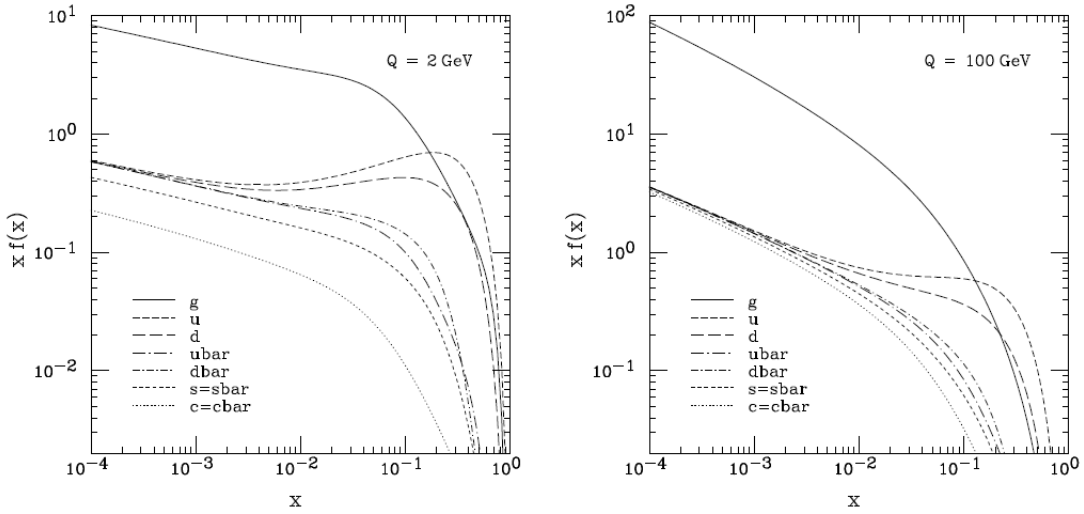

Figure 2.4.: The parton density functions CTEQ6M at the energy regimes of 2 GeV and 100 GeV are shown on a logarithmic scale for different quarks and for gluons [32].

LHC (10 TeV) already a very small fraction $x_i \geq 0.035$ of the two interacting partons is sufficient to produce a top quark pair according to the equation for the effective centre-of-mass energy $\hat{s}$

$$\sqrt{\hat{s}} = \sqrt{x_1 x_2 s} \geq 2m_{top} \quad . \tag{2.2}$$

In order to calculate the total cross section of the $t\bar{t}$ production all different production processes with their cross section $\hat{\sigma}_{i,j}$ convoluted with the PDFs have to be taken into account:

$$\sigma_{tot}(t\bar{t}) = \sum_{i,j} \int dx_i dx_j f_i(x_i, Q^2) f_j(x_j, Q^2) \hat{\sigma}_{i,j}(x_i, x_j) \quad . \tag{2.3}$$

Assuming a top quark mass of 172.5 GeV this leads with near NNLO precision to an expected $t\bar{t}$ cross section at 10 TeV [33] of

$$\sigma_{t\bar{t}}^{\mathrm{NNLO}}(10\ \mathrm{TeV}, 172.5\ \mathrm{GeV}, \mathrm{CTEQ6.6}) = 401.60\ {}^{+3.7\%}_{-4.3\%}(\mathrm{scales})\ {}^{+4.6\%}_{-4.5\%}(\mathrm{PDF})\ \mathrm{pb} \quad . \tag{2.4}$$

For comparison the $t\bar{t}$ production cross sections measured by the CDF and DØ experiments at the Tevatron during the two run phases and the corresponding relative contribution by gluon fusion or quark-antiquark annihilation are listed together with predicted values for possible centre-of-mass energies at the LHC in Table 2.3. As discussed, these values depend on the different centre-of-mass energies and on the assumed top quark mass.

Table 2.3.: The cross sections for $t\bar{t}$ production measured by the CDF and DØ experiments are compared to the expected cross section for the LHC at a centre-of-mass energy of 10 TeV and 14 TeV. The contributions from the different production mechanisms depend on the centre-of-mass energies.

Process	Tevatron (Run I) $\sqrt{s}$ =1.8 TeV	Tevatron (Run II) $\sqrt{s}$ =1.8 TeV	LHC at $\sqrt{s}$ =10 TeV	LHC at $\sqrt{s}$ =14 TeV
$\sigma_{t\bar{t}}$(CDF)	6.5 $^{+1.7}_{-1.4}$ pb [34]	7.5 $^{+0.48}_{-0.48}$ pb [35]	-	-
$\sigma_{t\bar{t}}$(DØ)	5.69 $^{+1.60}_{-1.60}$ pb [36]	8.18 $^{+0.98}_{-0.87}$ pb [37]	-	-
$\sigma_{t\bar{t}}$(Theory)	5.2 $^{+0.5}_{-0.7}$ pb [38]	6.7 $^{+0.7}_{-0.9}$ pb [38]	401.60 $^{+5.9\%}_{-6.2\%}$ pb [33]	833 $^{+52}_{-39}$ pb [39]
$q\bar{q}$-contrib.	90 %	85 %	15 %	10 %
gg-contrib.	10 %	15 %	85 %	90 %

Single Top Production

Just recently the single top production via weak interaction was discovered at the Tevatron by the DØ and CDF experiments [40, 41, 42]. In leading order a t-channel, s-channel and associated Wt production process contribute to the total cross section (Fig. 2.5).

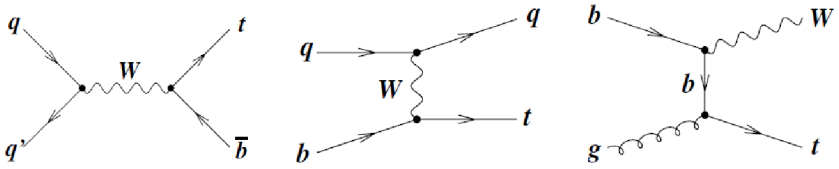

Figure 2.5.: Leading order Feynman diagram of single top quark production via the weak interaction

Before the observation of the single top quark production only an indirect measurement of the CKM matrix element V_{tb} assuming unitarity of the CKM matrix and using the V_{ts} and V_{td} elements was possible. The latest single top cross section measurement enables a direct estimation of $|V_{tb}| = 0.91\ ^{+0.11}_{-0.11}(\text{stat} + \text{sys}) \pm 0.07(\text{theory})$ [43]. A significant deviation of V_{tb} from 1 would indicate the existence of a fourth quark family.
The cross section of the different channels for single top production at the LHC are expected to be [44]

$$\sigma^{\text{NLO}}_{t\bar{t}}(\text{t} - \text{channel}) \approx 124.5 \text{ pb} \ , \tag{2.5}$$

$$\sigma^{\text{NLO}}_{t\bar{t}}(\text{s} - \text{channel}) \approx 6.6 \text{ pb} \ , \tag{2.6}$$

$$\sigma^{\text{NLO}}_{t\bar{t}}(\text{Wt} - \text{associated}) \approx 32.7 \text{ pb} \ , \tag{2.7}$$

at the LHC running with an energy of 10 TeV. But as already mentioned the signal over background ratio for single top production is much worse than for $t\bar{t}$ production.

2.2.2. Top Pair Decay Channels

Since the absolute value of the CKM matrix element $|V_{tb}|$ is approximately 1, the top quark decays almost exclusively (99.8 %) into a W boson and a b-quark. The decay channels of the top pair production are therefore classified according to the final states of the two W boson decays. The W boson can decay into a charged lepton and its corresponding neutrino or into a pair of light quarks ($u\bar{d}$ or $c\bar{s}$).
This leads to three possible decay signatures of the $t\bar{t}$ event:

- the *di-leptonic* channel ($W^+W^- \to l^+\nu_l l^-\bar{\nu}_l$), in which both W bosons decay into leptons,
- the *lepton + jets* channel ($WW \to l\nu_l q\bar{q}$), in which one W boson decays into a quark pair and one into a lepton pair and
- the *full-hadronic* channel ($WW \to q\bar{q}q\bar{q}$), in which both W bosons decay into quark pairs.

As an example the top pair decay into the lepton + jets channel is sketched in Figure 2.6. Because lepton universality approximately holds, the branching ratios (BR) for the W bo-

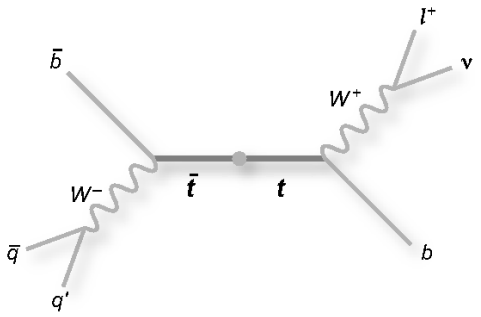

Figure 2.6.: Schematic of the top pair decay into the lepton + jets channel

son decaying into an electron (10.75 ± 0.13 %), a muon (10.57 ± 0.15 %) and a tau lepton (11.25 ± 0.20 %) are almost equal. The hadronic decay into $q\bar{q}$-pairs has a BR of 67.60 ± 0.27 % [4]. Similar numbers can be estimated from pure combinatorics by counting the possible final states taking into account the colour charges of the quarks. The resulting BRs of the $t\bar{t}$ decay in LO are shown in a pie chart in Figure 2.7.

2.2.3. Experimental Aspects

Signature

In an experiment the three different decay channels leave signatures in the detector which have special characteristics and can be used to identify the production of $t\bar{t}$-pairs. The charged leptons can be directly measured by their momentum and deposited energy in the detector. The quarks form bundles, which can be seen as so called *jets* in the calorimeter. Neutrinos are not detectable,

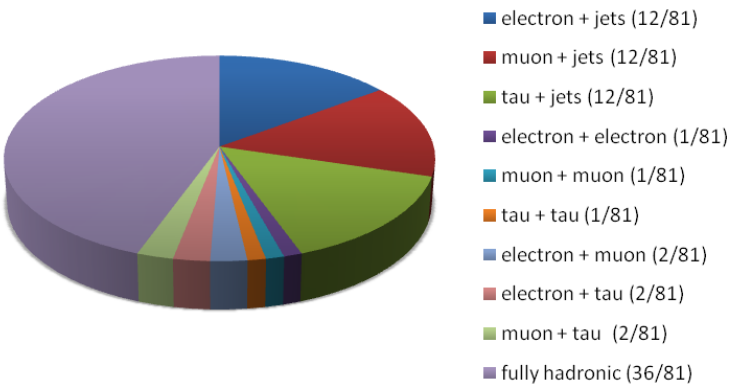

Figure 2.7.: Pie chart of the different final states in the top pair decay

though one can reconstruct their transverse momentum: because of momentum conservation, the negative sum of the momentum components of all measured objects, the missing transverse energy $\not{E}_T$, is approximately the momentum of the neutrinos (see Sec. 3.2.1).
The signatures of the decay channels are as follows:

- The dileptonic channel has a very clear signature with two leptons with opposite charge and two b-jets which might be identified with b-tagging techniques. Since only the sum of the $\not{E}_T$ caused by the two neutrinos can be measured, no four-momentum vector of the single neutrinos can be reconstructed. The BR of this channel is only about $\frac{4}{81}$. QCD background (see below) contributes only marginally and also other background processes can be easily separated.

- The lepton + jets channel is often called *golden channel* because of its relatively large branching ratio of 15 % for each lepton type (in total $\frac{24}{81}$) and because the complex signature is relatively easy to identify. The signature comprises four jets, two of them b-jets, one charged lepton and $\not{E}_T$ due to one neutrino. Background processes to this channel are discussed in more detail in Section 2.2.3.

- In the full-hadronic channel six jets need to be measured. There is no $\not{E}_T$ in this channel and the BR is with $\frac{36}{81}$ quite large. The signature can be easily imitated by QCD background processes.

Because the tau lepton can decay hadronically and is difficult to identify, it is usually treated separately and is here not included in the specific channels or in the given branching ratios.

Background Processes for the lepton + jets Channel

In every higher order calculation it is possible that the initial state or the final state particles radiate a gluon or a photon depending on their couplings. Since radiated gluons with high energy can imitate jets from the hard-scattering process and have an impact on the kinematics of the radiating particles the *initial or final state radiation* (ISR/FSR) changes the overall topology of the events.
For the lepton + jets channel there are two main background sources. If a single leptonically

decaying W boson is produced by the proton-proton interaction and additionally at least four jets are detected, coming for instance from gluon radiation, the physical signature is very similar to the one of the lepton + jets channel. This physical background, called *W + jets*, is difficult to handle because the final state particles are the same and one has to find good discriminating variables to distinguish W + jets from $t\bar{t}$ events. Examples for leading order Feynman diagrams (W + 2 jets) are shown in Figure 2.8.

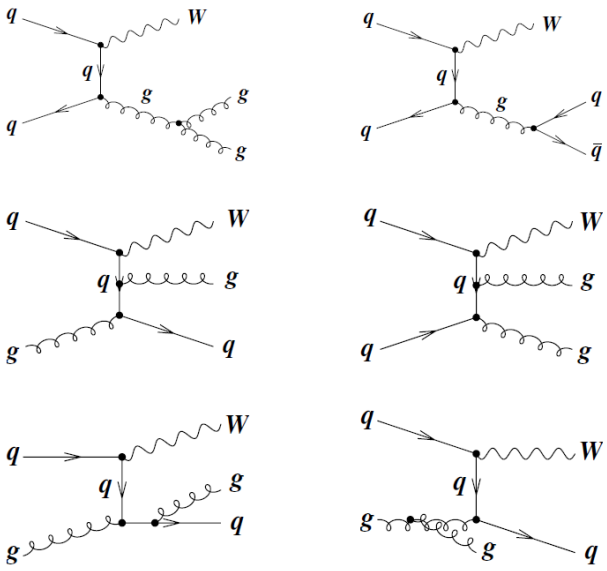

Figure 2.8.: Feynman diagram in leading order for the W + 2 jets background process.

The second background source is of *instrumental* nature which means that either due to limitations of the detector information is lost or the interpretation of the detector response is incorrect. In multijet QCD processes a jet might be misidentified as an electron or a muon coming from a jet might be falsely called isolated. In addition, inefficient measurements of the jet energies, fluctuations in the jet response, lost jets in the detector or miscalibration of the calorimeters may lead to a significant $\not\!\!E_T$.

Combinatorial Assignment of the jets in the lepton + jets Channel

Jets are in general flavour and charge blind which means that by only measuring the jet properties one can not say which parton originally formed that jet. The only exception are b-jets, where secondary vertices can be separated from the primary interaction point because of the long life time of b-mesons. Neglecting this b-tagging techniques, the four jets of the lepton + jets channel result in 24 possible combinations to assign the jets to the partons[4]. The two light quarks coming from the W boson are indistinguishable in their detector response and in their kinematic properties. Hence, for the reconstruction of the $t\bar{t}$ event there are only 12 combinations left to consider. All combinations of the jet-parton assignment which are not the correct ones are referred to as *combinatorial background*. This includes combinations in which the selected jets do not stem from the final state quarks of the $t\bar{t}$ decay but from ISR or FSR. This is especially the case if jets coming from the $t\bar{t}$ event are not detected due to inefficiencies or the acceptance of the detector.

[4]here: partons ≡ final state particles

3. The ATLAS Experiment at the Large Hadron Collider

As it was pointed out in the last chapter, the existing Standard Model cannot be the final theory for describing fundamental interactions between elementary particles. There are various theoretical speculations how to extend or go beyond the Standard Model in order to solve most of its issues. In the end, only an experiment can provide evidence. At the moment the Large Hadron Collider (LHC) at CERN in Geneva is the best candidate to further explore the Standard Model. It was designed over decades by a huge world wide collaboration of scientists and engineers to push the energy barrier of colliders to a new limit. This chapter shortly describes the LHC and introduces the ATLAS experiment - one of the multi-purpose detectors at the LHC.

3.1. The Large Hadron Collider

The LHC is a two-ring superconducting-hadron collider with a design centre-of-mass energy of $\sqrt{s} = 14$ TeV [45]. The tunnel, which was originally constructed for the former Large Electron-Positron Collider (LEP), has a circumference of approximately 27 km, a diameter of 3.8 m and lies roughly 100 m underground at the CERN Laboratory (Conseil Européen pour la Recherche Nucléarie) near Geneva in Switzerland.

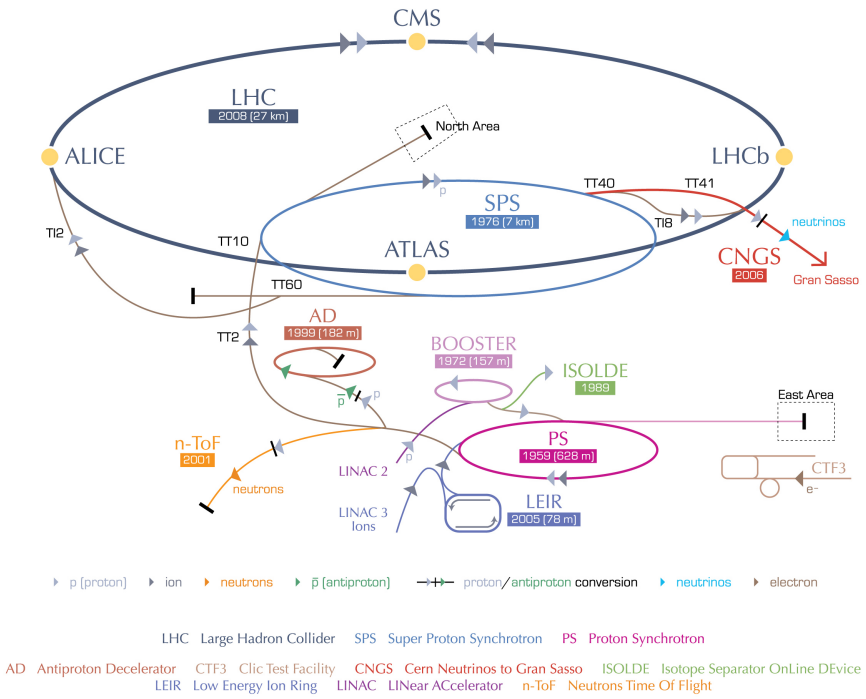

Figure 3.1.: The injector chain and the experiments of the LHC within CERN's accelerator complex.

In its main operation mode (see Fig. 3.1) protons are first pre-accelerated in the Linear Particle Accelerator (LINAC) to the energy of 50 MeV, next in the Proton Synchrotron Booster (PSB) to 1.4 GeV and further in the Proton Synchrotron (PS) to 26 GeV. Finally, the protons gain their nominal LHC injection energy of 450 GeV in the Super Proton Synchrotron (SPS). Two beams of protons in opposite directions are then injected to the ultrahigh vacuum of 10^{-10} mbar inside the beam pipes. Furthermore, lead ions can be accelerated by the LHC. 1 232 dipole electromagnets with a maximum magnetic field of 8.4 T bend the beams on a circular trajectory. In addition, 392 focusing quadrupole magnets avoid that the beams diverge. In order to handle the enormous electric currents which are needed to generate such strong magnetic fields, superconducting magnets are used. Therefore the complete machine has to be kept at 1.9 K through super-fluid liquid helium cooling. Since 96 tonnes of helium are needed for this, it is the largest cryogenic system ever built. Radio frequency cavities along the beam pipe ramp the beam energy from 450 GeV up to maximum of 7 TeV per beam.
At the full design luminosity of 10^{34} cm^{-2}s^{-1} there are 2 808 bunches of about 10^{11} protons each, which circulate in the beam pipe with a spacing of 25 ns between them. With an average of 23 interactions per bunch crossing this results in approximately 920 million proton-proton collisions per second in each of the four interaction points where the experiments ATLAS [46] with LHCf [47], CMS [48] with TOTEM [49], ALICE [50] and LHCb [51] have been built. ALICE and LHCb are both special purpose detectors, the former is built for examining the quark-gluon plasma created by lead ion collisions and the latter for studying CP violation in the b-quark sector. The two multi-purpose experiments CMS and ATLAS are typical onionskin detectors designed for exploring all kinds of new physics or extensions to the Standard Model. The ATLAS experiment is described in more detail in the following.

3.2. The ATLAS Detector

A Toroidal LHC Apparatus (ATLAS) is housed in its cavern at point 1 at the LHC. It is designed to identify particles and measure their tracks and energies with very high precision as well as to handle the high interaction rates, radiation doses, particle multiplicities and energies [52]. The structure of ATLAS is almost cylindrical around the interaction point and nominally forward-backward symmetric with a total length of 44 m, a height of 25 m and a weight of approximately 7 000 tonnes. Figure 3.2 shows an overview of the ATLAS detector with its major components, the innermost tracking system, the calorimeter, the muon spectrometer and the magnet system.

The ATLAS Coordinate System

With its origin in the nominal interaction point the right-handed coordinate system of ATLAS is well defined. The x-axis is pointing from the interaction point to the center of the LHC ring, the positive y-axis is defined as pointing upwards while the z-axis is defined by the beam direction such that $\vec{x} \times \vec{y} = \vec{z}$. The transverse momentum is defined as

$$p_T = \sqrt{p_x^2 + p_y^2} \ , \tag{3.1}$$

where p_x and p_y are the momentum components in the x- and y-direction, respectively. In polar coordinates the azimuthal angle ϕ, always given in radians in the range $[-\pi, +\pi]$, lies in the x-y-plane around the beam axis and the polar angle θ in the r-z-plane. Due to the highly

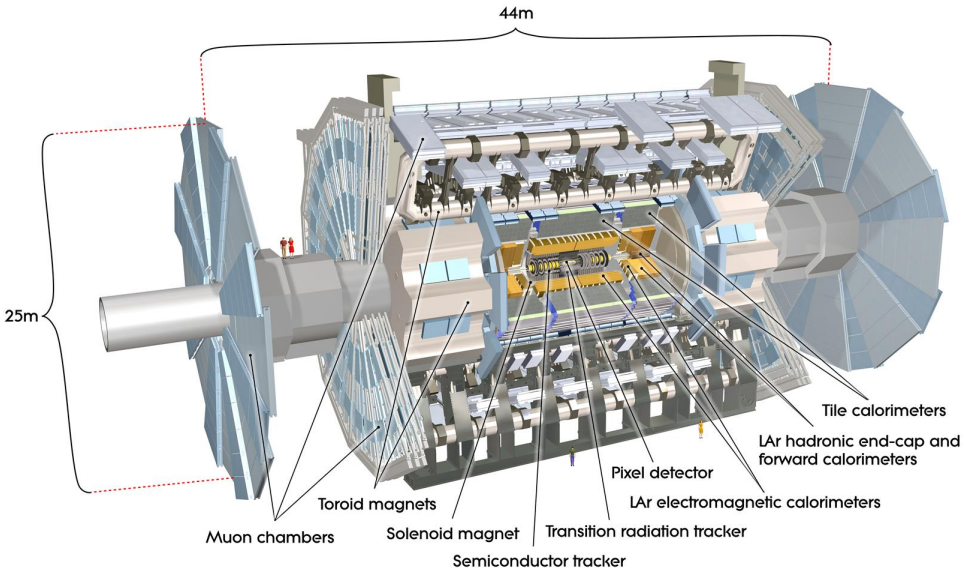

Figure 3.2.: Overview of the ATLAS detector

relativistic nature of the particles, the particle production flux within the detector caused by QCD processes is almost constant with respect to the pseudorapidity

$$\eta = -\ln\left[\tan\left(\frac{\theta}{2}\right)\right] \quad . \tag{3.2}$$

It is assumed that the energy E of the particle is much larger than its mass, so the approximation $E \approx |\vec{p}|$ is valid. Because of its invariance under Lorentz transformations the distance ΔR in η-ϕ space is often used:

$$\Delta R = \sqrt{\Delta\eta^2 + \Delta\phi^2} \quad , \tag{3.3}$$

where $\Delta\eta$ and $\Delta\phi$ are the difference in pseudorapidity and azimuthal angle, respectively.

3.2.1. Interaction of Particles with Matter

The ways in which particles interact with matter is the basis for the design of every particle detector, consequently also for the design of the detector components of the ATLAS experiment. Particles generated in collider experiments can interact with the detector material via various processes and the dominant interaction depends on the energy. The distinction of different types of particles according to their interaction with matter helps to identify the particles and to locate where the energy of the particles is deposited. All charged particles interact electromagnetically and are generally detected by ionization and excitation of bound electrons or γ radiation. Neutral particles need to generate charged particles in interactions before they can be detected. Particles which interact via the strong force can be detected by inelastic scattering mediated by gluons. Particles which interact only weakly, i.e. neutrinos, cannot be directly detected by the ATLAS detector.

Massive Charged Particles

The average energy loss in material of heavy ($m \gg m_e$) charged particles with energies in the range of $0.1 \lesssim \beta\gamma \lesssim 1000$ is given by the Bethe-Bloch formula [53]:

$$-\left\langle \frac{dE}{dx} \right\rangle = 4\pi N_A r_e^2 m_e c^2 z^2 \frac{Z}{A} \frac{1}{\beta^2} \left[\ln\left(\frac{2m_e c^2 \gamma^2 \beta^2}{I} \right) - \beta^2 - \frac{\delta}{2} \right] \quad , \tag{3.4}$$

where z is the charge of the interacting particle, Z and A are the atomic and mass number of the absorber, m_e and r_e are the mass and the classical radius of the electron, N_A is the Avogadro constant, I is the mean excitation potential of the target material and δ parametrizes the *density effect*, which depends on the velocity of the particle. The density effect causes the transverse electric field of relativistic particles to be screened by the charge density of the material, hence the interaction with the material is suppressed. In the energy range of $3.5 \lesssim \beta\gamma \lesssim 1000$ this effect dominates the energy loss with $\delta \propto \ln(\beta\gamma)$, which causes a wide flattish plateau in the logarithmically plotted stopping power (Fig. 3.3). Any particle with energies in this range is called *minimum ionizing particle* (MIP), because the mean energy loss rate is close to the minimum at $\beta\gamma \simeq 3.5$. The range of the plateau is particularly large for muons. Since muons at colliders have typically energies in this range they leave little energy in the detector.

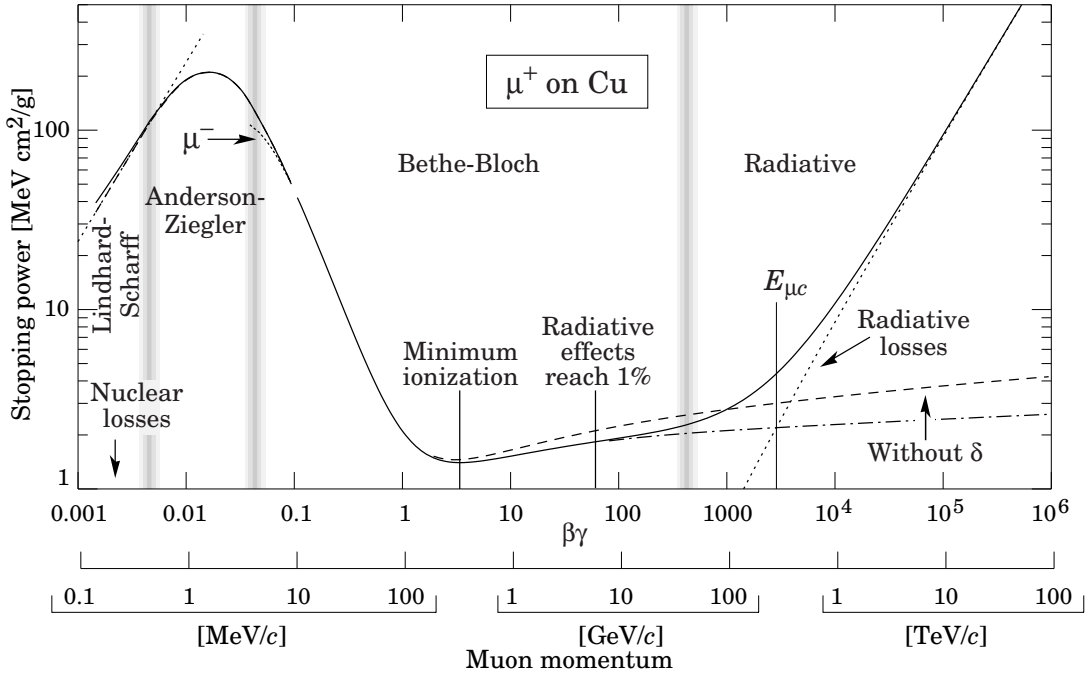

Figure 3.3.: Stopping power for positively charged muons in copper. The plot includes low and high energy regions, where the Bethe-Bloch approximation is invalid [4].

At the lower limit ($\beta\gamma \lesssim 0.1$) of the Bethe-Bloch formula the velocity of the charged particle is comparable to the one of the atomic electrons and thus corrections for atomic effects must be included. At the upper limit ($\beta\gamma \gtrsim 1000$) radiative effects take over. Both limits depend on the atomic number of the material in use.
Additionally, all charged particles radiate if their velocity is larger than the phase velocity of light in a given material, which is referred to as *Cherenkov radiation*. If a relativistic particle crosses the interface of two media of different dielectric constant, *transition radiation* is produced. If

the transferred energy of an incident particle is large enough, secondary *knock-on electrons* can themselves ionize, excite and radiate (δ rays). The contributions to the total energy losses by these effects are generally negligible but the first two processes can be used to track or identify particles [4].

Electrons and Photons

Electrons of low energy loose, like all charged particles, their energy mainly due to ionization and excitations. However, the energy losses of high energy electrons are dominated by bremsstrahlung, because the losses caused by bremsstrahlung are proportional to the particle's energy, but anti-proportional to the square of the particle's mass. Consequently, the average energy loss of electrons cannot be described by the Bethe-Bloch formula. Photons interact electromagnetically via the photoelectric effect, Rayleigh scattering, Compton scattering and pair production of electrons and positrons (see right plot of Fig. 3.4). The latter effect dominates for high energy photons, thus their signature in dense material is similar to the one of high energy electrons. By the interplay of bremsstrahlung and pair production, photons and electrons generate a cascade of 2^n particles resulting in electromagnetic showers. The *radiation length* X_0, in which the electrons' energy is on average decreased to $\frac{1}{e}$ of its initial energy by bremsstrahlung, is thus equal to $\frac{7}{9}$ of the mean free path of high energy photons due to pair production. If the electrons' energy falls below a critical energy E_c, the electrons rather dissipate their energy by ionization and excitation and start to generate less shower particles. At these energies also Møller and Bhabha scattering and positron annihilation contribute marginally, which is sketched in the left plot of Figure 3.4.

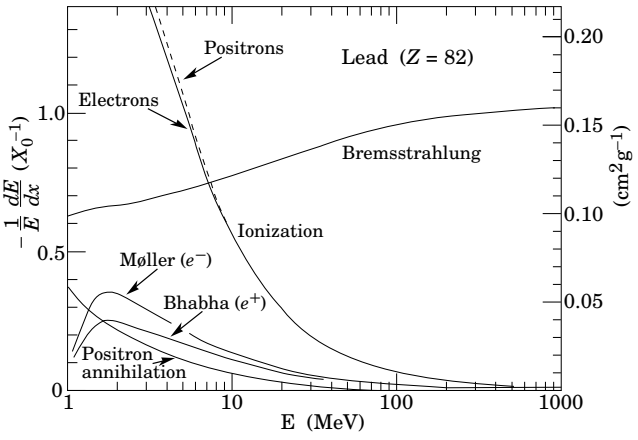

(a) Fractional energy loss per radiation length of electrons in lead due to the various processes as a function of the electron energy. At $E_c \approx 10$ MeV bremsstrahlung and ionization contribute equally to the losses. Møller and Bhabha scattering and positron annihilation are negligible compared to ionization and bremsstrahlung.

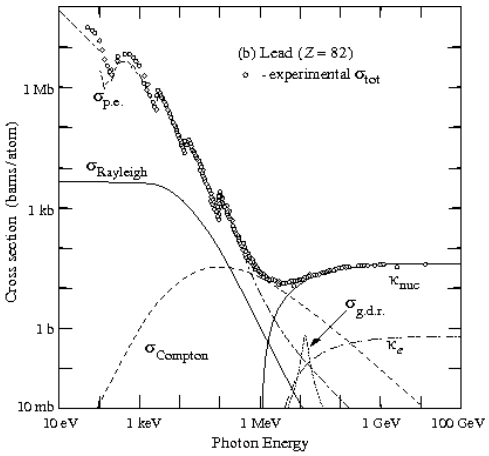

(b) Photon total cross section as a function of its energy in lead. The cross sections of the photoelectric effect $\sigma_{\mathrm{p.e.}}$, Rayleigh scattering $\sigma_{\mathrm{Rayleigh}}$, Compton scattering $\sigma_{\mathrm{Compton}}$, pair production in the nuclear κ_{nuc} and electron κ_{e} field and photo-nuclear interactions $\sigma_{\mathrm{g.d.r}}$ contribute to the total cross section.

Figure 3.4.: The electromagnetic interactions for electrons and photons in lead [4].

Strong Interaction

Although in principle the strong interaction of hadrons with matter is described by QCD, this is not possible in the wide energy ranges of hadron-matter interactions in the detector, because the strong force grows stronger for low energies and can thus not be described by perturbation theory. There are various nuclear effects, for instance spallation and fission, that contribute in cascades to the total energy loss of hadrons. In these processes lighter hadrons like pions, nucleons and kaons are produced by inelastic scattering which results in hadronic showers. The mean free path with respect to inelastic scattering defines the hadronic interaction length λ_a [53]. This quantity has to be considered as an approximation, because various processes can modify the shower length and the measurable energy. The shower length is much larger and its profile is much more inhomogeneous than for electromagnetic showers. For instance, neutral pions, produced in the hadronic shower, decay further into two photons, which leads to electromagnetic sub-showers, that reduce the actual length of the hadronic shower. Moreover, the nuclei of the absorber material can be excited or broken up, which leads to energy losses, of which a large fraction cannot be measured by the calorimeter. The de-excitation of the nuclei may generate, for example, slow neutrons or neutrinos, which are mostly invisible to the calorimeter. Further, pions or kaons can decay into muons and neutrinos, which deposit only little or no energy in the calorimeter, respectively.

Particle Detection with the ATLAS Experiment

As seen in Figure 3.2 the inner detector of ATLAS is included in a strong magnetic field in order to bend the trajectory of charged particles and to allow the measurement of their momentum. The inner detector is surrounded by the electromagnetic and hadronic calorimeters, in which electromagnetically and hadronically interacting particles are absorbed in order to measure their energy. The huge outermost part of the detector, the muon system, is used to detect muons. Figure 3.5 shows a cross-sectional view of the ATLAS detector in order to visualize how the different particles interact with the detector components.
The following signatures are caused by particles traversing the detector:

- Photons are invisible in the tracking system, but deposit their energy in the electromagnetic calorimeter via electromagnetic showers.
- Electrons and positrons leave tracks in the inner detector and are bent by the magnetic field, such that the momentum and the sign of the charge can be measured. The remaining energy is absorbed by the electromagnetic calorimeter via shower formation.
- Neutral hadrons, such as neutrons, are invisible to the inner detector and the electromagnetic calorimeter, but their energy is absorbed by the hadronic calorimeter resulting in hadronic showers, which are called jets.
- Charged hadrons, such as protons, are tracked with the inner detector and electromagnetic calorimeter, which results in a curved trajectory within the magnetic field. They deposit their energy in the hadronic calorimeter via hadronic interactions.
- Muons interact like electrons electromagnetically but due to their much larger mass they shower very rarely and interact seldom in the detector (MIPs). Hence, they are the only particles which can be seen in the outermost detectro component, the muon spectrometer.
- Neutrinos interact only weakly, so they are not directly visible in the detector. The resulting $\not{E}_T$ can be reconstructed depending on the topology of the process under study.

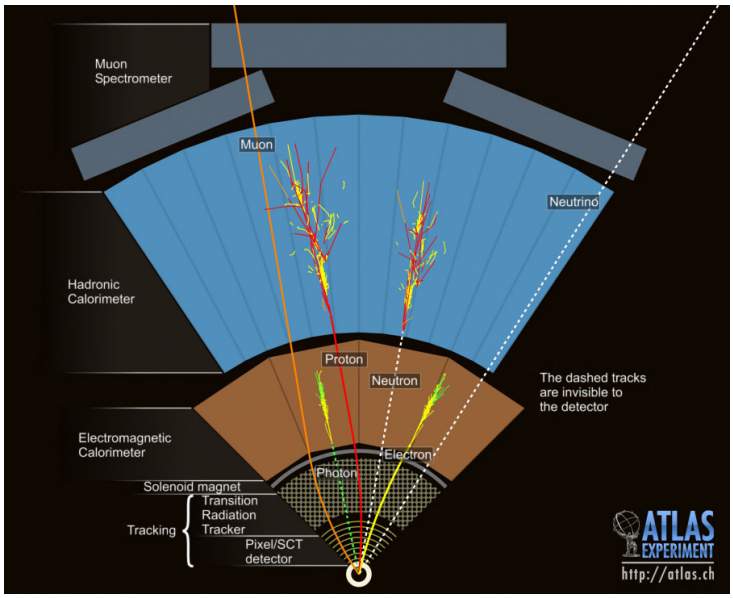

Figure 3.5.: A cross-sectional view of the ATLAS detector. It is sketched how different particles can be detected by the detector components.

Note that the idealized case is described. Hadronically interacting particles can also leave a part of their energy in the electromagnetic calorimeter. Especially neutral pions might decay into two photons and shower electromagnetically.

3.2.2. Inner Detector

Every 25 ns about 1 000 particles will emerge from the interaction point causing a very high track density in the detector. A precise measurement of the momentum, the tracks of the particles and their reconstructed vertices requires a fine granularity of the tracking system. This is achieved by the concentric inner detector (ID) shown in Figure 3.6, which covers the range out to $|\eta| = 2.5$ and consists of three subsystems: the pixel detector, the silicon microstrip tracker (SCT) and the transition radiation tracker (TRT).
A 2 T magnetic field generated by the central solenoid surrounding the ID forces charged particles to move on curved trajectories. The pixel detector and the SCT are based on doped semiconductor sensors in which charged particles leave ionization signals.
The innermost pixel detector consists of three cylindrical barrel layers with two end-caps on each side, each arranged in three disc layers. It has the finest granularity of the ID and is highly segmented in 1 744 sensors with 47 232 pixel each to achieve a good vertex resolution. The identical pixel sensors have a minimum pixel size of $50 \times 400\ \mu\text{m}^2$ which are read out in 80.4 million channels. In order to reduce thermal noise and to realize an intrinsic spatial resolution of about 10 μm in $R - \phi$ and 115 μm in z the pixel system is cooled down to $-10°$ C.
In the SCT each particle traverses four cylindrical double strip layers parallel to the beam axis. Half of the layers in the barrel region have a small stereo angle of 40 mrad with the goal to measure the R- and the ϕ-coordinate. In total 15 912 strip sensors of 6.4 cm length and a pitch of 80 μm are used in the barrel region and on the nine discs at each side in the end-cap region. This leads to 6.3 million readout channels and an intrinsic accuracy of 17 μm in $R - \phi$ and 580 μm in z-direction.

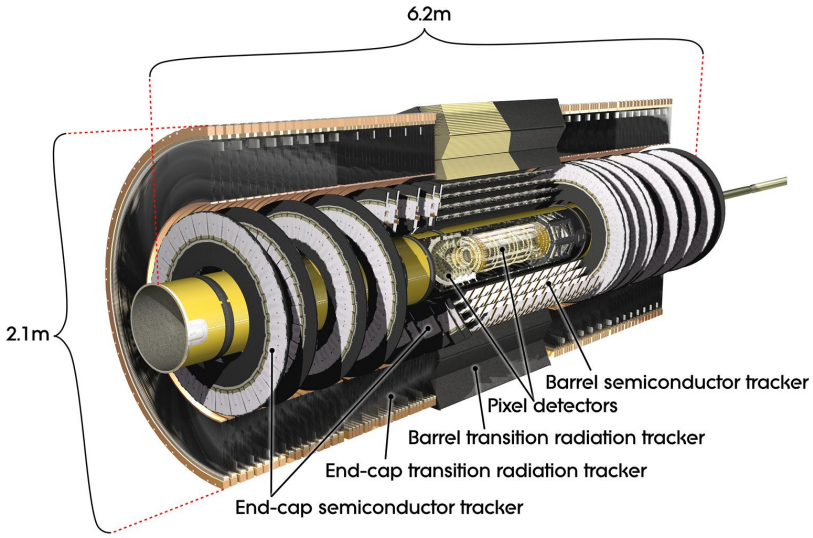

Figure 3.6.: The layout of the inner detector: the innermost pixel, semiconductor and transition radiation tracker in the barrel and the end-cap region.

The largest number of hits, ideally 36 per track, is possible with the 4 mm diameter straw tubes of the TRT. It is parallel to the beam axis and reaches an accuracy of 130 μm in $R-\phi$. The tubes are filled with a $Xe/CO_2/O_2$ gaseous mixture which is ionized by charged particles or photons coming from the transition radiation of the particles. The detection of transition-radiation photons in the Xenon-based gas mixture enables electron and pion identification. The TRT covers a region up to $|\eta| = 2.0$ and has approximately 351 000 readout channels.
The combination of the three different detector systems including the solenoid magnet results in up to 43 hits and thus in a good momentum resolution for the transverse momentum p_T of charged particles. The momentum resolution due to the spatial uncertainty can be obtained via the determination of the sagitta of the curved trajectory and is given by the *Glückstern formula* [54]

$$\frac{\sigma(p_T)}{p_T} = \frac{\sigma(x) \cdot p_T}{0.3 \cdot L^2 \cdot B} \sqrt{\frac{720}{N+4}} \quad , \tag{3.5}$$

where $\sigma(x)$ is the spatial uncertainty, L the length of the track, B the magnetic field of the solenoid and N the number of measured track points. The derivation of Equation 3.5 can be found in the Appendix A.3.

3.2.3. Calorimetry

The calorimeter system is built to measure the energy of electromagnetically and hadronically interacting particles. As already mentioned muons and neutrinos can not be stopped, but electrons, photons and hadrons are absorbed. Both, the electromagnetic (EM) and the hadronic calorimeters in ATLAS, are sampling calorimeters. The principal idea of a sampling calorimeter is to alternate a very dense material which induces particle showers and a highly ionizable material so that the deposited energy can be determined. However, the energy deposited in the dense absorber material cannot be measured. The entire ATLAS calorimeter system is shown in Figure 3.7.

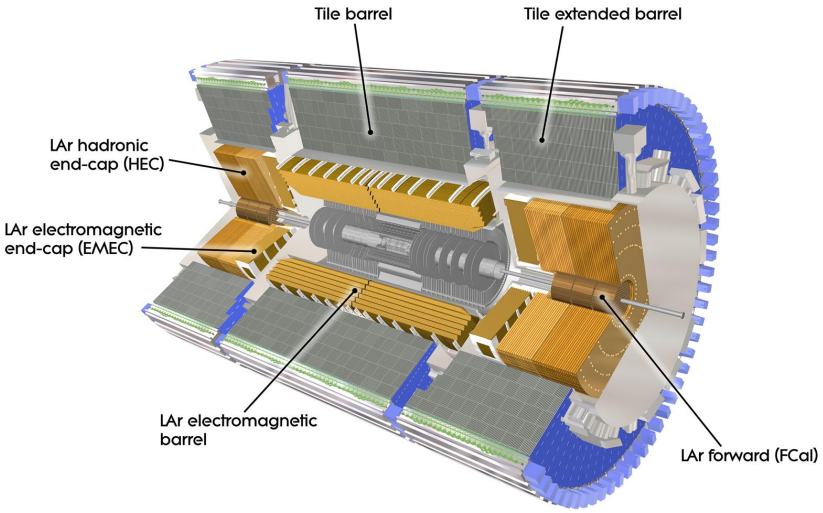

Figure 3.7.: The layout of the LAr calorimeter with the hadronic tile and the hadronic forward calorimeter.

Electromagnetic Calorimeter

The barrel (EMB) and the two end-caps (EMEC) of the electromagnetic calorimeter consist of accordion-shaped lead absorbers with liquid Argon (LAr) in between, ensuring continuity in the azimuth. In gaps between the absorbers kapton electrodes measure the ionization current in the LAr. The active medium Argon was chosen because of its intrinsic linear behaviour, stable response time and radiation hardness [52].
The three layered forward calorimeter (FCAL) close to the beam pipe consists of a copper and Tungsten matrix filled with concentric rods and tubes with LAr in the gaps. Only the first wheel (FCAL1) is an electromagnetic module with copper as the absorber.
The overall weight of 4.5 tonnes and the material budget of the ID lead to the consequence that many electrons, photons and low energy pions already loose a significant part of their energy before reaching the EM calorimeter. Therefore an instrumented Argon layer in the region $0 < |\eta| < 1.8$ complements the electromagnetic calorimeters in order to measure the energy lost in front of the calorimeters (presampler).
The acceptance for the EMB is $|\eta| < 1.475$, the EMEC covers the range $1.375 < |\eta| < 3.2$ while the FCAL is in the very forward region with $3.1 < |\eta| < 4.9$. The total thickness of 22 radiation lengths (X_0) in the EMB and 24 X_0 in the end-caps should avoid punch-throughs of most of the EM showers into the hadronic calorimeter.

Hadronic Calorimeter

The hadronic calorimeter consists of a tile calorimeter in the barrel, a liquid-Argon calorimeter in the hadronic end-cap (HEC) and a liquid-Argon forward calorimeter. In the tile calorimeter steel is used as absorber and scintillator as active medium. It is subdivided into a central and two extended barrels and covers $|\eta| < 1.7$. The light generated in the scintillator is read-out via wavelength shifting fibers. The HEC is a copper LAr sampling calorimeter composed of two cylindrical wheels in the range $1.5 < |\eta| < 3.2$ as illustrated in Figure 3.7. The two hadronic

FCAL modules (FCAL2 and FCAL3) are mainly made of Tungsten serving as the absorber material to minimize the lateral spread of hadronic showers, again with LAr as the sensitive medium in the gaps between the rods and the tubes.

Energy Resolution

Since the number of ionized particles N is proportional to the deposited energy in the calorimeters the energy resolution follows from Poisson statistics

$$\frac{\sigma_N}{N} = \frac{1}{\sqrt{N}} \propto \frac{\sigma_E}{E} = \frac{a}{\sqrt{E}} \ , \tag{3.6}$$

with the Poisson standard deviation $\sigma_N = \sqrt{N}$ and a detector specific proportionality factor a. With this equation one can define a relative energy resolution

$$a = \frac{\sigma_E}{\sqrt{E}} = \frac{\sqrt{\left\langle (E^{\text{true}} - E^{\text{meas}})^2 \right\rangle}}{\sqrt{E^{\text{true}}}} \ . \tag{3.7}$$

where E^{meas} is the measured energy value and E^{true} the true energy known from a test-beam or simulations. The measurement of electrons for the electromagnetic calorimeter and of pions for the hadronic calorimeter has been tested [52] with a resulting relative energy resolution of $a = (10.1 \pm 0.4)\%$ for electrons and $a = (52 \pm 1.0)\%$ for pions. Taking calibration effects with a constant term c and instrumental effects like electronics noise with a proportional term to $\frac{1}{E}$ into account, the overall energy resolution is given by

$$\frac{\sigma_E}{E} = \frac{a}{\sqrt{E}} \oplus \frac{b}{E} \oplus c \ . \tag{3.8}$$

3.2.4. Muon System

The outermost part of the ATLAS detector is formed by the muon spectrometer of which the layout is shown in Figure 3.8. It is designed to detect muons exiting the calorimeter system in the the region $|\eta| < 2.7$ and to measure their momentum precisely. As already mentioned, muons behave like MIPs so only their momentum and not their full energy can be measured. Another important purpose of the muon spectrometer is to provide information to the trigger systems, thus it has to give a very fast response. To fulfill all of these tasks the muon spectrometer is built within a huge 4 T toroidal magnet system and consists of 2 × 2 different detector systems: the precise monitored drift tubes (MDT) and cathode strip chambers (CSC), and the fast resistive plate chambers (RPC) and thin gap chambers (TGC).
The MDT consists of 1 088 chambers with 3-8 layers of proportional counters. The drift tubes are gas-filled (Ar/CO_2) Aluminium cylinders with a Tungsten-Rhenium wire in the center. The drift tubes are monitored by temperature and B-field sensors. With a maximum drift time of 700 ns each of the tubes has a spatial resolution of $60 - 80$ μm with a resulting resolution of about 35 microns per chamber.
Because the MDTs are limited by their counting rate of 150 $\frac{\text{Hz}}{\text{cm}^2}$, they are replaced by 32 multi-wire chambers of the CSC in $|\eta| > 2$, where this rate can be exceeded. The whole CSC system is made out of two discs with 16 chambers each which are also filled with Ar/CO_2 gas. With a sophisticated arrangement of the Tungsten-Rhenium wires, electrons drift less than 40 ns and one can reach a spatial resolution of 60 μm per CSC plane and a counting rate of up to 1000 $\frac{\text{Hz}}{\text{cm}^2}$.

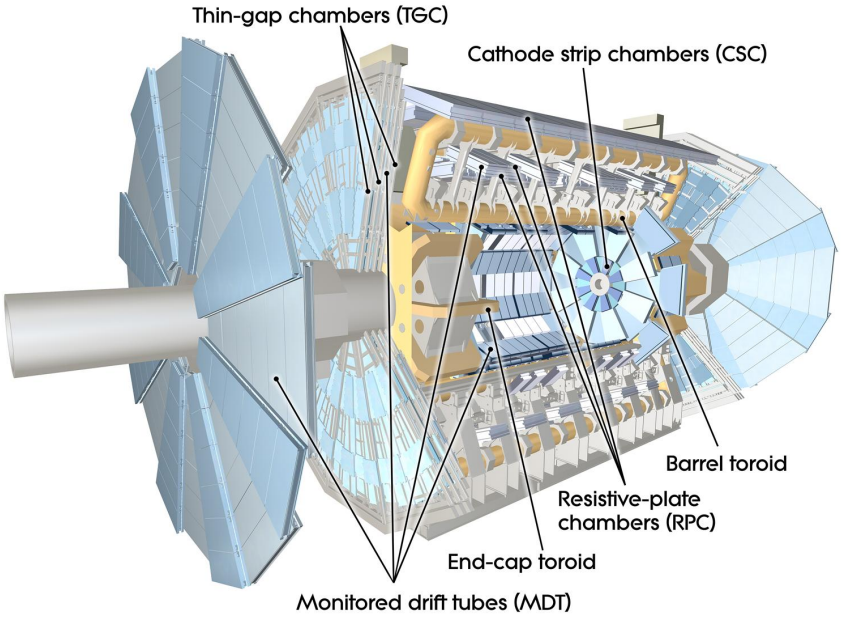

Figure 3.8.: The layout of the muon system consisting of the thin gap chambers, cathode strip chambers, monitored drift tubes, resistive plate chambers and the toroidal magnet system.

Muon chambers which are used for trigger decisions cover a range of $|\eta| < 2.4$ with RPCs in the region $|\eta| < 1.05$ and TGCs in the end-cap region of $1.05 < |\eta| < 2.4$ The two resistive plates serving as electrodes are made of phenolic-melaminic plastic laminate and the gaps are filled with a gas mixture of $C_2H_2F_4$, Iso-C_4H_10 and SF_6. It has a fast response with a time resolution of 1.5 ns at the nominal operating voltage of 9.8 kV.
The TGC system is similar to the CSC but with smaller electrode spacing and CO_2/n-pentane as a gas mixture so the spatial resolution is worse but the time resolution is only 4 ns which is necessary for triggering.

3.2.5. Trigger and Data Acquisition

As mentioned in Section 3.1 a proton interaction rate of 1 GHz can lead to approximately 60 $\frac{\text{Tb}}{\text{s}}$ of data which is truly challenging in terms of processing and data storage. Only 300 $\frac{\text{Mb}}{\text{s}}$, equivalent to a rate of 200 Hz, can be stored. The ATLAS trigger system (Fig. 3.9) has to reduce the initial data rate by five orders of magnitude. Only one single event out of 200 000 can be stored and one has to be very careful which events are selected not to reject interesting physics events. ATLAS uses a three-level trigger system for online event selection:

- The Level 1 Trigger (LVL1) is completely hardware-based, i.e. FPGAs and other electronics are used for logical operations. Its task is to decide whether the event is of general physics interest in order to reduce the data rate to 100 kHz. Since the trigger works synchronized with the data taking the decision has to be taken within 2.5 μs after the event occurs, therefore the hardware is integrated into the detector parts. The data information is stored in pipeline memories while the LVL1 trigger is working.
  The decision is based on the muon and calorimeter system only. If a muon is identified by the RPC and TGC the transverse momentum is estimated using look-up Tables depending

on the hits because there is not enough time to reconstruct the track and calculate the momentum. The calorimeter trigger uses a coarse granularity and looks especially for high p_T electrons, photons, jets and a large total transverse energy along with large missing transverse energy. If LVL1 accepts the event, the geometry of the triggered object is passed as the Region of Interest (ROI) to the next trigger.

- The Level 2 Trigger (LVL2) is completely software based running on dedicated software farms. The LVL2 analyses each ROI in the detector including additional detector subsystems with full granularity and the Inner Detector tracking information. With 10 ms processing latency LVL2 can run more complex algorithms for the event-driven sequential selection, but those still have to be kept as simple as possible and efficient. While LVL2 refines the selection further to a data rate of 1 kHz the detector information is stored in Readout Buffers (ROBs).

- The third and final trigger, the Event Filter (EF) is also software based with a latency in the order of a second. During this time, the whole event is reconstructed based on calibration and alignment information obtaining the global event from the ROBs. Furthermore, extended tasks such as vertex reconstruction, final track fitting and calculation of global $\not{E}_T$ can be performed. first time the pure detector signal which can be measured for example in voltage is formed into physics objects like jets or leptons. The LVL2 and EF comprise the ATLAS high-level trigger (HLT) system. After the data rate is reduced to 200 Hz the passing objects are distributed to storage elements all over the world (GRID) or may be also recorded to special storage elements if the data is needed for alignment or calibration.

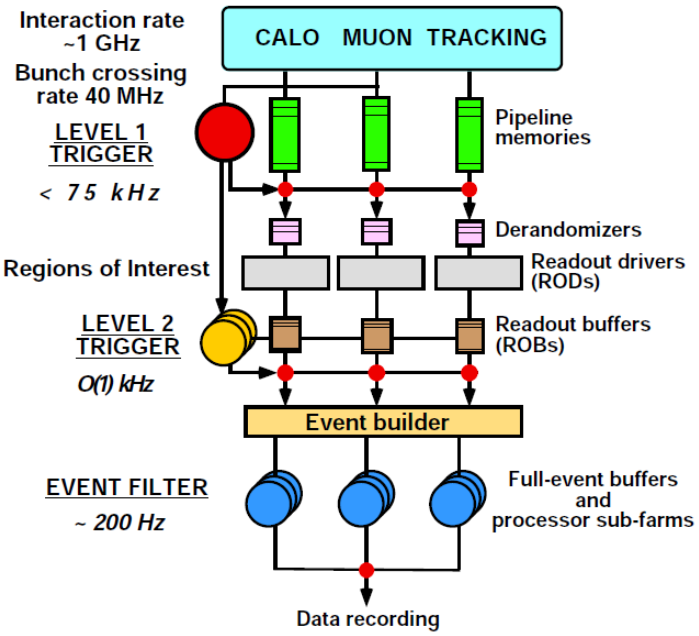

Figure 3.9.: A schematic of the ATLAS Trigger System is shown consisting of Level 1, Level 2 and the Event Filter.

4. Kinematic Fitting

Experiments in high-energy physics generate data samples, which are used to test the underlying theory or to determine the values of the model's free parameters. The estimated value can vary on an event-by-event basis. Consequently, one tries to find an estimator based on the entire data set and the knowledge about the physical process. This estimator should be an accurate estimate with a well defined uncertainty. The properties of the final state particles of the $t\bar{t}$ decay, such as energy and angular variables, can be measured only within uncertainties, e.g. the accuracy is limited by the detector resolution. Apart from this the measured jets give no information about the assignment of the jets to the parton. In the lepton + jets channel there are in principle 24 possible combinations in the assignment of the four jets (see Sec. 2.2.3). The concept of kinematic fitting allows for identifying the jets to the partons and for finding better estimators for the measured quantities by using kinematic constraints from the assumed model.

4.1. Parameter Estimation

4.1.1. Estimators

Generally, an estimator $\hat{a}$ is a function of the data, whose estimate is a meaningful guess for the value of the model parameter [4]. *Good* estimators are required to have the following properties [55, 56]:

- For an increasing data set with N elements the difference between the estimator $\hat{a}$ and the true value a should vanish. An estimator is called *consistent* if the following equation holds:

$$\lim_{N\to\infty} \hat{a} = a \quad . \tag{4.1}$$

- The estimator is called *unbiased* if its fluctuations to higher and lower values balance, meaning

$$\langle \hat{a} \rangle = a \quad , \tag{4.2}$$

  where $\langle \hat{a} \rangle$ is the expectation value of the estimator.

- The spread of the values should be small. So the estimator is *efficient* if its variance $V(\hat{a})$ is small. However, there is an upper limit on the accuracy of an unbiased estimator namely the minimum variance bound (MVB).

These are only the most important properties, sometimes robustness is also important, which is the property of being insensitive to variations from the model assumptions. In general there is no perfect estimator and one has to weigh which property is the most important one for the specific application.

4.1.2. The Likelihood Function

In statistics one usually defines probabilities for a particular outcome based on known parameters. For testing a theoretical model in physics it behaves the other way around. Given a particular data sample $\boldsymbol{x} = \{x_1, x_2, x_3, ..., x_N\}$ one is interested in estimating the unknown parameters $\boldsymbol{a} = (a_1, a_2, a_3, ..., a_m)$ of the model or in validating the model hypothesis. With *Bayes*' theorem one can easily reverse the described conditional probabilities:

$$P(\boldsymbol{a}|\boldsymbol{x}) = \frac{P(\boldsymbol{x}|\boldsymbol{a})P(\boldsymbol{a})}{P(\boldsymbol{x})} = \frac{P(\boldsymbol{x}|\boldsymbol{a})P(\boldsymbol{a})}{\int P(\boldsymbol{x}|\boldsymbol{a'})P(\boldsymbol{a'})d\boldsymbol{a'}} \quad , \tag{4.3}$$

where $P(\boldsymbol{x})$ and $P(\boldsymbol{a})$ are the prior probability density functions (p.d.f) of the data set $\boldsymbol{x}$ and the unknown parameters $\boldsymbol{a}$ before the measurement. In the Bayesian approach the posterior p.d.f. $P(\boldsymbol{a}|\boldsymbol{x})$ contains all knowledge about the parameters $\boldsymbol{a}$, given the data $\boldsymbol{x}$. The denominator in Equation 4.3 serves to normalize the posterior p.d.f. to unity. There is no general rule to determine the prior $P(\boldsymbol{a})$. If applicable it can simply be set to a constant within a certain range and zero outside this range.
The reversed probability $P(\boldsymbol{x}|\boldsymbol{a})$ to have $\boldsymbol{x}$ obtained given the model parameters $\boldsymbol{a}$ is interpreted as the likelihood function $\mathcal{L}(\boldsymbol{a}) \equiv P(\boldsymbol{x}|\boldsymbol{a})$, which is evaluated with the data $\boldsymbol{x}$. Generally, the measurements x_i are statistically independent and each follows the p.d.f $P(x_i|\boldsymbol{a})$, so that the joint p.d.f for $\boldsymbol{x}$ can be factorized and the likelihood function is

$$\mathcal{L}(a_1, a_2, a_3, ..., a_m) = \prod_{i=1}^{N} P(x_i|\boldsymbol{a}) \quad , \tag{4.4}$$

formed by the product of the individual probabilities $P(x_i|\boldsymbol{a})$, which are calculated according to the model.
The likelihood function can include information from theory as well as from the modeling of the experimental conditions. This is simply done by multiplying probability densities coming from constraints on the parameters, for example energy- and momentum-conservation (kinematics). In this way one can use physics information in order to gain more precise estimators by using the approach described in the next section.

4.1.3. The Maximum Likelihood Method

The maximum likelihood (ML) method, invented by C.F. Gauß, is one consistent way to build estimators. The ML estimator (MLE) $\hat{a}$ is the value of a for which the likelihood (Equation 4.4) is maximized. This means, the MLE is not the most likely value but makes the data most likely (given the model) and is therefore for small samples not always the best estimator. For example, it is in general consistent, but not efficient and unbiased for finite N. This is the price one has to pay for the invariance of the MLE under one-to-one parameter transformations, which is truly an important feature of the ML method [56]. In the special case of a constant prior p.d.f., the mode of the posterior is equal to that of the MLE. Following the *central limit theorem*, the MLE becomes unbiased for large samples with the variance equal to the MVB:

$$V(\hat{a}) = \frac{1}{\left\langle \left(\frac{\mathrm{d}\ln\mathcal{L}}{\mathrm{da}}\right)^2 \right\rangle} \quad . \tag{4.5}$$

Because the product of arbitrary probability densities is usually not easy to derivate, the logarithm of $\mathcal{L}$ is built to obtain the MLE:

$$\frac{\partial \ln \mathcal{L}(x_1, x_2, ..., x_N | a_1, a_2, ..., a_m)}{\partial a_j} = \frac{\partial}{\partial a_j} \sum_{i=1}^{N} \ln P(x_i|\boldsymbol{a}) = 0 \quad \forall \quad \text{j=1, 2, ..., m} \quad . \tag{4.6}$$

Owing to its monotony the derivative of $\ln \mathcal{L}$ returns the same estimator. Especially for a higher dimensional parameter space this cannot be solved analytically, so one has to use numerical techniques minimizing $(-\ln \mathcal{L})$. Most of these techniques do not provide any quality factor or goodness-of-fit. If the primary assumptions about the parent distributions $P(x_i|a)$ are wrong one cannot notice that from the results of the fit. One has to be careful with the underlying model determining the probability distributions.

4.2. Kinematic Fitting of $\pi^0 \to \gamma\gamma$

For illustration, a brief overview of kinematic fitting using the maximum likelihood method is given by applying the method to the simple example of neutral pion decay. Neutral pions π^0 have a mass of 134.9766 ± 0.0006 MeV and decay in roughly 99 % of the events into two photons with a mean life time of $(8.4 \pm 0.6) \cdot 10^{-17}$ s [4]. The leading order Feynman diagram of the neutral pion decay is shown in Figure 4.1.

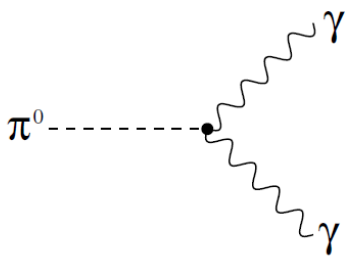

Figure 4.1.: The leading order Feynman diagram of the neutral pion decay.

Suppose that the two energies of the photons $\tilde{E}_1, \tilde{E}_2$ are both measured with the uncertainty σ. The kinematic fit allows for finding better estimators E_1, E_2 for the measured energies by using the kinematic constraint that the invariant mass of the two photons has to be close to the mass of the pion. For simplicity the following assumptions are made:

- The fitting parameters E_1, E_2 are Gaussian distributed around the measured values within a width of σ.
- The invariant mass of the two photons is Gaussian distributed within a width of σ_{π^0} around the pion mass M_{π^0}.
- The directions of the two photons are perfectly measured.

The invariant mass $m_{\gamma\gamma}$ of the two massless photons can be calculated by adding the four-momentum vectors p_i of the photon:

$$m_{\gamma\gamma}^2 = (p_1 + p_2)^2 = 2E_1E_2(1 - \cos\theta) \ , \tag{4.7}$$

where θ is the angle between the two photons in the laboratory frame. Consequently, the resulting likelihood function is given by

$$\mathcal{L} = \frac{1}{2\pi\sigma^2}\prod_{i=1}^{2}\left[\exp\left(\frac{-\left(\tilde{E}_i - E_i\right)^2}{2\sigma^2}\right)\right]\frac{1}{\sqrt{2\pi\sigma_{\pi^0}^2}}\exp\left(\frac{-\left(m_{\gamma\gamma} - M_{\pi^0}\right)^2}{2\sigma_{\pi^0}^2}\right) \quad . \tag{4.8}$$

Taking the logarithm yields

$$\ln\mathcal{L} = \sum_{i=1}^{2}\left(-\frac{\left(\tilde{E}_i - E_i\right)^2}{2\sigma^2}\right) - \frac{\left(m_{\gamma\gamma} - M_{\pi^0}\right)^2}{2\sigma_{\pi^0}^2} - \ln\left(2\pi\sigma^2\right) - \frac{1}{2}\ln\left(2\pi\sigma_{\pi^0}^2\right) \quad . \tag{4.9}$$

Because only the extremum is of interest the constant logarithmic terms and the factor $-\frac{1}{2}$ can be dropped. With the mass constraint of Equation 4.7 the $\ln\mathcal{L}$ can be written as

$$\ln\mathcal{L} = \frac{1}{\sigma^2}\left(\left(\tilde{E}_1 - E_1\right)^2 + \left(\tilde{E}_2 - E_2\right)^2\right) + \frac{\left(\sqrt{2E_1E_2(1-\cos\theta)} - M_{\pi^0}\right)^2}{\sigma_{\pi^0}^2} \quad . \tag{4.10}$$

Finally the partial derivatives of $\ln\mathcal{L}$ with respect to both fitting parameters are set to zero, which lead to a solvable system of equations.

$$\frac{\partial\left(\ln\mathcal{L}\right)}{\partial E_1} = -\frac{2\left(\tilde{E}_1 - E_1\right)}{\sigma^2} + \frac{2E_1E_2(1-\cos\theta) - M_{\pi^0}\sqrt{2E_1E_2(1-\cos\theta)}}{E_1\sigma_{\pi^0}^2} \stackrel{!}{=} 0 \quad , \tag{4.11}$$

$$\frac{\partial\left(\ln\mathcal{L}\right)}{\partial E_2} = -\frac{2\left(\tilde{E}_2 - E_2\right)}{\sigma^2} + \frac{2E_1E_2(1-\cos\theta) - M_{\pi^0}\sqrt{2E_1E_2(1-\cos\theta)}}{E_2\sigma_{\pi^0}^2} \stackrel{!}{=} 0 \quad . \tag{4.12}$$

From this system of equations one obtains the fitting parameters E_1 and E_2. Without the constraining term the fit would just return the measured values, but with the mass constrained the fitting parameters are on average closer to the true values compared to the measured ones [57]. By using a kinematic constraint one can reach energy resolutions beyond the detector resolution.

4.3. The KLFitter Package

The Kinematic Likelihood Fitter (KLFitter) [58] is a package written in C++ for the estimation of precise physical parameters using the maximum likelihood method. The structure is based on ROOT [59] and the numerical maximization of the likelihood is performed by the Bayesian Analysis Toolkit (BAT) [60] which also uses MINUIT [61]. The KLFitter works stand-alone, but is also implemented in the *Athena* software framework used in the ATLAS experiment (TopKLFitter) [62]. Given a particular event topology the KLFitter maximizes the likelihood in consideration of the assumed kinematics and particle properties.
Although it is a general package which can be applied to any user-defined event topology, only $t\bar{t} \to e + \ jets$ events will be discussed in the following because this channel of the $t\bar{t}$ decay scheme will be studied as an example in this thesis. As described in Section 2.2.3, the well-known decay results in four jets, a high-p_T electron and $\not{E}_T$. Two jets are produced by light-quarks coming from the hadronically decaying W boson and two jets are b-jets coming from the decay of the

two top quarks.

The following measured quantities define the data set:

- energies $\tilde{E}_i$ and directions $\tilde{\Omega}_i = (\tilde{\eta}_i, \tilde{\phi}_i)$ of the four jets;
- energy $\tilde{E}_e$ and direction $\tilde{\Omega}_e = (\tilde{\eta}_e, \tilde{\phi}_e)$ of the electron
- missing transverse energy $\not{E}_T$ (x- and y-components).

The direction of the electron is assumed to be measured with negligible uncertainty. The energies of the quarks and the electron and the angular distributions of the quarks are measured with non-vanishing uncertainties. These uncertainties are not necessarily symmetrically distributed and can vary in different energy- and η-regions. treatment so the resolutions are parametrized by transfer functions $W(\tilde{E}_i, E_i)$. The likelihood approach allows for the very general treatment of parameterizing the resolutions by transfer functions $W(\tilde{E}_i|E_i)$ and $W(\tilde{\Omega}_i|\Omega_i)$, which map the measured energies $\tilde{E}_i$ and angles $\tilde{\Omega}_i$ of the objects to the true energies and angles of the final state particles.
Although neutrinos leave no direct signal in the detector, the momentum of the neutrino can be obtained by applying energy- and momentum-conservation to all measured objects. Because of its vanishing mass the neutrino momentum is also parametrized by transfer functions $W(E_{x,y}^{\text{miss}}|p_{x,y}^{\nu})$. The parametrization of the transfer functions is described in detail in Section 5.4. In the theoretical model of the KLFitter it is assumed that all transfer functions are known and all jets are detected. Furthermore, the $t\bar{t}$ decay is considered in the leading order picture which means that all jets originate from the $t\bar{t}$ decay and no jets coming from ISR/FSR are considered.

4.3.1. Constraints

For setting up the likelihood function the physics model of the $t\bar{t}$ decay is used. As a first constraint the invariant di-jet mass m_{jj} and the invariant mass of the electron and the neutrino $m_{e\nu}$ coming from the decaying W boson are required to be Breit-Wigner (BW) distributed around a pole mass of $M_W = 80.4$ GeV within a width $\Gamma_W = 2.1$ GeV [4]. Accordingly, these probability densities constrain the combined momenta of the two light quarks and the combined momenta of the electron and the neutrino (see App. A.1). the the invariant masses follow its distribution. The normalized and relativistic BW function for a mass m centered around M is given by

$$BW(m|M) = \frac{2}{\pi} \frac{\Gamma M^2}{(m^2 - M^2)^2 + \Gamma^2 M^2} \quad . \tag{4.13}$$

For illustration, the true hadronic W boson mass coming from a simulation of $t\bar{t} \rightarrow e + jets$ events is fitted with the BW-function in Figure 4.2. Particularly in the tail regions the distribution is not Gaussian-like. As expected, the fitted pole mass of 80.41 GeV and the width of 2.153 GeV are very close to the MC truth values.
As a second constraint the invariant top quark masses m_{jjj} and $m_{e\nu j}$ follow also a Breit-Wigner distribution. The user can choose whether the top pole mass is an additional free parameter or is fixed to a certain value. This value can come from previous measurements or, like in this case, the value equals the one which is used in the Monte Carlo generation ($M_t = 172.5$ GeV). In the current implementation, the decay width of the top mass is independent of the pole mass

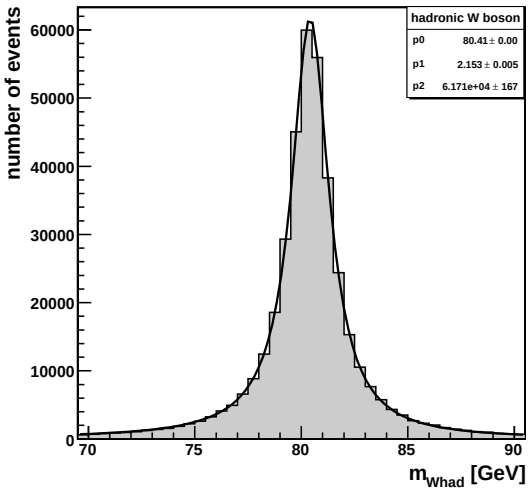

Figure 4.2.: The true hadronically decaying W boson is fitted with a Breit-Wigner function. The first fitting parameter corresponds to the pole mass, the second to the width and the third to the amplitude.

and is set to $\Gamma_t = 1.5$ GeV. The derivation of the invariant masses depending only on the fit parameters can be found in Appendix A.1.
Particles and Antiparticles are not treated differently, in particular $M_{W^+} = M_{W^-}$ and $M_t = M_{\bar{t}}$ which implies CPT invariance. Both constraints give sensitivity to the combinatorial assignment of jets to partons. In addition each constraint increases the degrees of freedom k in the fit, which has to be at least one to enable a kinematic fit:

$$k = N - M + P \ , \tag{4.14}$$

where N is the number of variables, M the number of fit parameters and P the number of constraints.

4.3.2. Fit Parameters

Taking the transfer functions of the measured objects and the constraints into account the following 17 parameters are used in the fitting procedure:

- energies of the four quarks E_i and the electron E_e (5 parameters);
- angular variables $\Omega_i = (\eta_i, \phi_i)$ of the four jets ($2 \times 4 = 8$ parameters);
- momentum components of the neutrino $p^{\nu}_{x,y,z}$ (3 parameters);
- optionally the top pole mass M_t (1 parameter).

Each parameter is varied in the kinematic fit within a certain range. The ranges of the energies, the angular variables and the x- and y-components of the neutrino momentum are set individually for each event around the measured values:

- $E_i \in \left[\min\left(0, \tilde{E}_i - 7 \cdot \sqrt{\tilde{E}_i}\right),\ \tilde{E}_i + 7 \cdot \sqrt{\tilde{E}_i}\right]$

- $E_e \in \left[\min\left(0, \tilde{E}_e - 2\cdot\sqrt{\tilde{E}_e}\right),\ \tilde{E}_e + 2\cdot\sqrt{\tilde{E}_e}\right]$
- $p_{x,y}^{\nu} \in \left[E_{x,y}^{\text{miss}} - 100,\ E_{x,y}^{\text{miss}} + 100\right]$
- $p_z^{\nu} \in [-1\,000,\ +1\,000]$
- $\eta_i \in [\tilde{\eta}_i - 0.2,\ \tilde{\eta}_i + 0.2]$
- $\phi_i \in \left[\tilde{\phi}_i - 0.1,\ \tilde{\phi}_i + 0.1\right]$
- $M_t \in [100,\ 1\,000]$

The ranges of the energies, momentum and mass are all given in GeV, the ranges of the angular variables in radians. The energies of the partons and the energy of the lepton need to be within a range of seven and two times the standard deviations of the measured value, respectively, and they are required to be positive. The z-component of the neutrino momentum has to be within a range of $\pm 1\,000$ GeV. The pole mass of the top quark M_t is constrained to be between 100 GeV and 1 000 GeV, such that it is significantly larger than the pole mass of the W boson but is limited to reasonable values.

4.3.3. Likelihood

Finally, the likelihood function for $t\bar{t} \to e + \ jets$ events can be defined:

$$\begin{aligned}\mathcal{L} \ = \ & \left(\prod_{i=1}^{4} W(\tilde{E}_i|E_i)\right) \cdot W(\tilde{E}_e|E_e) \cdot W(E_x^{\text{miss}}|p_x^{\nu}) \cdot W(E_y^{\text{miss}}|p_y^{\nu}) \cdot \left(\prod_{i=1}^{4} W(\tilde{\Omega}_i|\Omega_i)\right) \cdot \\ & BW(m_{jj}|M_W) \cdot BW(m_{e\nu}|M_W) \cdot BW(m_{jjj}|M_t) \cdot BW(m_{e\nu j}|M_t) \ . \end{aligned} \tag{4.15}$$

As indicated in Section 2.2.3 the negative loglikelihood $(-\ln\mathcal{L})$ has to be minimized in the global parameter space for all possible permutations associating a jet with a parton. Because the likelihood function is invariant under the permutation of the two light quarks, there are 12 permutations for exactly four selected jets. In principle three options for the different minimization techniques can be chosen: *Marcov Chain Monte Carlo* (MCMC) sampling, *Simulated Annealing* (SA) or MINUIT . In case of MCMC and SA additionally MINUIT is used in the mode of the likelihood distribution of a single fit in order to further improve the accuracy of the fit. Since SA and MINUIT minimization critically depend on the initial conditions, the starting values are set to the measured values or are calculated in case of the top mass m_t and the neutrino p_z^{ν}[1] from the kinematics of the measured values. By default, MINUIT is chosen as minimization technique, but in a few percent of the events no minimum can be found by MINUIT for a specific permutation. In that case the minimization is repeated with SA. The best parameters found by SA are then passed to MINUIT again and used as starting values for a new minimization. If still no minimum is found by MINUIT , these permutations are discarded.
Apart from the fit parameters for each permutation and the corresponding likelihood value, the KLFitter also returns the *best permutation* which is the jet permutation with the largest likelihood value.

[1] The more likely value of the two neutrino p_z^{ν} solutions is used (see App. A.2).

5. Used Monte Carlo Data

Not only in absence of real data but also during the data taking process Monte Carlo (MC) simulated data are essential for detector understanding and physics analyses, e.g. to compare data with MC.
For the studies presented in this thesis, a Monte Carlo data sample with di-leptonic and semi-leptonic final states has been used[1]. The sample has been created during the central ATLAS MC08 production in run 5200 and has been generated with MC@NLO version 3.1 [63] with a centre-of-mass energy of 10 TeV and assuming a top mass of 172.5 GeV [64]. The MC@NLO generator simulates final states with next-to-leading order (NLO) accuracy using the parton density function CTEQ6M [32], which are then passed to a parton shower MC with leading-logarithmic (LL) accuracy. The $t\bar{t}$ decay and the parton shower process (fragmentation and hadronization) are simulated by the JIMMY [65] plug-in for HERWIG [66] which allows to generate multi-parton interactions and thus to model underlying events.
The event generation (e357), detector simulation through GEANT4 (s462), digitization and reconstruction has been performed with Athena version 14.2.21.1 in the ATLAS geometry ATLAS-GEO-02-01-00. The sample has been re-reconstructed to avoid known issues of former reconstruction versions so the reconstruction tag has been changed to r635_t53. Since the sample contains all possible decay channels but no fully hadronic decay of the $t\bar{t}$-system the sample cross section is reduced by roughly 46 % to 202.86 pb compared to the full $t\bar{t}$ cross section at a centre-of-mass energy of 10 TeV (see Eq. 2.4). The MC sample is scaled in order to match this higher order calculations by a so called *K-factor* of 1.07. The total number of events in the sample is roughly 2 million.

5.1. Object Definitions

The following object definitions are used for these studies [67]:

- Jets are built from calorimeter towers (0.1×0.1 in η-ϕ), which are calibrated with a global cell weighting approach (H1). The cell weights are obtained by a parametrization in energy density from a di-jet sample. The jets are further reconstructed with an iterative seeded fixed-cone jet finder [68] with a split and merge procedure. The ΔR cone size is set to 0.4 and a jet is requested to have p_T >15 GeV and $|\eta| < 2.5$. If a jet overlaps with an electron within a $\Delta R < 0.4$ the (closest) jet is removed.

- For the reconstruction of electrons, rectangular clusters with a fixed size are formed out of a seed in the electromagnetic calorimeter cells. The position is optimized in order to maximize the amount of energy within the cluster which is referred to as the sliding window algorithm [69]. For each of the reconstructed clusters a matching track which does not belong to a photon-conversion pair needs to be found within a $\Delta\eta \times \Delta\phi$ window of 0.05×0.10 and with a momentum fitting to the cluster energy $\left(\frac{E}{p} < 10\right)$. Three

[1] mc08.105200.T1_McAtNlo_Jimmy.merge.AOD.e357_s462_r635_t53.

different quality levels are defined based on cuts on the shower variables [67]: loose, medium and tight. For these studies the medium quality level is used; the electron has to be isolated within a $\Delta R < 0.2$ and p_T >15 GeV and $|\eta| < 2.47$ is required. The crack region ($1.37 < |\eta| < 2.52$) between the barrel and the end-caps of the electromagnetic calorimeter is excluded.

- Ideally, the x- and y-component of the missing transverse energy should be the negative sum of the energy x- and y-components of all physics objects. In ATLAS this is calculated from the energy deposited in all calorimeter cells, which are associated with a parent reconstructed and identified high-p_T object and from muon information. A refined calibration of the object (electron, photon, tau, jet) is used to determine the weights of the calorimeter cells above a noise suppression threshold. Additionally, cells outside objects are globally calibrated with H1 weights and also added. The contributions by muons are calculated separately for isolated and non-isolated muons measured by the muon spectrometer and calorimeter cells. For these studies the definition MET_RefFinal is used for $\not{E}_T$ which is the sum of refined calorimeter cells, cells outside objects, muon contribution and cryostat corrections due to losses in the cryostat.

5.2. Event Selection

5.2.1. Preselection

The Göttingen n-tuple maker GoTopTree in version 01-03-00 is used to create flat root-tuple and to split the sample according to the decay channel. This is done via a pre-selection on truth level. For the following studies only $t\bar{t}\rightarrow$ (τ, μ + jets$\rightarrow$) $e\nu$ + jets is used, so all events are required to have exactly one electron, at least two b-quarks and two light quarks in MC truth. This includes events, in which one W boson decays into a tau lepton, which further decays into light jets. The lepton + jets decay mode corresponds to 34.73 % of the total sample.
In order to further skim the sample it is also asked for at least one reconstructed electron and one reconstructed jet. There might be no electrons found in the reconstruction because the electron is misidentified as a jet or its direction is beyond the detector acceptance. A jet might not be reconstructed due to the efficiency of the jet algorithm, the overlap removal, the acceptance of the detector or because the jet is reconstructed as an electron or has low transverse momentum. In the jet algorithm several jets might be identified as one due to the split and merge procedure with a fixed ΔR cone size. This happens particularly often if the W boson is highly boosted and decays hadronically, or the top quark is highly boosted and the jet coming from the b-quark overlaps with the jets coming from the further decaying W boson. However, it happens very rarely that none of the four jets are reconstructed in the $t\bar{t}$ sample. In total 236 653 events pass these pre-selection, which correspond to roughly 57 % of the events (see Tab. 5.1).

5.2.2. Selection Cuts

After the preselection additional selection criteria are applied in order to obtain well reconstructed events and a pure signal. The cuts which are used in this studies are the ones which are presented in the CSC analyses [67]. A similar selection will be applied when analyzing measured data. There it will be essential to discriminate the signal process from background processes. The cut flow and the criteria are presented in Table 5.1.
The Table shows that 87 684 events pass all selection criteria, which is quoted to get an idea of the statistics in the sample. The cross section is reduced from 75.39 pb to 16.05 pb which corre-

Table 5.1.: Cut flow of the $t\bar{t}$ sample with all weights and correction factors applied given for number of events, cross section σ, relative ϵ_{rel} and absolute ϵ_{abs} cut efficiencies. The numbers represent the statistics of the sample and thus an arbitrary integrated luminosity.

Cut	N_{events}	σ in pb	ϵ_{rel}	ϵ_{abs}
no	411 807	75.39	1.00	1.00
Pre-selection	236 653	43.32	0.57	0.57
1 isolated electron with $p_T > 20$ GeV and $\lvert\eta\rvert < 2.5$	217 728	39.85	0.92	0.53
at least 3 jets with $p_T > 40$ GeV and $\lvert\eta\rvert < 2.5$				
& at least 1 additional jet with $p_T > 20$ GeV and $\lvert\eta\rvert < 2.5$	98 815	18.09	0.45	0.24
$\not{E}_T \geq 20$ GeV	87 684	16.05	0.89	0.21

sponds to an absolute cut efficiency of roughly 21 %. For an integrated luminosity of 200 pb^{-1} about 3 210 events pass the selection[2].
There might be more electrons found in the reconstruction, because hadrons fake electrons (e.g., pions misidentified as electrons) or secondary electrons are generated in photon conversion or radiated from jets. Additional reconstructed jets in the signal sample can be caused by ISR and FSR, fakes from the showering process, underlying events, soft scattering, leptons misidentified as jets or one jet reconstructed as several jets. Figure 5.1 shows the jet multiplicities before and after the selection, though a jet is only given if its $p_T > 20$ GeV.

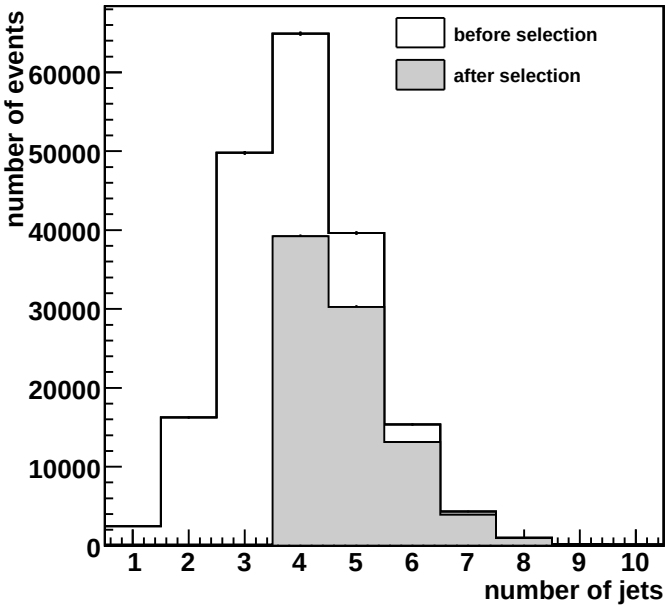

Figure 5.1.: Jet multiplicities of the $t\bar{t}$ signal MC sample before and after the selection.

Before the selection, there are many events with only two or three reconstructed jets with the required transverse momentum. If this is not caused by the momentum requirement it is due

[2]The goal for the LHC's first running period is an integrated luminosity of 200 pb^{-1}.

to the reasons described in Section 5.2.1. After the selection less than 50 % of the events have exactly four jets but more than 90 % of the events have four, five or six jets. One can also see that the relative reduction of events due to the $p_T > 40$ GeV cut is strongest in the 4-jet bin.

5.3. Truth Matching

For some studies, e.g. for extracting the transfer functions from the simulated data or for evaluating the reconstruction efficiency of the KLFitter, it is necessary to identify jets with their corresponding truth quark coming from the $t\bar{t}$ decay. One possibility to apply *truth matching* is via a geometric matching criterion in η-ϕ-space, where a reconstructed jet is associated with a truth quark if

$$\Delta R = \sqrt{(\phi_{\text{reco}} - \phi_{\text{truth}})^2 - (\eta_{\text{reco}} - \eta_{\text{truth}})^2} < 0.3 \ . \tag{5.1}$$

This identification might not be unique which is illustrated in Figure 5.2.

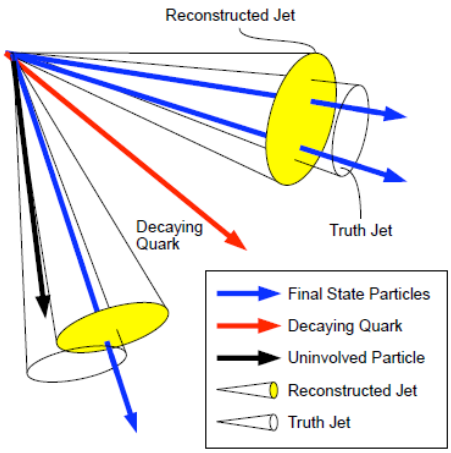

Figure 5.2.: The showering final state quark can be associated with its own jet or with a reconstructed jet which is caused by the another final state particle or by an uninvolved particle. Here it is also shown that showering the truth particle results in another jet than the reconstructed one [70].

The same requirement is applied for reconstructed electrons and truth electrons, but with a cone size of 0.1. An event is labeled *matched* if there is a one-to-one assignment of all truth partons coming from the leading order hard scattering process to reconstructed jets and if the truth electron is matched to a reconstructed electron. In particular, the event is not called matched if two or more quarks share one single jet, if one quark can be matched to more than one jet or if one quark cannot be associated to a jet.
The matching can be done for only the four highest jets in p_T or one can also include more jets if more jets are reconstructed in the selected event. Obviously the probability to match an event increases, the more jets are taken into account. One should not forget that although a jet is matched to a truth parton its association might not be unambiguous.
Because the matching efficiencies will be used for later studies of the performance of the KLFitter, the following calculated numbers are obtained from events which are not rejected in the fitting

procedure (see Sec. 4.3). In about 6 % of the events MINUIT cannot minimize the negative loglikelihood, thus the number of the selected events is reduced to 82 371. In approximately 1 % of the events the reconstructed electron can not be matched to the truth electron, so 81 589 of the events fulfill the electron matching criterion.
Furthermore, the jet truth matching is performed for the four highest jets in p_T regardless of the jet number in the event. This is also done separately for four, five and six jet events, where if applicable four, five or six jets are considered in the matching process. In order to evaluate the matching the *matching efficiency* ϵ_M is defined as the ratio of matched events N_M over the total number of events. The results are shown in Tab. 5.2.

Table 5.2.: The total number of events, the number of matched events and the resulting matching efficiencies are shown for the different number of jets in an event and number of used jets for the matching procedure.

Number of jets in event	Number of jets used for matching	N_{events}	N_M	ϵ_M in %
> 4	4	82 371	18 849	22.88 ± 0.17
4	4	36 864	13 499	36.62 ± 0.32
5	4	28 401	4 257	14.99 ± 0.23
5	5	28 401	13 963	49.16 ± 0.42
6	4	12 336	881	7.14 ± 0.24
6	5	12 336	3 473	28.15 ± 0.48
6	6	12 336	6 654	53.94 ± 0.66

The Table shows clearly the tendency that the more jets are taken into account for the matching procedure for a given jet multiplicity, the higher is the probability to match the event. In case of six jets in the event, the matching efficiency can be increased from only 7 % if four jets are used to 54 % if six jets are used. Note this matching is not necessarily correct because the probability to match with an uninvolved jet rises as well, if more jets are considered. In addition, one should be aware that ϵ_M is of course not the quantity to be optimized.

5.4. Parameterization of Transfer Functions

The detector response caused by a traversing particle is in general not a symmetric distribution around the true value. In particular the calorimeter shows a tendency to rather measure less energy due to losses, e.g. in dead material. Of course this depends on the detector geometry and is thus a function of, e.g. η. It is also a function of the energy of the particle because the shower processes depend on the material and sampling fraction of the detector and is broader if the particle has larger energy. Therefore the detector resolutions for energies E and angular variables Ω are parametrized by transfer functions $W(\tilde{E}_i|E_i)$ and $W(\tilde{\Omega}_i|\Omega_i)$, which give the probability density of a measured value given the true value in different η and energy bins. In this way the contribution to the resolution caused by radiation, hadronization or scattering as well as by the measurement process or reconstruction algorithm can be taken into account. The definition of a jet depends not only on the jet algorithm but also on the level of observation. This is visualized in Figure 5.3.
In the parton jet picture, gluons and quarks form a parton shower with the energy of the initial partons. The particle jet is obtained from reconstructed particles, e.g. pions and kaons, by

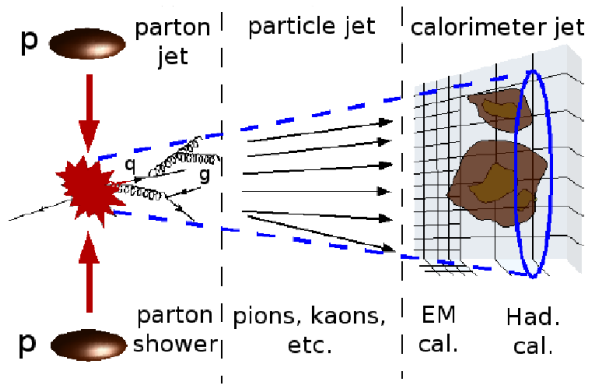

Figure 5.3.: The evolution of the partonic system is shown in the three different observation levels of parton, particle and calorimeter jet.

applying a jet algorithm to stable particles. The energy may differ because of invisible energy losses (neutrinos, nuclear excitations, etc.) or due to particles coming from an underlying event or scattering out of the jet cone of the algorithm. The calorimeter jet is formed from the raw calorimeter response and is affected by the detector properties, e.g. dead regions, non linear response or noise. results in a different jet energy compared to the particle jet. The mapping from the calorimeter jet to the particle jet is done by the calibration process correcting for most of the detector losses. However, cells without a physical context cannot be correctly calibrated and invisible particles and processes are not taken into account. The particle jet is then further mapped to the parton jet by the transfer functions.
The transfer functions are extracted from the Monte Carlo sample described in Section 5 with slightly changed requirements [71]. In order to minimize any possible bias, the p_T cut for all objects are changed to $p_T > 7$ GeV and no further selection is applied. To identify the reconstructed objects with their corresponding truth particle, truth matching (see Sec. 5.3) is applied.
The parametrization of the transfer functions for the energies is done separately for different types of objects distinguished in electrons, light jets, b-jets and $\not{E}_T$, and is modeled by double Gaussian functions in $\delta E = \frac{E_{\text{truth}} - E_{\text{measured}}}{E_{\text{truth}}}$ ($\not{E}_T$ is only a Gaussian function):

$$W(\delta E) = \frac{1}{\sqrt{2\pi}(p_2 + p_3 p_5)} \left[\exp\left(-\frac{(\delta E - p_1)^2}{2p_2^2} \right) + p_3 \exp\left(-\frac{(\delta E - p_4)^2}{2p_5^2} \right) \right] \quad , \tag{5.2}$$

where the parameter p_2 is parametrized according to the detector resolution with

$$p_2 = \frac{a_2}{\sqrt{E_{\text{truth}}}} + b_2 \quad , \tag{5.3}$$

and all other p_i are parametrized as linear functions of E_{truth}, i.e.,

$$p_i = a_i + b_i \cdot E_{\text{truth}} \quad . \tag{5.4}$$

Given these assumptions, ten parameters for each object and bin are obtained from a two-dimensional binned likelihood fit in which one dimension is the energy of the reconstructed object and the other dimension is the relative difference of the energies δE. So far, the η binning is chosen very coarse resulting in the interval borders [0, 1.0, 1.7, 2.5] which is motivated by

the detector geometry. The energy is divided into bins depending on the statistics within a single bin in order to minimize statistical uncertainties. The minimum energy depends on the objects and on the η-bin, while the maximum can be set to a user defined limit. In figure 5.4 the measured distributions of relative energy difference for light quarks and b-quarks are shown with the double Gaussian parametrization. The parameters p_i are further fitted in a global fit depending on the truth energy. These globally fitted parameters are used to define the transfer functions.

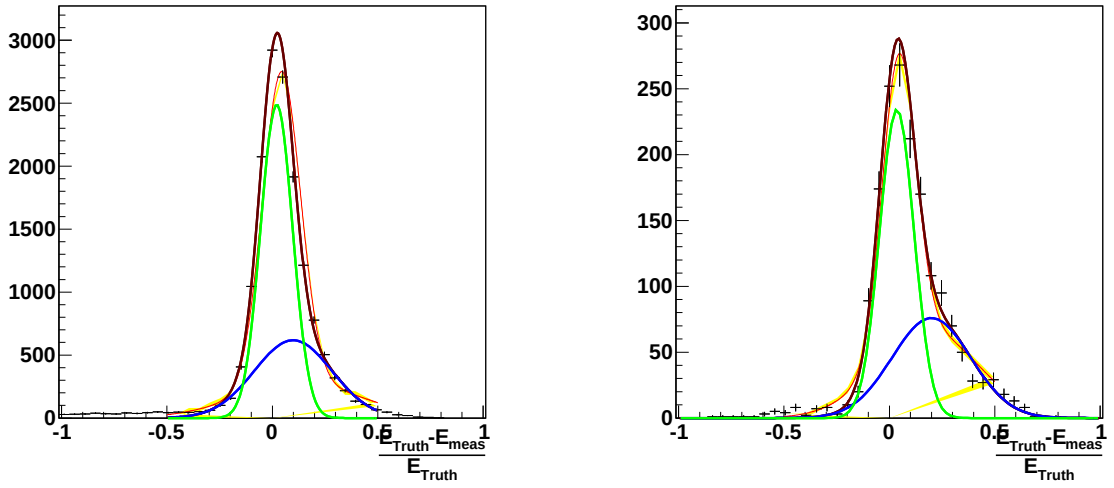

(a) transfer function of light quarks in $0 < \eta < 1.0$ and energy 130 GeV < E < 160 GeV

(b) transfer function of b-quarks in $1.7 < \eta < 2.5$ and energy 272 GeV < E < 302 GeV

Figure 5.4.: In both plots the parametrization with a double Gaussian (brown), its subcomponents divided into the two Gaussians (green, blue) and the global fit (red) with error band (yellow) of the transfer function can be seen.

Both of the transfer functions show an asymmetric tail on the right side of the distribution. This means that less energy is measured than generated in the Monte Carlo, which can be explained by the described losses in the detector.
contribution by supply material.
In the Appendix B further transfer functions of electrons, light quarks and b-quarks as well as the fitting of the parameters p_i can be found. The resulting parameters for the light quarks and the b-quarks within $1.0 < \eta < 1.7$ are summarized in Table 5.3.

With the given parameters the transfer functions for light quarks and b-quarks in the range $1.0 < \eta < 1.7$ are plotted for some truth energies in Figure 5.5.
The maximum of all transfer functions is at measured energy values below the truth energy of the initial parton. The larger the parton energy, the broader is the measured energy resolution because of the broadening in the hadronic showers. Moreover, the transfer functions for b-quarks are significantly broader than for the light quarks. Similar to the treatment of the energies, the transfer functions of the angular variables and the $\not\!\!E_T$ are parametrized by Gaussian functions.

Table 5.3.: The globally fitted parameters for the transfer functions of light quarks and b-quarks for the binning range of $1.0 < \eta < 1.7$. The unit for a_2 is $\mathrm{GeV}^{1/2}$ instead of the given one and b_2 is a dimensionless quantity.

	light quarks		b-quarks	
p_i	a_i	b_i in GeV^{-1}	a_i	b_i in GeV^{-1}
p_1	0.093 ± 0.002	(-2.64 ± 0.10)·10^{-4}	1.185 ± 0.023	(-1.24 ± 0.09)·10^{-4}
p_2	0.952 ± 0.033	(2.81 ± 0.29)·10^{-2}	1.006 ± 0.055	(2.23 ± 0.45)·10^{-2}
p_3	0.151 ± 0.015	(-2.83 ± 0.46)·10^{-4}	3.156 ± 0.238	(0.06 ± 0.67)·10^{-4}
p_4	0.193 ± 0.016	(-4.37 ± 0.82)·10^{-4}	0.273 ± 0.011	(-4.71 ± 0.55)·10^{-4}
p_5	0.342 ± 0.015	(-2.45 ± 0.63)·10^{-4}	0.317 ± 0.009	(-2.32 ± 0.44)·10^{-4}

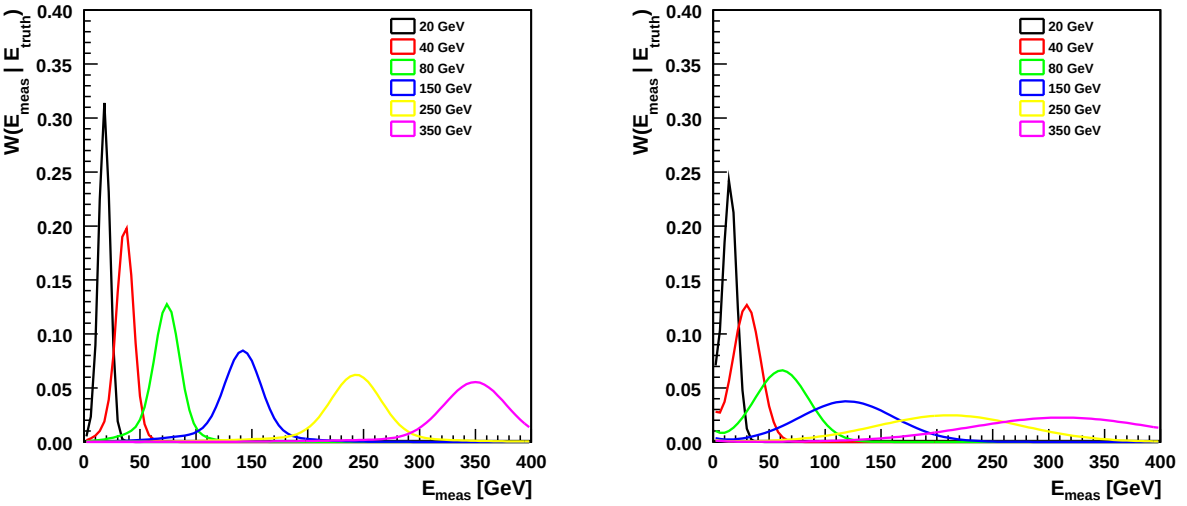

(a) transfer functions of light quarks

(b) transfer functions of b-quark

Figure 5.5.: The parametrized transfer functions for light quarks and b-quarks in the range $1.0 < \eta < 1.7$ are plotted versus E_{meas} for $E_{\mathrm{truth}} = (20, 40, 80, 150, 250, 350)$ GeV.

Further studies are ongoing to improve the parametrization in terms of binning, object definition and category and automatic extraction [71].

6. Top Pair Reconstruction with KLFitter in the e + jets Channel

The MC sample described in Section 5 is used to perform studies with the KLFitter. Slightly simpler transfer functions with different energy bins compared to the ones described in Section 5.4 are extracted from this sample and are used as an input to the fitting procedure [58]. The four highest jets in p_T are chosen to reconstruct the $t\bar{t}$ system regardless of the jet multiplicity, the other jets are ignored. As long as not explicitly stated, the default minimization procedure is chosen. For the following studies, the MC data is fitted once with free and once with fixed top pole mass in order to show the performance of the KLFitter separately for both constraints.

6.1. Likelihood Distributions and Permutation Probabilities

The mode of the likelihood distribution of a single fit defines the likelihood value for the specific permutation of the event. As mentioned in Section 4.3, the permutation with the largest likelihood value is defined as the *best permutation*. If matching is applied, one can define a *true permutation*, which is the permutation obtained by the association in the truth matching. The name true permutation might be misleading, it should be kept in mind, that the true permutation is not necessarily the correct permutation. For instance, one quark of the top decay could be matched to an uninvolved jet. If this and the other jets are then correctly assigned to their matched quarks, the permutation would be called true, although not all jets have their origin in the top decay. The values of the maximized $\ln \mathcal{L}$-function are shown in Fig. 6.1.
In case of a free top pole mass, the peak of the logarithmic likelihood distribution for the true permutation is slightly sharper than the one for the best permutation, because only matched events are considered. The distribution of the best and the second best permutation have well pronounced peaks around a logarithmic likelihood value of -24, but also side maxima around values of roughly -32 are visible. The main peak is more pronounced and shifted to larger values for the best permutation, whereas the second peak is larger for the second best permutation. Most of the events have logarithmic likelihood values between -50 and -20 in the best two permutations. In the distribution of the third best permutation the side maximum dominates the distribution and the peak around -24 is barely observable. The explanation for this arising shoulder is the wrong association of the jets to the partons of the decaying top quarks. That includes events in which jets are used in the reconstruction which are not caused by final state particles of the $t\bar{t}$ decay (see Sec. 6.6). The distribution of the worst permutation shows only the broad shoulder caused by the combinatorial background. The maximum is around logarithmic likelihood values of -47 and the distribution ranges approximately from values of -62 to -30. Thus the likelihood values of the best permutation can be clearly discriminated from the ones from the worst permutation.
In case of a fixed top pole mass the distributions are broader and shifted to smaller values. The additional constraint restricts the fit to reach larger likelihood values, but leads to a better jet-parton assignment and a better reconstruction of the kinematic of the event (see Sec. 6.2 - 6.4). The distribution of the best permutation peaks again around values of -24 but the maximum

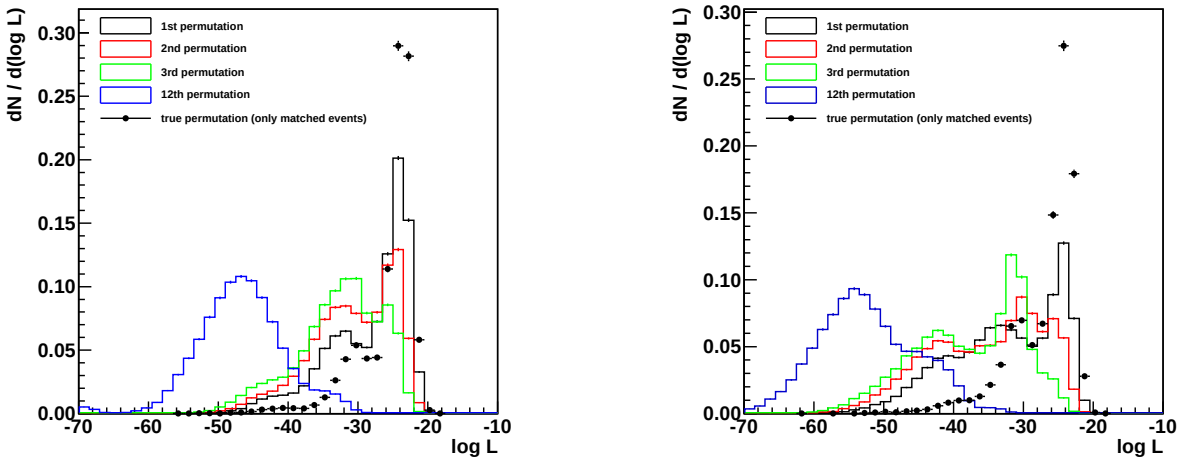

(a) free top pole mass

(b) fixed top pole mass

Figure 6.1.: The distributions of the maximized $\log \mathcal{L}$-values for the three best and the worst permutation are shown without matching required. The fit is performed with a free top pole mass (left) and with a fixed top pole mass (right). For comparison, the log likelihood in the true permutation for only matched events is shown.

is significantly smaller. The broad tail on the left side is much more pronounced and ranges to values down to -58. The distribution of the second best permutation has a very broad first peak around -30 and is less pronounced than the peak of the third best distribution around -32. The side maximum in the distribution of the best permutation arises at values around -32, whereas the broad shoulder in the distributions of the second and third best permutation arises at values of smaller than -40. The main peak of the third permutation is still larger than this shoulder. The distribution of the worst permutation shows a broad shoulder around -55 and ranges from values of -72 to -30.
Indeed, also the second or the third best permutation can return likelihood values close to the best permutation. In order to give a quantified measure for the separation of the permutation one can define the *permutation probability* p_i, which gives the probability of the permutation as the relative weight:

$$p_i(\text{correct}) = \frac{\mathcal{L}_\text{i}}{\sum_{\text{j=1}}^{\text{N}} \mathcal{L}_\text{j}} \quad , \tag{6.1}$$

where N is the number of possible permutations. In Fig. 6.2 the permutation probabilities for the three best, the worst and the true permutation are displayed.
No large differences in the distributions are visible whether the fixed top pole mass is used or not. One can see that only the permutation probability for the best permutation contributes to probabilities larger than 0.5 and in approximately 30 % of the events the permutation probability is very close to one. Only because of the logarithmic scale the likelihood distributions of the first three permutation seem to be close. The relative weight shows a clear discrimination. For all events the permutation probability of the second best permutation is smaller than 0.5 with roughly 30 % of the events in the zeroth bin. In more than 60 % of the events the third best

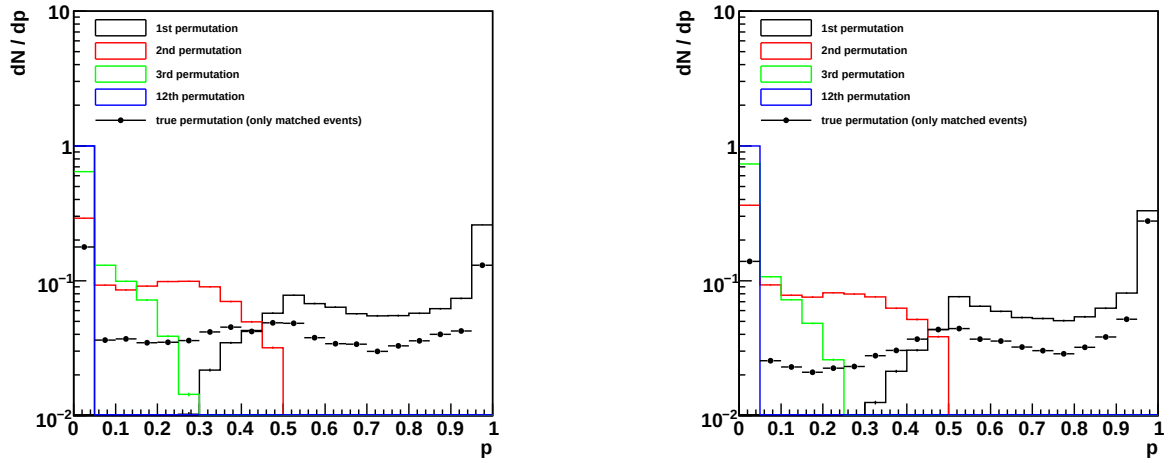

(a) free top pole mass

(b) fixed top pole mass

Figure 6.2.: The distributions of the permutation probability for the three best and the worst permutation are shown without matching required. The fit is performed with a free top pole mass (left) and with a fixed top pole mass (right). For comparison the relative weight for the true permutation (only matched events) is also shown.

permutation has a probability smaller than 0.05 and in all events this permutation probability is smaller than 0.3. The permutation probability of the worst permutation is in all events smaller than 0.05. The distribution of the true permutation is a mixture of all permutations and is rather flat distributed, except for two peaks at $p > 0.95$ and $p < 0.05$. Even though matching is required this distribution already gives an impression of how often the best permutation equals the true permutation.

6.2. Reconstruction Efficiencies

In order to evaluate the jet-parton association done by the KLFitter, reconstruction efficiencies are defined. Obviously only matched events can be taken into account for these studies. For example, the reconstruction efficiency ϵ_R for finding the correct permutation is estimated as the ratio of the number of events in which all jets are correctly assigned to the total number of matched events. In other words, this is the fraction of events in which the best permutation equals the true permutation. Similarly, efficiencies for the correct reconstruction of the hadronically decaying W boson and of the two b-quarks coming either from the hadronically or from the leptonically decaying top quark are calculated. With the same approach one can also estimate the potential to identify b-jets. The *b-tagging probability* is defined as the probability to associate a b-jet correctly with a b-quark, whereas the *misidentification probability* is defined for the case that a light jet is wrongly associated with a b-quark. With the assumption that only jets from the $t\bar{t}$-system are considered, the efficiencies can also be interpreted as the probability to find a correct configuration of jets with respect to the objects under study. This probability can be also calculated from pure combinatorics. A comparison of the reconstruction efficiencies with the statistical probabilities is shown in Figure 6.3.

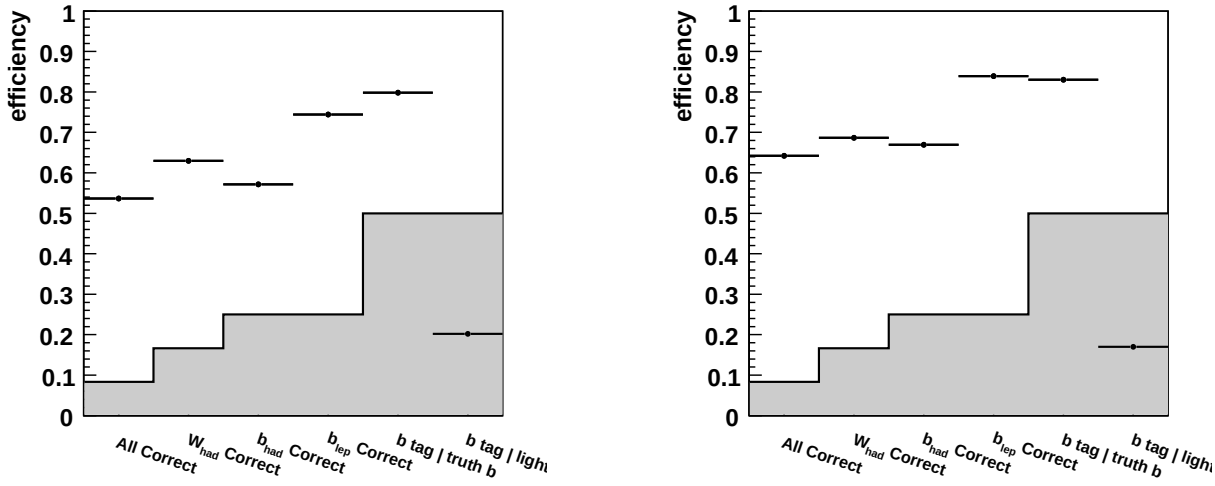

(a) free top pole mass

(b) fixed top pole mass

Figure 6.3.: The reconstruction efficiencies of the KLFitter (line) are compared to the statistical probabilities (gray shaded). Ordered by bin number the efficiencies for finding the correct permutation, the correct pair of quarks from the hadronically decaying W boson, the b-quark from the hadronically decaying top quark and the b-quark from the leptonically decaying top quark are shown. In the last two bins the b-tagging and the misidentification probability are shown.

Table 6.1 shows a summary of the obtained efficiencies with the corresponding uncertainties.

Table 6.1.: The reconstruction efficiencies for the two different top pole mass constraints are compared to the probabilities from random assignment.

	Statistical	Efficiencies in %	
	Probability in %	free top pole mass	fixed top pole mass
ϵ(all correct)	8.33	53.68 ± 0.55	64.22 ± 0.60
ϵ(hadronic W correct)	16.67	62.96 ± 0.59	68.66 ± 0.62
ϵ(hadronic b correct)	25.00	57.15 ± 0.56	66.97 ± 0.61
ϵ(leptonic b correct)	25.00	74.41 ± 0.64	83.89 ± 0.68
ϵ(b-tagging)	50.00	79.80 ± 0.67	83.02 ± 0.68
ϵ(misidentification)	50.00	20.20 ± 0.34	16.98 ± 0.31

In the two cases of a free and a fixed top pole mass the KLFitter finds the correct permutation of all jets in 53.68 % and 64.22 % of the events, respectively, while the pure statistical probability is only 8.33 %. The efficiencies for reconstructing the hadronically decaying W boson correctly are 62.96 % and 68.66 % for the two constraints, respectively, whereas only in 16.67 % of the events the W boson is correctly reconstructed by random assignment. It is less likely to reconstruct the b-quark from the hadronically decaying top quark correctly (57.15 % and 66.97 %) than to reconstruct the b-quark from the leptonically decaying top quark correctly (74.41 % and 83.89 %) for both constraints. Fixing the top pole mass leads again to higher efficiencies. The

statistical probability to assign one jet correctly to any quark is 25 %. The b-tagging probability is 79.80 % and 83.02 % in the cases of using the KLFitter with free and fixed top pole mass, respectively, while from combinatorics this is a coin flip decision with a probability of 50 %. The misidentification probability for this setup is exactly the complementary b-tagging probability. As expected fixing the top pole mass improves the performance significantly.
For these studies only matched events are taken into account, which means the reconstruction efficiencies might depend on the matching procedure. If the matching efficiency increases, the total number of correctly reconstructed events can increase, even if the reconstruction efficiency drops. In order to give an adequate quantity which represents the performance of the KLFitter the *total efficiency* ϵ_{tot} is defined as

$$\epsilon_{tot} = \epsilon_M \cdot \epsilon_R \quad , \tag{6.2}$$

where ϵ_M is the matching efficiency described in Section 5.3 and ϵ_R the efficiency for reconstructing all jets correctly. For the performance studies only the first four jets in p_T are considered regardless of the jet multiplicities. In that case, the matching efficiency is approximately 23 % (see Tab. 5.2) resulting in total efficiencies of roughly 12 % and 15 % for the two constraints, respectively.

6.3. Energy Resolution

In addition to the improvement in the correct association of jets with quarks the performance of the KLFitter is reflected by the impact on the energy resolution of the final state particles. Since the transfer functions of the measured resolutions are a direct input to the fitter, the improvement indicates the performance of the kinematic fit. Because the two light quarks from the hadronically decaying W boson cannot be distinguished by the kinematic fit, no fair association of the fitted energy to the true energy in the MC can be made. Therefore, only the energy resolutions of the b-quarks coming from the hadronically (Fig. 6.4) and leptonically (Fig. 6.5) decaying top quark are shown for both top pole mass constraints. The normalized number of events are plotted depending on $\frac{\Delta E}{\sqrt{E_{\text{true}}}}$ according to the energy resolution in Equation 3.7. The quantity $\Delta E = E_{\text{true}} - E_{\text{meas/reco}}$ is the difference of the true energy and the measured or reconstructed energy, respectively. Since this is a comparison to the true energy values, only matched events are considered.
A Gaussian fit is performed within a range of $\pm 1.5\ \sqrt{\text{GeV}}$ around the mode of the distributions and yields in case of the measured energy resolution of the hadronic b-quark a mean of $0.59 \pm 0.02\ \sqrt{\text{GeV}}$, which means that less energy than the true energy is measured in the detector. Physics wise this loss is mainly caused by leptonic decays in the showering process. Muons might be not identified coming from the b-jet and the energy of neutrinos is lost. The width of the Gaussian fit is $1.17 \pm 0.03\ \sqrt{\text{GeV}}$ and $1.18 \pm 0.03\ \sqrt{\text{GeV}}$ for the free and fixed top pole mass, respectively. The measured energy resolutions marginally differ for both constraints, because in case of the fixed top pole mass less events are rejected due to the fact that MINUIT cannot find a minimum (see Sec. 4.3).
The kinematic fit shifts the energy distribution to a more centered mean value around zero ($-0.06 \pm 0.02\ \sqrt{\text{GeV}}$ and $-0.16 \pm 0.01\ \sqrt{\text{GeV}}$) and makes the shape more symmetric and narrow, although the combinatorial uncertainties cause slightly stronger developed tails. These tails are less pronounced for the true permutation. In case of the free top mass constraint the Gaussian width of the reconstructed energies can be only marginally improved, but in case of the fixed top mass the width is $0.92 \pm 0.02\ \sqrt{\text{GeV}}$ and about 21 % smaller than the measured width.

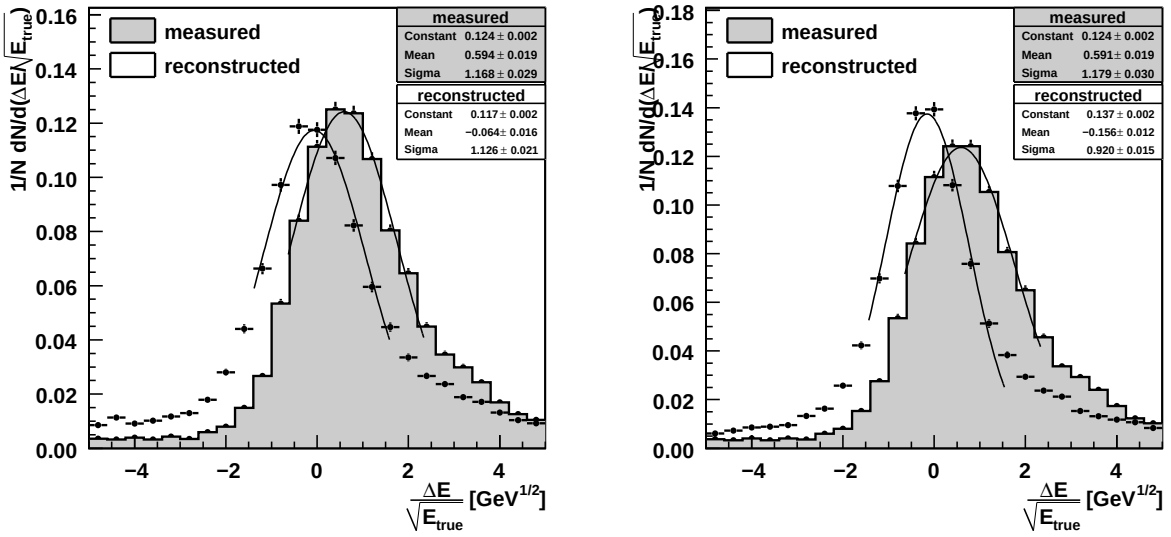

(a) free top pole mass

(b) fixed top pole mass

Figure 6.4.: The measured (gray shaded) energy resolution is compared to the reconstructed energy resolution of the bottom quark, which comes from the hadronically decaying top quark. This study is done for both top pole mass constraints. A simple Gaussian function is used to fit the distributions around the peak. In the statistics boxes the amplitude, the mean and the width of the Gaussian fit are displayed.

The same study is performed for the energy resolution of the b-quark coming from the leptonically decaying top (Fig. 6.5). Again the reconstructed resolutions are centered within uncertainties around zero. Although with the free top pole mass constraint the width can not be improved, the resolution with a fixed top mass is much more narrow after the kinematic fit. The width can be reduced from $1.16 \pm 0.03\ \sqrt{\text{GeV}}$ to $0.71 \pm 0.01\ \sqrt{\text{GeV}}$ by almost 40 %. The measured and the reconstructed energy resolutions are summarized in Table 6.2.

Table 6.2.: The mean and width values of the Gaussian fitted energy resolutions for the two b-quarks coming from the hadronically and leptonically decaying top quark are shown. The values are compared for the two different top pole mass constraints before (measured) and after (reconstructed) the kinematic fit.

	free top pole mass		fixed top pole mass	
	measured	reconstructed	measured	reconstructed
hadronic b-quark				
mean in $\sqrt{\text{GeV}}$	0.59 ± 0.02	-0.06 ± 0.02	0.59 ± 0.02	-0.16 ± 0.01
width in $\sqrt{\text{GeV}}$	1.17 ± 0.03	1.13 ± 0.02	1.18 ± 0.03	0.92 ± 0.02
leptonic b-quark				
mean in $\sqrt{\text{GeV}}$	0.61 ± 0.02	-0.06 ± 0.02	0.60 ± 0.02	-0.04 ± 0.01
width in $\sqrt{\text{GeV}}$	1.16 ± 0.03	1.20 ± 0.03	1.16 ± 0.03	0.71 ± 0.01

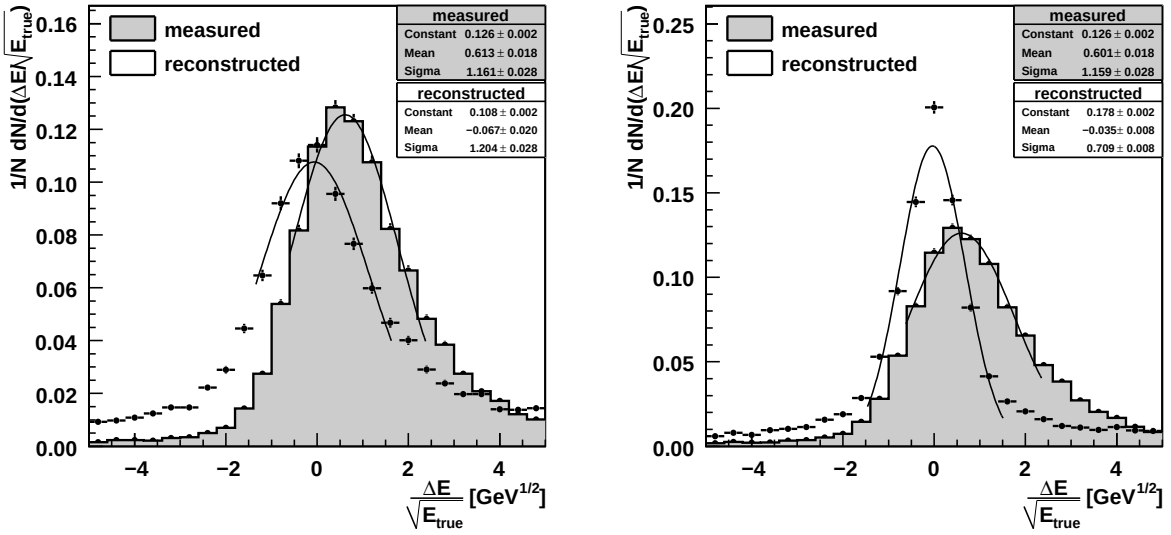

(a) free top pole mass

(b) fixed top pole mass

Figure 6.5.: The measured (gray shaded) energy resolution is compared to the reconstructed energy resolution of the bottom quark, which comes from the leptonically decaying top quark. This study is done for both top pole mass constraints. A simple Gaussian function is used to fit the distributions around the peak. In the statistics boxes the amplitude, the mean and the width of the Gaussian fit are displayed.

These studies show that the kinematic fit can in fact improve the energy resolution of the measured objects by finding better estimators.

6.4. Properties of the Composite Objects

As shown in the last sections the kinematic fit enables a better assignment of jets to parton and returns estimators which are more accurate than the measured values. In the following sections it is analyzed how this affects the kinematics and the properties of composite objects in the $t\bar{t}$ decay chain.

6.4.1. Top Quark

Certainly, the reconstruction of the two top quarks is of particular interest and is subsequently studied more extensively.

Direction

A key variable which represents the performance of the fitter is the direction of the reconstructed top quark. Therefore the distance in η-ϕ space, ΔR, between the reconstructed top quark and the true top quark in the Monte Carlo is studied. No matching is required, but for comparison matched and all events including not matched events are shown. The normalized ΔR distributions of the hadronically and of the leptonically decaying top quark are shown on a logarithmic

scale for both top pole mass constraints (Fig. 6.6 and Fig. 6.7). The range is chosen from -3 to 1 which corresponds to $\Delta R \in [0.001, 10]$.

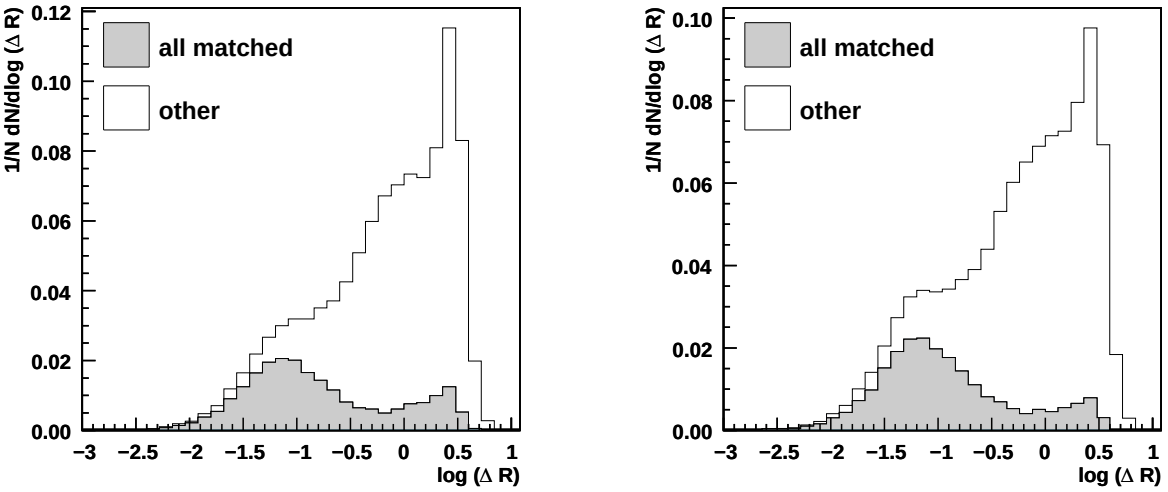

(a) free top pole mass

(b) fixed top pole mass

Figure 6.6.: The ΔR distance of the hadronic top quark to the true one for all matched events gray and not matched events white is shown in a stacked plot. The x-axis is on a logarithmic scale, thus the bin size is not equidistant in ΔR .

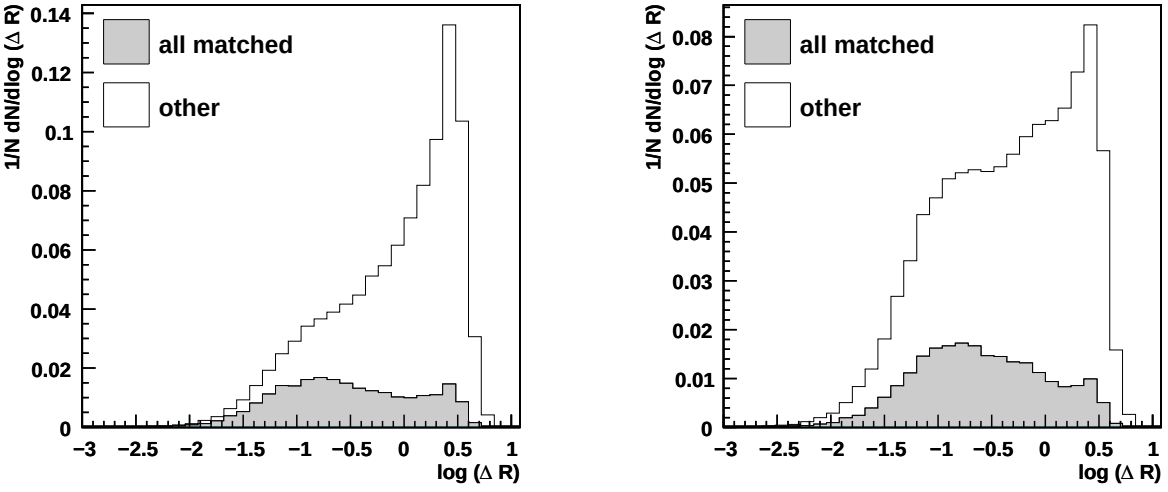

(a) free top pole mass

(b) fixed top pole mass

Figure 6.7.: The ΔR distance of the leptonic top quark to the true one for all matched events gray and not matched events white is shown in a stacked plot. The x-axis is on a logarithmic scale, thus the bin size is not equidistant in ΔR .

If matching is required, in all cases there is a peak visible around -1 which shows that the direction for these cases is quite well reconstructed with a ΔR around 0.1. The distributions are broader for the leptonic top quarks because of additional uncertainties coming from the neutrino momentum. In the case of a free top mass an additional peak arises around 0.5, which means a ΔR around π. In these events jets are wrongly associated to the two hemispheres of the top quarks or uninvolved jets are falsely allocated to the $t\bar{t}$-system. For example the b-quark of the leptonically decaying top quark is assigned to a jet coming from the hadronically decaying top quark. Since this is not intuitively acceptable, further studies on this topic are performed in Section 6.5.1. As expected in the case of a fixed top mass the peak around 0.5 coming from combinatorial background is much more suppressed.
If no matching is required, the combinatorial background dominates the distribution, though for a fixed top mass the shoulder around -1 is more pronounced. The logarithmic scale on the x-axis might give the wrong impression of an unexpected poor reconstruction, but it is chosen here to show the fine structure of the ΔR distribution. In order to summarize the goodness of the reconstruction in terms of direction of the top quarks, the fraction of events with ΔR smaller than a certain value are calculated and summarized in Table 6.3.

Table 6.3.: The fraction of events with reconstructed top quarks within a distance in $\Delta R < 0.1$, 0.3, 0.5 to the true top quarks are summarized for the two constraints. The distances are calculated with and without requirement of truth matching.

	ΔR	Fraction of events in %			
		free top mass		fixed top mass	
		matching	no matching	matching	no matching
hadronic	< 0.1	46.23 ± 0.50	7.37 ± 0.07	53.07 ± 0.54	8.81 ± 0.07
top	< 0.3	69.56 ± 0.62	14.36 ± 0.10	77.29 ± 0.65	16.21 ± 0.10
quark	< 0.5	74.84 ± 0.65	19.19 ± 0.11	82.66 ± 0.68	21.14 ± 0.12
leptonic	< 0.1	24.77 ± 0.37	5.09 ± 0.06	27.14 ± 0.39	9.08 ± 0.08
top	< 0.3	52.73 ± 0.54	12.43 ± 0.09	56.01 ± 0.56	19.60 ± 0.11
quark	< 0.5	63.12 ± 0.59	16.63 ± 0.10	67.75 ± 0.61	24.58 ± 0.12

In the sample of matched events one can see that the directions of the top quarks are adequately reconstructed. If the top mass is left free, approximately 75 % and 63 % of the events have a reconstructed hadronic and leptonic top quark, respectively, within a distance of $\Delta R < 0.5$ to the true top quark. Fixing the top mass even further improves the reconstruction of the direction. The direction of the leptonic top quark can be less precisely reconstructed, because it strongly depends on the reconstruction of the neutrino momentum.
Certainly, the fractions are considerably smaller if no matching is required, because already a part of the used objects coming from the simulation are far off the true final state particles and thus cannot be matched. Final state radiation can change the momentum of the reconstructed objects or uninvolved jets are used for the reconstruction. The reconstruction of the direction of the top quarks is obviously sensitive to these facts. Additionally one should point out that fixing the top quark mass helps the reconstruction of the leptonic top quark direction more than the hadronic top quark direction. The reconstruction of the hadronic top quark direction is probably then dominated by combinatorics, especially permutations within the hadronic hemisphere meaning jets in the decay chain of the hadronic top quark are permuted. With a fixed top mass the leptonic top quark direction is then more precisely reconstructed than the hadronic one and

roughly 25 % of the events have a leptonic top quark with a ΔR distance of smaller 0.5 to the true one.

Mass

As shown in the last sections, fixing the top mass improves the reconstruction significantly, though this restricts the possibility to reconstruct the top quark mass value. cannot be measured in this scenario. Especially in the beginning of the ATLAS experiment the top mass measurement will be an important task, e.g. in order to understand the detector. Thus, in this section the top pole mass is treated again as a free parameter in the kinematic fit.
In the left plot of Figure 6.8 the distribution of the invariant mass m_{jjj} of the three jets associated to the hadronically decaying top is shown stacked with matched (gray) and not matched (white) events. The right plot shows the same but the distribution of the invariant mass $m_{e\nu j}$ of the electron-neutrino-jet system of the leptonically decaying top. The distributions are normalized to unity.

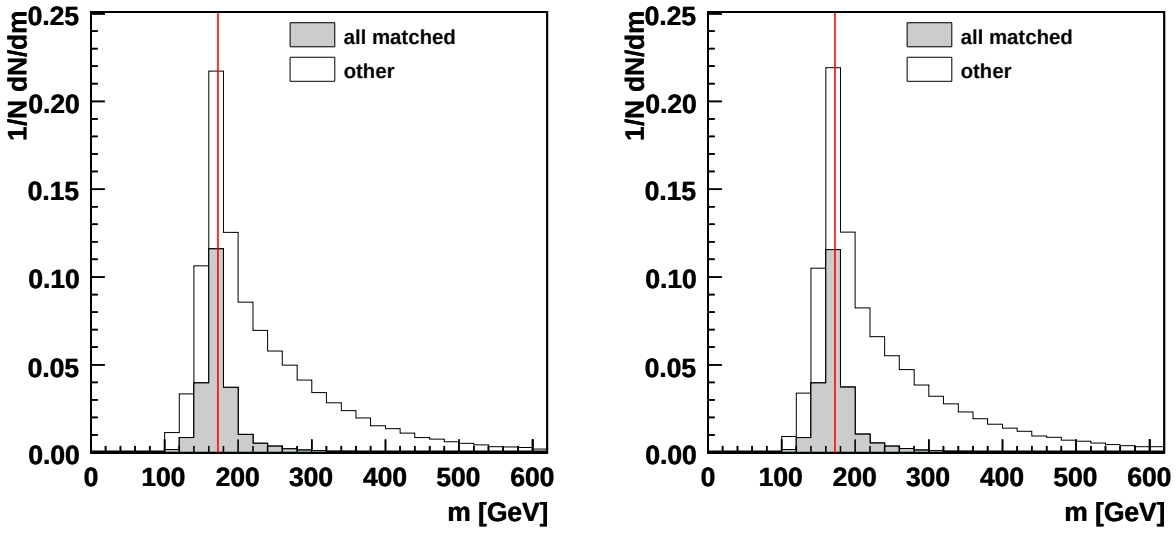

(a) invariant mass m_{jjj}

(b) invariant mass $m_{e\nu j}$

Figure 6.8.: Stack plot of the invariant top masses for all matched events gray and not matched events white. The value at the x-axis of 172.5 GeV is drawn as a vertical red line in the plot and represents the top mass which is used in the MC simulation.

In all cases the peak is well established around 172.5 GeV (indicated by a red vertical line). In the sample of matched events, the combinatorial background which gives rise to a shoulder towards higher top masses, is less pronounced, thus the shoulder of the peak decreases sharply.

Transverse Momentum and Angular Variables

In order to study the reconstruction of the kinematic variables of the top quarks, the normalized distributions of the transverse momentum p_T and the angular variables η and ϕ are compared in Figure 6.9 - 6.11 with the true distributions coming from MC. For these studies no matching is required and the kinematic fit is performed with the free top pole mass constraint. The proper-

ties of the reconstructed hadronic (left) and the leptonic (right) top quark are displayed, the true distributions are shaded in gray. Below the distributions, the ratio of reconstructed and true values are plotted with asymmetric uncertainties in order to visualize the relative discrepancy. The transverse momentum (Fig. 6.9) of both top quarks is reconstructed closely to the truth

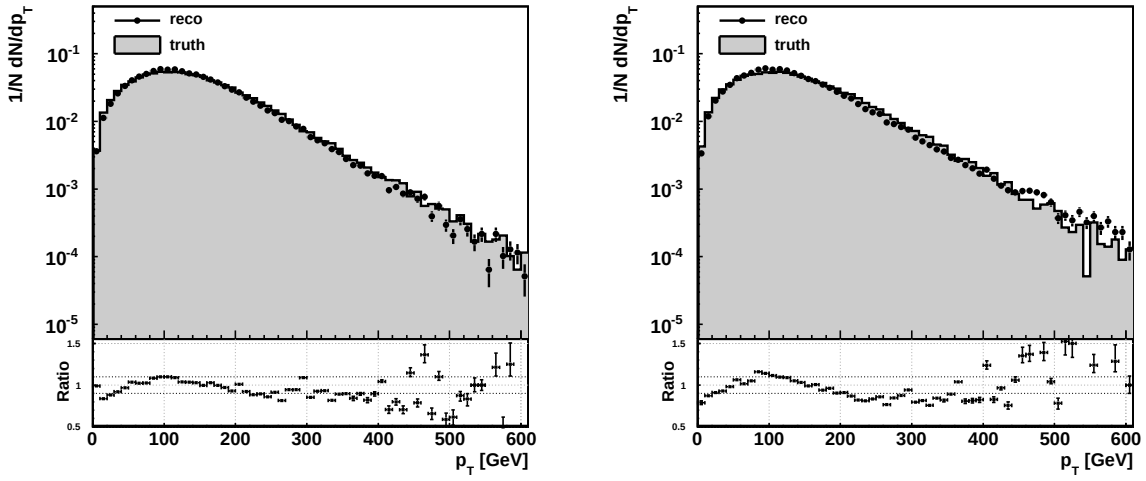

(a) hadronically decaying top quark

(b) leptonically decaying top quark

Figure 6.9.: The reconstructed (dotted) transverse momentum is compared to the true (gray shaded) distribution. The ratio of reconstructed and true value is given in a subdivision of the plot.

values with relative fluctuations of up to ±20 % within the range of $p_T < 400$ GeV. In particular for the leptonically decaying top quark, less events are reconstructed with a transverse momentum in the region 200 GeV $< p_T <$ 400 GeV, whereas too many events have a p_T in the peak region around 100 GeV. For highly boosted top quarks with $p_T > 400$ GeV the distributions differ significantly (see Sec. 6.5.2), though in the region $p_T > 600$ GeV the distribution is dominated by the large statistical uncertainties.
The η-distribution (Fig. 6.10) of the reconstructed hadronic top quark is in relatively good agreement with the true distribution, in the central region ($-2 < \eta < 2$) the relative deviations to the true distributions are smaller than ±15 %. Too few events are reconstructed with η values around zero, whereas on average more events are reconstructed with high η values. In the forward region ($\eta > |3|$) the relative discrepancy to the truth rises up to ±50 %.
The η of the reconstructed leptonic top quark is reasonably well reconstructed with relative fluctuations of ±20 % in the central region ($-2 < \eta < 2$), but significantly more events than in MC truth information are reconstructed in the forward region ($|\eta| > 2$). This tendency was already observed for the hadronically decaying top quark but was much less pronounced. This substantial worse reconstruction, compared to the hadronic top quark, can be explained by additional uncertainties through the free parameter p_z of the neutrino momentum.
The ϕ-distributions (Fig. 6.11) of both top quarks are shown for the sake of completeness and match well with relative deviations smaller than ±10 % to the true distributions.

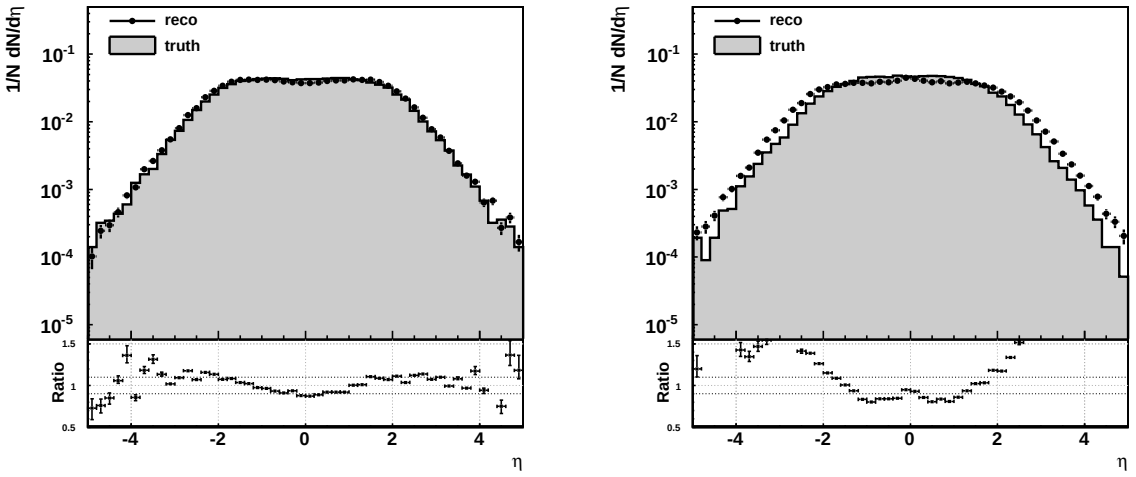

(a) hadronically decaying top quark

(b) leptonically decaying top quark

Figure 6.10.: The reconstructed (dotted) pseudorapidity is compared to the true (gray shaded) distribution. The ratio of reconstructed and true value is given in a subdivision of the plot.

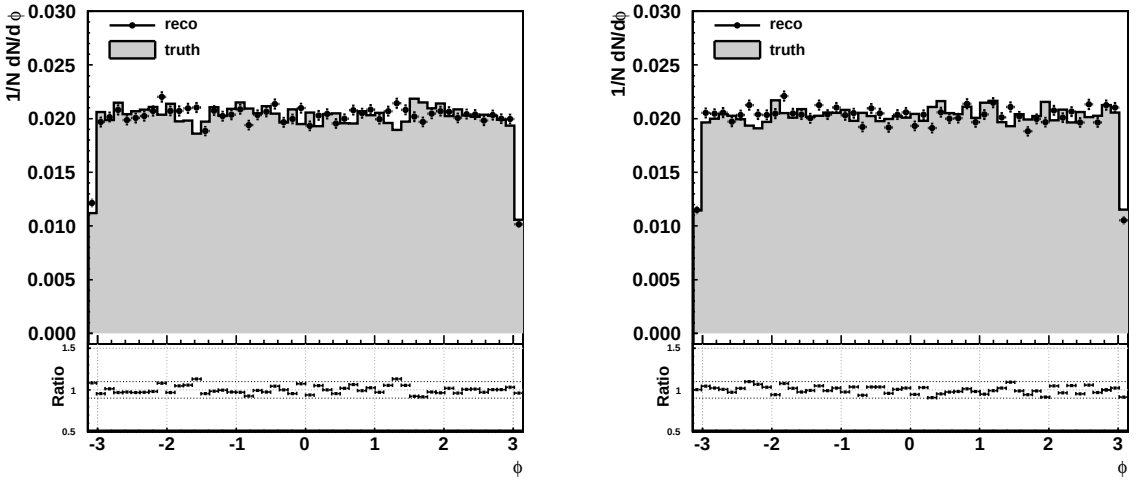

(a) hadronically decaying top quark

(b) leptonically decaying top quark

Figure 6.11.: The reconstructed (dotted) ϕ coordinate is compared to the true (gray shaded) distribution. The ratio of reconstructed and true value is given in a subdivision of the plot.

6.4.2. $t\bar{t}$-System

In order to complete the performance studies of the KLFitter the reconstruction of the transverse momentum and of the invariant mass of the $t\bar{t}$-system are shown in Figure 6.12. Since the distributions are quite similar for both constraints, they are only shown for the free top pole mass and are compared to MC truth (gray shaded).

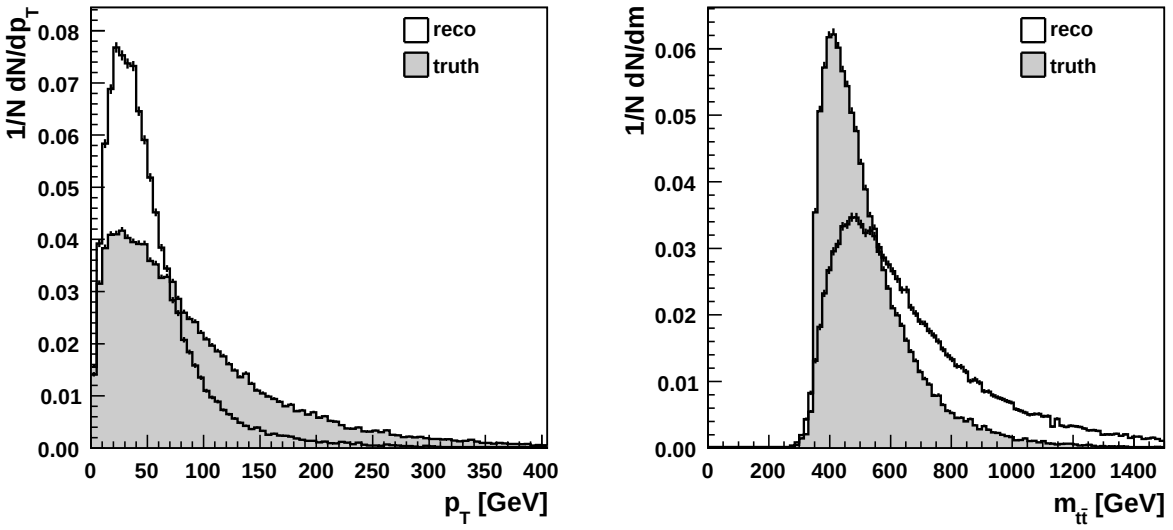

(a) transverse momentum

(b) invariant mass

Figure 6.12.: The transverse momentum and the invariant mass of the $t\bar{t}$-system are compared to truth (gray shaded).

Both, the reconstructed transverse momentum and the invariant mass of the $t\bar{t}$-system do not agree with the truth. However, the transverse momentum is in principle not easy to reconstruct and only the use of the $\not{E}_T$ in the kinematic fit makes it possible to reconstruct it at all. The mean value of the reconstructed transverse momentum is much smaller than the true one. Also the distribution is much more narrow than in truth. Since the p_T of the $t\bar{t}$-system is underestimated, the invariant mass is overestimated, because of the relativistic relation $m^2 = E^2 - p^2$. The resulting reconstructed mass distribution is much broader than the true one. However, matched events show in the true permutation comparable distributions to the ones of MC truth. This indicates that the insufficient reconstruction is mainly caused by combinatorics and selected objects, which do not match to the truth $t\bar{t}$ topology. Hence, an emphasis is placed on further studying the reconstruction of the $t\bar{t}$-system in Section 6.6.

6.5. Kinematic Limitations of the Reconstruction

Because of the changing decay geometry, it is expected that the performance of the $t\bar{t}$ reconstruction depends on the initial energy of the decaying objects. Some aspects are studied in more detail in the following. The kinematic fit is performed for the four jets with the highest p_T and with the top pole mass treated as a free parameter.

6.5.1. Reconstructing the Two Hemispheres of the Decaying Top Quarks

Direction of the Top Quarks

In order to better understand the shapes of the ΔR distributions of the top quarks, shown in Section 6.4.1, the reconstruction of matched events is further studied in the following. As presented in Section 5.3 roughly 23 % of the events can be matched. In Figure 6.13 the ΔR distributions of the hadronically and the leptonically decaying top quark are shown in a stacked plot.

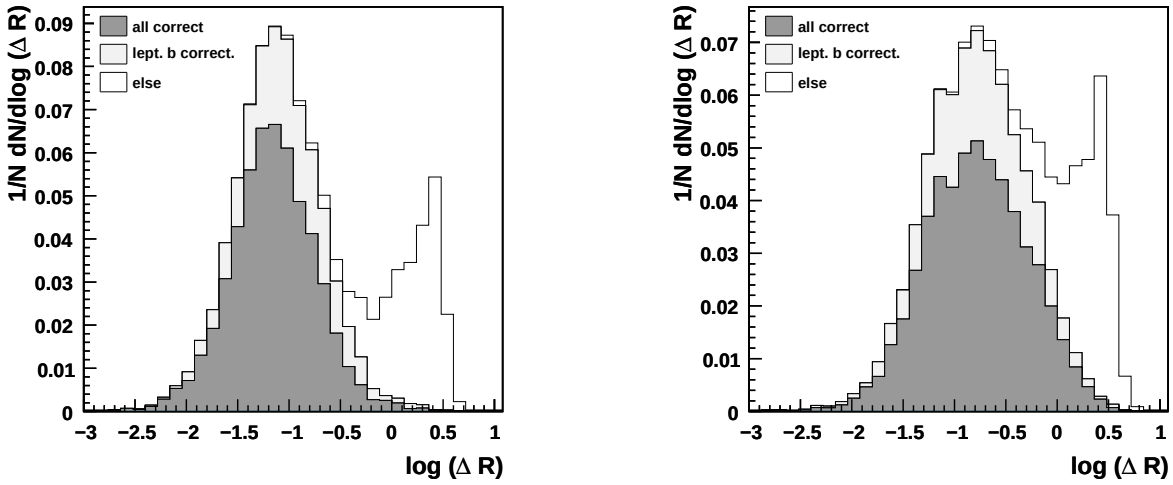

(a) hadronically decaying top quark

(b) leptonically decaying top quark

Figure 6.13.: The ΔR distance of the reconstructed top quarks to the true ones for matched events are shown in a stacked plot. It is distinguished between events in which all jets (dark gray) are correctly assigned, the leptonic b-jet is (light gray) and is not (white) correctly assigned. The x-axis is on a logarithmic scale, thus the bin size is not equidistant in ΔR .

In dark gray the ΔR between the reconstructed and the true top quark is shown for those events, in which all jets are correctly assigned to the partons. In light gray the additional events are shown, in which at least the b-jet of the leptonically decaying top quark is correctly assigned, which means that the three jets coming from the hadronically decaying top quark are correctly associated with the hadronic top quark but are permuted among each other. All jets are correctly assigned to their corresponding top quark hemisphere. For matched events it is obvious that if the hadronic hemisphere is correctly reconstructed this is also true for the leptonic hemisphere, but not necessarily the other way around, because a light jet in the hadronic hemisphere can be associated with the b-quark. Finally, the events in which jets are wrongly associated to their corresponding hemispheres are shown in white.
Completely correctly reconstructed events generate a peak around -1 which means that the reconstructed top quark direction is very close to the true one. Also events in which the jets are correctly associated with their hemispheres, but are permuted within the hemisphere, contribute only to the peak around -1. Only if jets are interchanged between the hemispheres, the direction of the reconstructed top quark differs significantly from that of the true quark, so these events generate the second peak at around $\Delta R = 0.5$. All this is true for the direction of the hadronically decaying top quark as well as for the leptonically decaying one, though the peak is slightly shifted to higher values and broader in case of the leptonic top quark. This is due to

the additional uncertainties coming from the neutrino reconstruction.
The same studies can be performed for partly matched events. First all events are studied, in which all partons of the hadronic hemisphere could be unambiguously matched, but the b-quark coming from the leptonically decaying top quark is not necessarily matched. These events are called *hadronic-matched* events. The matching efficiency of matching only the hadronic hemisphere is roughly 30 % (see Fig. 6.18) and is therefore slightly higher than the matching efficiency of matching all jets to their corresponding partons. If the matched jets are correctly associated with the hadronic hemisphere, one can still associate the remaining jet with the leptonic b-quark, although this jet could not be matched to the true parton. Note that this is only possible for the given scenario in which exactly four jets are considered in the fit and that there is a chance that the true jet coming from the leptonically decaying top is not selected. Figure 6.14 shows the ΔR distribution of the hadronically and leptonically decaying top quark for hadronic-matched events in a stacked plot. Again it is distinguished between the different reconstruction scenarios.

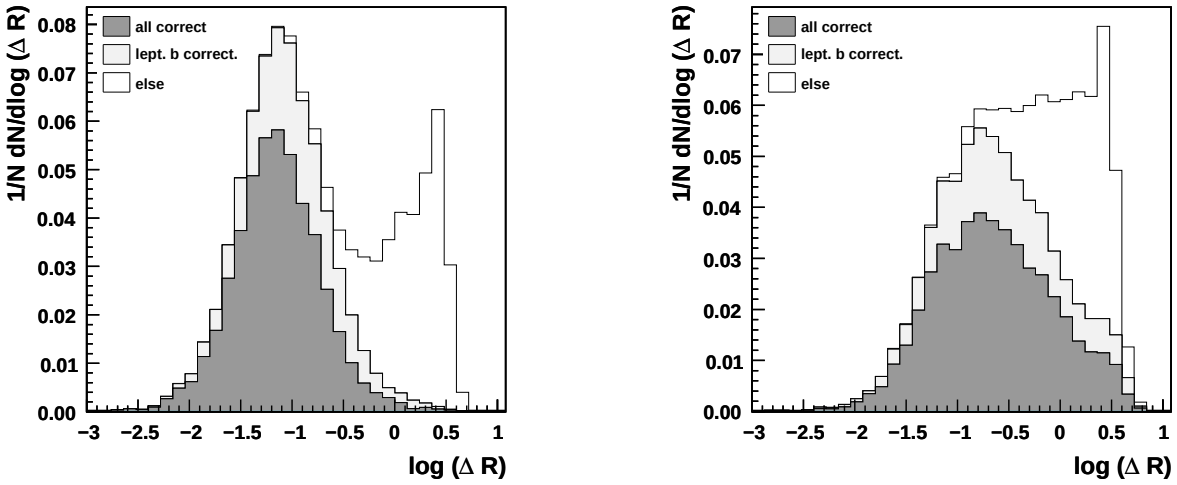

(a) hadronically decaying top quark

(b) leptonically decaying top quark

Figure 6.14.: The ΔR distance of the reconstructed top quarks to the true ones for hadronic matched events are shown in a stacked plot. It is distinguished between events in which all jets (dark gray) are correctly assigned, the leptonic b-jet is (light gray) and is not (white) correctly assigned. The x-axis is on a logarithmic scale, thus the bin size is not equidistant in ΔR .

In case of the hadronically decaying top quark (left) the additional events, in which the leptonic b-quark is not matched, contribute to the main peak around -1 if their jets are correctly associated with the hemispheres, else they accumulate in the second peak at around 0.5. Similarly the ΔR distribution of the leptonically decaying top quark (right) changes. However, events in which the jet associated with the leptonic b-quark is not matched to the parton accumulate in the right tails of the distributions, in which the hemispheres are correctly separated. These are for instance events in which the jet coming from the leptonically decaying top is not selected or is deflected by final state radiation. This and the rise of events with interchanged jets between the two hemisphere leads to the fact that the second peak around 0.5 is already higher than the peak of well reconstructed events around -1.

Finally, the ΔR distributions of the hadronically and leptonically decaying quark for all events in which at least the b-quark of the leptonic top quark could be uniquely matched to a jet are shown in the stacked plots of Figure 6.15. These events are called *leptonic-matched* events. The matching efficiency to match only the leptonic b-jet to a parton is larger than 80 % (see Fig. 6.18), so almost all events are used for this study. Obviously, now only the distinction whether the jets are correctly associated to their hemisphere (dark gray), meaning the leptonic b-quark is correctly reconstructed, or not (white) is possible.

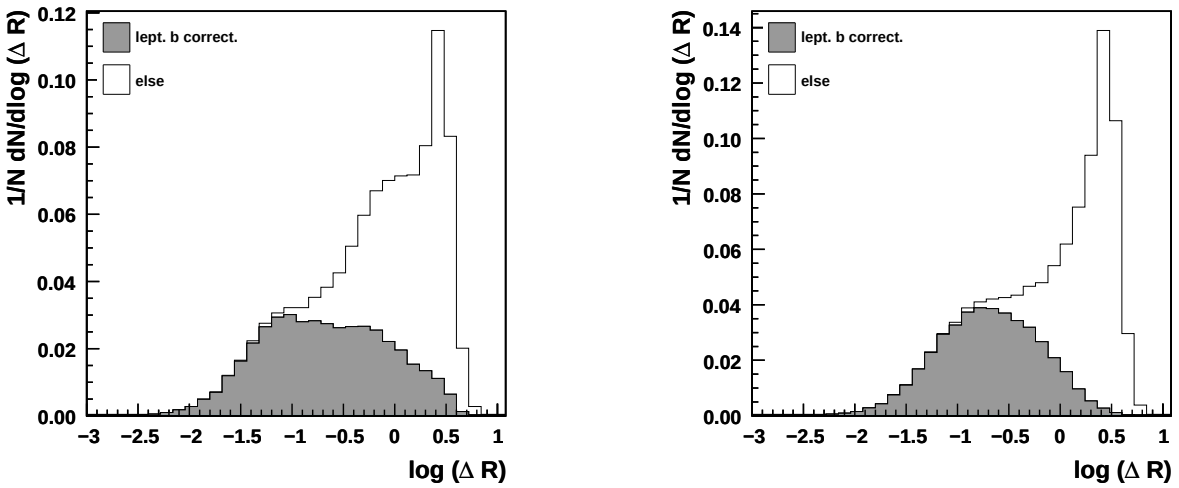

(a) hadronically decaying top quark

(b) leptonically decaying top quark

Figure 6.15.: The ΔR distance of the reconstructed top quarks to the true ones for leptonic matched events are shown in a stacked plot. It is distinguished between events in which the leptonic b-jet is (dark gray) and is not (white) correctly assigned. The x-axis is on a logarithmic scale, thus the bin size is not equidistant in ΔR .

Although for these studies significantly more events than in Figure 6.13 are used, the shape of the ΔR distribution of the events with jets correctly associated to the hemispheres look quite similar in case of the leptonically decaying top quark. Only the events in which jets of the two hemispheres are interchanged generate the peak around 0.5. Since this happens quite often the peak is three times as high as the peak of well reconstructed events.
In the same way the distribution of the hadronically decaying top quark is generated but with an additional contribution of events in which unsuitable jets are used for the reconstruction of the hadronically decaying top quark. These events enhance like in the right plot of Figure 6.14 the right tail of the distribution, in which the leptonic b-jet is correctly assigned. In addition they contribute to the left tail of the peak around 0.5, in which jets are interchanged between the hemispheres. The explanation is that jets which belong to the hadronically decaying top quark are not selected or might have been deflected by FSR. But since three jets are used for the reconstruction of the hadronic hemisphere this is more likely to happen than in the leptonic hemisphere.
In conclusion, the peak around 0.5 is mainly generated by events in which jets are wrongly associated to their corresponding top quark. The contribution to this by uninvolved or deflected jets is rather small. As expected permuting jets within the hadronic hemisphere does not affect the direction of the top quarks significantly.

6.5.2. Boosted Top Quarks

Direction of the Top Quarks

One would expect, that the direction of the top quarks is better reconstructed if the top quarks are not boosted to the forward direction, but do have a reasonable transverse momentum. In this scenario, the jets coming from the different top quarks are expected to be well separated among the two hemispheres. In Figure 6.16 the average of the ΔR distribution is plotted versus the true pseudorapidity η and the true transverse momentum p_T for the hadronically (gray) and the leptonically (black) decaying top quark. No matching is required.

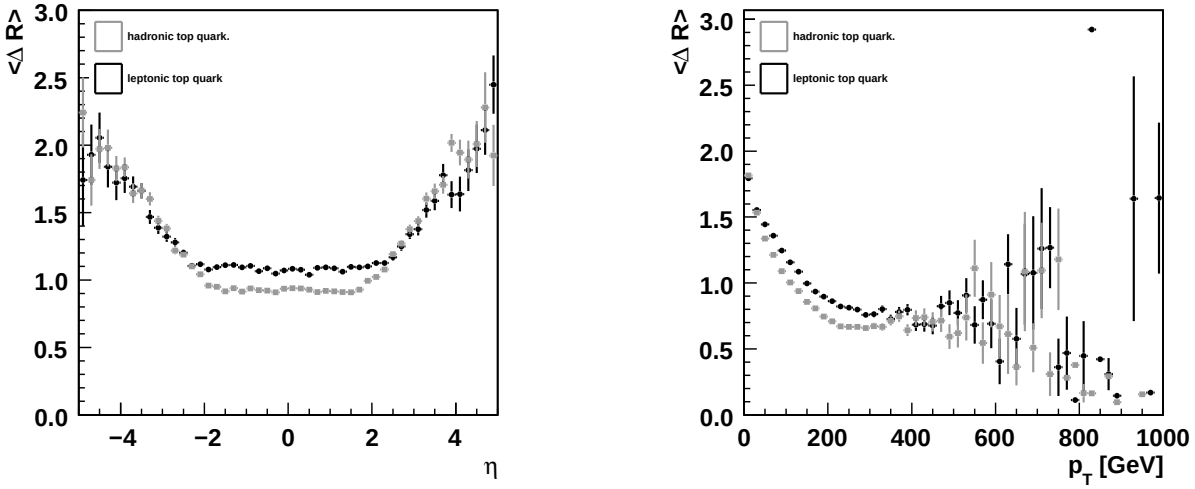

(a) averaged ΔR versus η of top quarks

(b) averaged ΔR versus pt of top quarks

Figure 6.16.: The average of the ΔR distance of the top quarks to the true ones for hadronic (gray) and leptonic (black) top quark versus their η direction and transverse momentum.

Indeed, in the central region of $-2 < \eta < 2$ the average ΔR is almost constant around a value of 1 (non logarithmic). As expected, the ΔR of the leptonically decaying top quark is slightly larger than the one for the hadronically decaying top quark. But in the forward region ($|\eta| > 2$) the average ΔR of both top quarks increases strikingly.
A similar trend is observable for the p_T of two top quarks. At low p_T values the average ΔR is larger than 1.5, but decreases constantly until a transverse momentum of roughly 200 GeV is reached. For 200 GeV $< p_T <$ 500 GeV the average ΔR is almost constant at values below 0.7 and 0.8 for the hadronic and leptonic top quark, respectively. The interchange of the leptonic b-jet with jets coming from the hadronically decaying top quark seems only to happen negligibly for $-2 < \eta < 2$ and $p_T >$200 GeV. Thus for instance, cutting on these values would be a possibility to further improve the reconstruction of the $t\bar{t}$ decay.

Reconstruction Efficiencies

As shown in Section 6.5.1,the direction of the top quarks is adequately reconstructed as long as no jets are assigned to the wrong hemisphere. Thus the reconstruction efficiency and the ΔR distribution of the top quarks are strongly anti-correlated and the opposite trend as for the average ΔR should be observable for the reconstruction efficiency. In Figure 6.17 the recon-

struction efficiency is plotted versus the transverse momentum of the hadronic (light gray) and leptonic (black) top quarks. For comparison, shaded in dark gray, the efficiency for a random assignment of jets is shown.

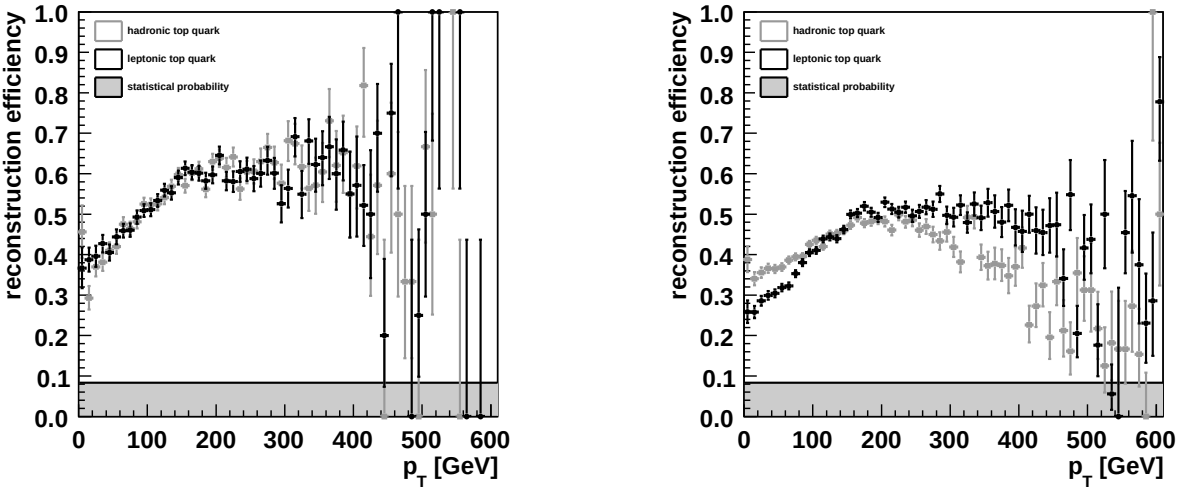

(a) fully matched events

(b) only leptonic b-quark is matched

Figure 6.17.: The reconstruction efficiency is shown versus the transverse momentum of the hadronic (gray) and leptonic (black) top quark.

In the left plot only fully matched events are used in order to evaluate the reconstruction efficiency of the entire event. Since the two top quarks are often approximately balanced in transverse momentum no severe differences are visible between the two distributions of the top quarks. At low p_T values the reconstruction efficiency is below 40 % and rises remarkably to values larger than 60 % at a transverse momentum of roughly 150 GeV. At this point the efficiency stays constant within fluctuations. For large transverse momenta of the top quarks the two hemispheres are well separated and thus the reconstruction efficiency increases. In contrary to Figure 6.16 only matched events can be used for this study.
On the other hand for the reconstruction of the top quark properties the key factor is the correct assignments of the jets to their top quark hemisphere. Hence, the same study can be made for events with the requirement that only the leptonic b-quark is matched to a jet. If then the matched jet is correctly assigned to the leptonic b-quark one can call the jets correctly associated to their hemispheres, though of course uninvolved jets can modify the interpretation. In the right plot (Fig. 6.17) the efficiency to correctly reconstruct the leptonic b-jet is plotted for all leptonic-matched events versus the transverse momentum of the two top quarks. Because only the leptonic b-quark is required to be matched more than 80 % events can be used for this study. For the leptonic top quark the shape of the distribution looks similar to the plot, in which only matched events are used, though the efficiency is shifted by roughly 10 % to lower values. However, the efficiency seems to be less dependent on the p_T of the hadronic top quark for low values, but starts to fall again for p_T values larger than 250 GeV. Because of the transverse momentum of the $t\bar{t}$-system, the transverse momentum of the two top quarks can differ. So for a high transverse momentum of the hadronic top quark it is less likely to associate the jets

correctly to their top quark hemisphere. One explanation for this can be found in the next section.

Matching Efficiencies

In order to understand the right plot of Figure 6.17, the matching efficiency is shown versus the p_T of the hadronic top quark in Figure 6.18.

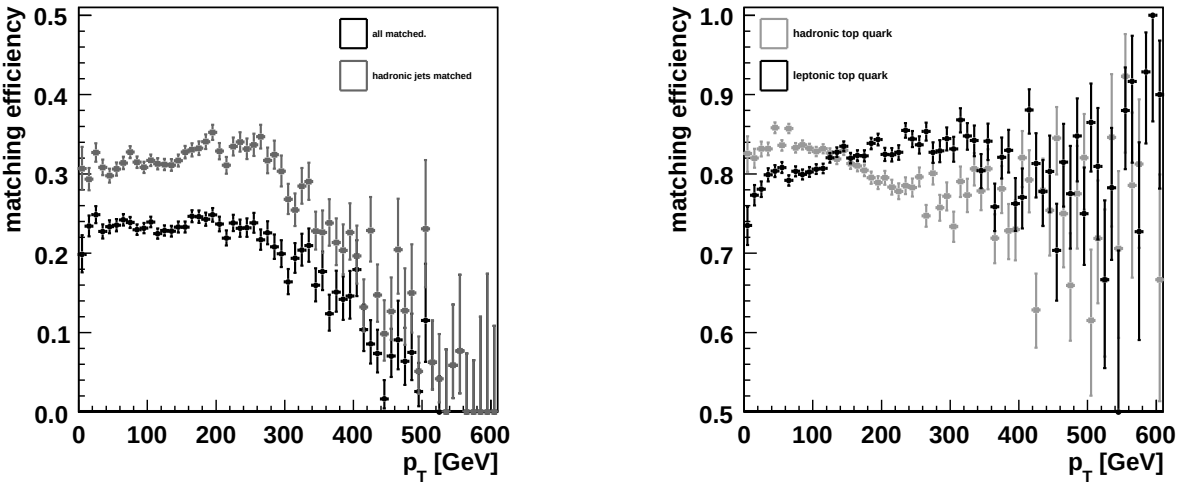

(a) matching efficiencies versus p_T of hadronic top quark

(b) leptonic matching efficiency versus p_T of the two top quarks

Figure 6.18.: On the left the matching efficiencies for matching all partons (black) or only the partons of the hadronically decaying top quark (gray) are shown versus the transverse momentum of the hadronic top quark. On the right the matching efficiency for matching the b-quark of the leptonically decaying top quark is shown versus the transverse momentum of the hadronic (gray) and leptonic (black) top quark.

In the left plot the matching efficiency that all partons are matched (black) and that only the quarks coming from the hadronically decaying top quark are matched (gray) are shown. Both matching efficiencies are nearly constant in the range of 0 GeV $< p_T <$ 250 GeV but then start to drop. One explanation for this is, that if the hadronically top quark is highly boosted, so are the b-quark, the W boson and the light quarks from the W decay. The light quarks point almost in the same direction and will generate jets, which can overlap. In the reconstruction of the detector signature this might be identified as one single jet only. Moreover, the jet of the boosted b-quark can overlap with jets of the light quarks and might be merged together (*fat jets*) in the reconstruction of the jets.
This explains the drop of the reconstruction efficiency in the right plot of Figure 6.17. If the hadronic top quark is too highly boosted, two jets of the top quark decay are merged to one and an uninvolved jet is used for the reconstruction. If uninvolved jets are used for the reconstruction it is more likely to assign this jet to the leptonic b-quark and the jets are not correctly assigned to their top quark hemisphere, even if the leptonic b-quark could be matched. Note that this does not directly affect the reconstruction efficiency of the hadronic top quark hemisphere, because these events cannot be used to evaluate this measure. But the reconstruction of the

object properties in the hadronic top quark hemisphere is obviously affected. This is of course a problem of the jet algorithm and there are other jet algorithms that are more capable of separating these overlapping jets [72], or other techniques, which aim to identify highly boosted top quarks ($p_T > 500$ GeV) and reconstruct the substructure of broad mono-jets, which are caused by hadronically decaying top quarks [73].
In the right plot of Figure 6.18, the matching efficiency for matching the leptonic b-quark to a jet is shown versus the transverse momentum of the hadronic (gray) and leptonic (black) top quarks. As expected the matching efficiency slightly rises with the p_T of the leptonic top quark, because the matching becomes easier for clearly separated hemispheres and a well identifiable high energetic jet. However, the matching efficiency drops with rising p_T of the hadronic top quark, which supports the assumption that hadronic jets are merged and uninvolved jets are used for the reconstruction, which might be matched to the leptonic b-quark.

6.6. Reconstruction with Different Jet Multiplicities

As seen in Figure 5.1 in only about 50 % of the selected events the jet multiplicity is exactly four. Taking only the four highest jets in p_T regardless of the jet multiplicity covers the risk that not all of these four jets have their origin in final state particles from the $t\bar{t}$ decay but are high-p_T jets coming from QCD processes like ISR and FSR. The following studies are focused on the $t\bar{t}$ reconstruction with different jet multiplicities.
The idea is to divide the data set into samples with different numbers of measured jets N and select (in order of p_T) more than four jets for the kinematic fit. However, only four jets can be used in the $t\bar{t}$ reconstruction, so every permutation of four jets out of n selected jets is fitted. This is illustrated for six measured jets as an example in the schematic of Figure 6.19.

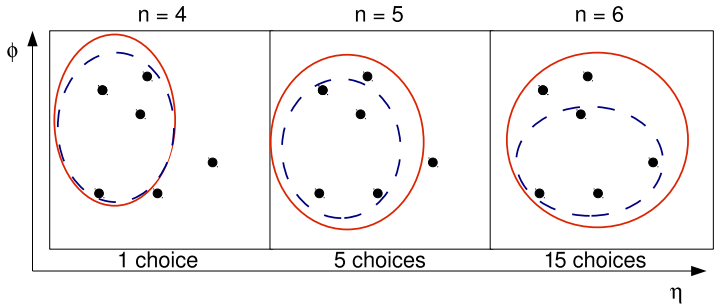

Figure 6.19.: The black dots illustrate N = 6 measured jets in η-ϕ-space. The red circle (solid line) indicates how many jets are considered for the fitting procedure and the blue circle (dashed line) indicates that only four jets can be used to reconstruct the $t\bar{t}$-system.

If again as an example six jets are measured there are three possibilities: Either the first four, five or six jets in p_T are considered in the fit. If for example all six jets are considered, every permutation of four out of the six jets has to be fitted. This results in a much larger number of jet permutations and the CPU time for fitting a single event increases. Jets which are not associated to the $t\bar{t}$ decay in a specific fit can permute in any order and are thus invariant under permutation. These permutations are removed in the fitting procedure. The number of possible permutation is given by

$$\mathrm{N(permutation)} = \frac{\mathrm{n!}}{2 \cdot (\mathrm{n}-4)!} \quad , \tag{6.3}$$

where n is the number of considered jets, the factor 2 takes into account that the two light quarks are indistinguishable and the factor $(n-4)!$ removes all invariant permutation of jets which are not used in the current fit of the $t\bar{t}$-system. Since more than 90 % of the events have four to six jets in the event (see Sec. 5.2), the studies are performed for these measured numbers of jets. In the kinematic fit, the top pole mass is used as a free parameter.

6.6.1. Reconstruction Efficiencies

The reconstruction of the $t\bar{t}$-system becomes much harder if more jets are taken into account, so naturally the reconstruction efficiency drops (compare Sec. 6.2). The pure statistical probability to find the correct permutation by chance is the inverse of the number of permutations (Eq. 6.3). For four jets this is $\frac{1}{12} \approx 8\,\%$, for five jets $\frac{1}{60} \approx 2\,\%$ and for six jets only $\frac{1}{180} < 1\,\%$. Subsequently, one needs to compare the reconstruction efficiencies obtained with the KLFitter to the statistical probabilities of finding the correct permutation by random assignment (Fig. 6.20).

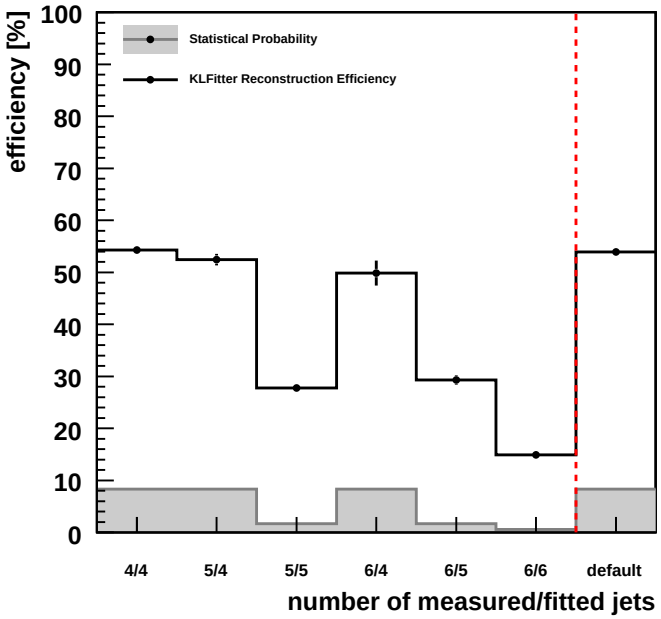

Figure 6.20.: The reconstruction efficiencies that all jets are correctly assigned by the KLFitter (black dots) are compared to the statistical probabilities (gray shaded) to find the correct permutation by chance. The first number in the x-axis label gives the number of measured jets, while the second gives the number of jets, which are used in the fit. In the last bin the reconstruction efficiency from Section 6.2 is shown, where always four jets are used for the fit, regardless of the jet multiplicity.

For a given number of measured jets, the reconstruction efficiency drops the more jets are considered in the fit. Compared to the statistical probability the reconstruction efficiency is still large. For comparison the reconstruction efficiency for fitting always only the first four jets in p_T regardless of the number of measured jets is shown in the last bin.
As mentioned in Section 5.3 the reconstruction efficiency alone is not a meaningful quantity, because the matching efficiency increases, the more jets are considered for the ΔR matching

procedure. Thus, more events are used in order to evaluate the reconstruction efficiency. The total efficiency defined in Equation 6.2 is affected by these two competing effects and is hence used to compare the performance of the KLFitter for the different scenarios. The results are shown in Table 6.4.

Table 6.4.: For a given number of jets the matching, reconstruction and total efficiencies are calculated for the possible number of considered jets. In the last two rows two possible setups of the KLFitter are shown. In the first row always the four highest jets in p_T are used for the fit, in the second row five jets are used for jet multiplicities higher than four.

Number of jets in event	Number of jets considered in the fit	ϵ_{M} in %	ϵ_{R} in %	ϵ_{tot} in %
4	4	36.62 ± 0.32	54.31 ± 0.63	19.89 ± 0.29
5	4	14.99 ± 0.22	52.46 ± 1.11	7.86 ± 0.20
	5	49.16 ± 0.42	27.81 ± 0.45	13.67 ± 0.25
6	4	7.14 ± 0.24	49.88 ± 2.38	3.56 ± 0.21
	5	28.15 ± 0.48	29.34 ± 0.92	8.26 ± 0.29
	6	53.94 ± 0.66	14.94 ± 0.47	8.06 ± 0.27
4/5/6	4	24.02 ± 0.18	53.91 ± 0.54	12.95 ± 0.16
4/5/6	4/5/5	39.86 ± 0.23	39.55 ± 0.36	15.76 ± 0.17

Although the reconstruction efficiency drops significantly, for example from approximately 54 % to only roughly 15 % for six measured jets, the total efficiency can be increased due to the rise of the matching efficiency. For five as well as for six measured jets, approximately twice as many events can be correctly reconstructed, if five jets are used in the fitter instead of only four. Permuting six jets in case of six jets in the event leads to no further improvement in the total efficiency within the statistical uncertainties. Although the matching efficiency is larger than 50 %, the reconstruction efficiency decreases too strongly to gain in total efficiency.
Accordingly, a new setup for the KLFitter can be defined depending on the jet multiplicity: The four highest jets in p_T are only used if exactly four jets pass the selection, else the five highest jets in p_T are considered in the reconstruction of the $t\bar{t}$-system. This new configuration leads to a relative improvement in total efficiency of 23 %, which is shown in the last two rows of table 6.4.

6.6.2. Performance of the KLFitter for Six Measured Jets

In the last section it was shown that the total efficiency can be increased, if more than exactly four jets are selected for the $t\bar{t}$ reconstruction. In the following it is studied whether the reconstruction of the kinematics and properties of the composite objects can also be improved. For these studies a jet multiplicity of six is chosen as an example, five jet events behave comparably (see Sec. 6.7.3). No matching is required, since else different events and different number of events are compared. Still the top pole mass is treated as a free parameter. In the kinematic fit of the events always the four, five and six highest jets in p_T are selected and permuted separately. In each plot these three cases are shown in black, red and blue, respectively. If a comparison to MC truth is made, this is plotted shaded in gray.

Likelihood Distribution

Apart from the quantitative investigation of how often one can find the correct permutation of the jets with the best permutation (see Sec. 6.6.1), it is interesting to know the quality of the best permutation or in other words the quality of the kinematic fit. This is reflected in the likelihood distributions of the best permutation, which are shown in Figure 6.21 together with the permutation probabilities.

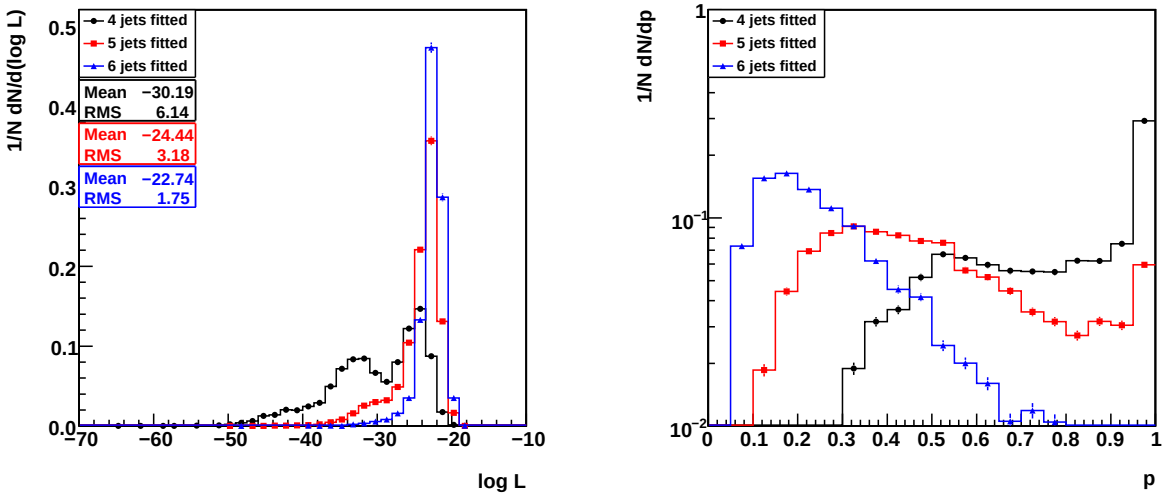

(a) likelihood distributions

(b) permutation probabilities

Figure 6.21.: The likelihood distributions and the permutation probability of the best permutations in six jets events are shown for the 3 different configurations of the KLFitter on a logarithmic scale. Either four jets (black), five jets (red) or six jets (blue) are selected for the fit and are permuted.

The peak of the logarithmic likelihood distributions is the sharper, the more jets are used in the fit. The RMS can be reduced from 6.14 to only 1.75, if six jets are taken into account. Also the peak position is slightly shifted to higher likelihood values. Since more jets are available for the single fit, a better configuration of the jets can be found resulting in a better likelihood value. The second peak at around $\ln \mathcal{L}$ of -35, visible for four jets and also shown in Section 6.1, disappears for higher numbers of jets used in the fit. So one may conclude that this peak arises because jets which come from the $t\bar{t}$ decay are within the acceptance of the detector but not selected. Thus uninvolved jets are used for the reconstruction and lead to worse likelihood values.
Aside from the fact, that it is much harder to find the correct permutation for more jets used in the fit, the likelihood distributions look similar for the first best permutations. This is reflected in the distributions of the permutation probability for the best permutation. Using more jets in the fit results in permutation probability distributions, which are shifted significantly to lower values. If five jets are considered a broad shoulder arises at values around 0.5 and less than 10 % of the events have a permutation probability of larger than 0.95. If six jets are considered the permutation probability ranges from 0.05 only up to 0.80 with a broad peak around 0.2, so only in few events the probability is larger than 0.5. The criterion to select the best permutation simply by the best likelihood value becomes slightly inaccurate, because the values are nearby.

Nevertheless only the best permutation has probabilities larger than 0.5 and in consideration of the significantly increasing number of permutations, the probability densities still look reasonable and can be clearly separated from those of worse permutations.

W Boson

Mass The W boson mass is in general strongly constrained by the Breit-Wigner W boson mass constraint. With a width of 2.141 ± 0.041 GeV [4] there is not much freedom for the mass to vary. As expected (see Figure 6.22) most of the reconstructed hadronically (left) and leptonically (right) decaying W bosons have a mass within the bin around the true value.

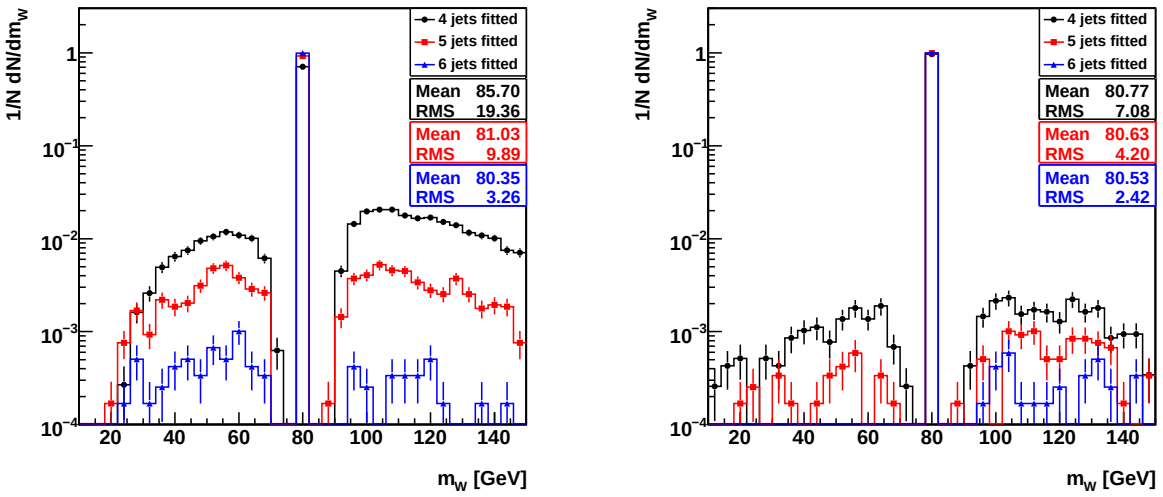

(a) hadronically decaying W boson

(b) leptonically decaying W boson

Figure 6.22.: The invariant mass distributions of the hadronically and leptonically decaying W boson systems with six jets in the event are shown. Either four jets (black), five jets (red) or six jets (blue) are selected for the fit and are permuted.

However, in a logarithmic scale side tails appear in the order of 10^{-2} to 10^{-3} fraction of total events, which are much more pronounced if exactly four jets are considered in the fit. These shoulders are caused by combinatorial background, in particular by using jets for the reconstruction of the $t\bar{t}$-system, which are probably not originating from the top quark decay. Thus the side tails are more developed for the hadronically decaying W boson and can be reduced up to a factor of 10 if six jets are taken into account for the fit. If six jets are used in the fit, the tails are negligibly small but also for five jets the tails are fairly suppressed, so that almost all events have masses in the bin of 80 GeV.

Top Quark

Direction Again, the direction of the top quarks is examined by calculating the ΔR between the true and reconstructed top quark. The distributions are shown in Figure 6.23. The peak around 0.5 coming from combinatorics is less pronounced, the more jets are used in the fitting procedure. As a consequence, a shoulder arises around values of -1 if more jets are considered. In Section 6.5.1 it has been pointed out that this peak is generated by events in which the jets are

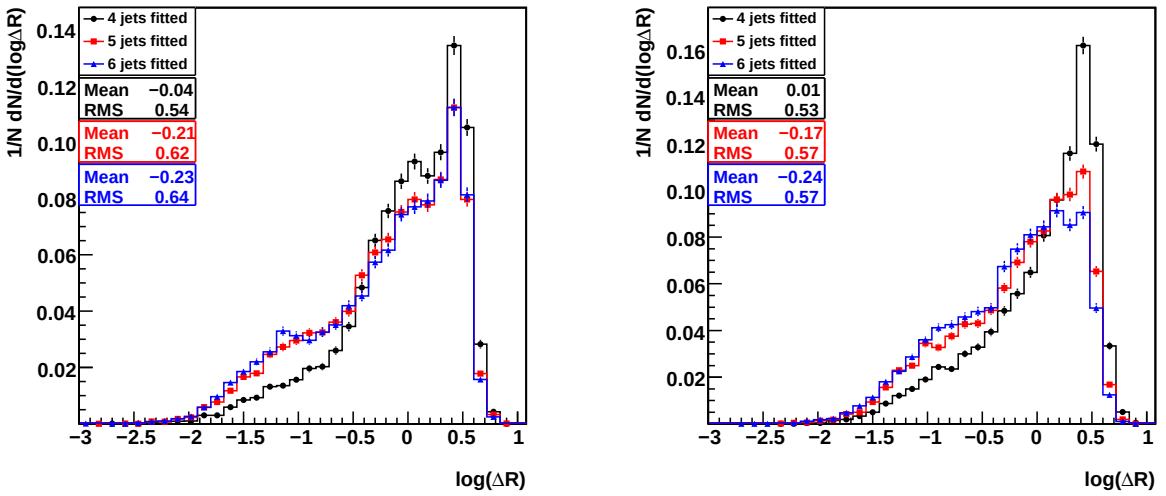

(a) hadronically decaying top quark

(b) leptonically decaying top quark

Figure 6.23.: The distance in ΔR between true and reconstructed top quark are shown in the distributions of the hadronically and leptonically decaying top systems with six jets in the event. Either four jets (black), five jets (red) or six jets (blue) are selected for the fit and are permuted.

correctly associated to their top quarks. Accordingly, more events have a smaller ΔR distance to the true top quarks, which is summarized in Table 6.5.

Table 6.5.: The fraction of events with reconstructed top quarks within a distance in $\Delta R < 0.1$, 0.3, 0.5 to the true top quarks are summarized for the four, five and six fitted jets. For the calculations only events with six measured jets are considered and no matching is required.

	ΔR	Fraction of events in %		
		4 jets fitted	5 jets fitted	6 jets fitted
hadronic	< 0.1	2.10 ± 0.07	4.45 ± 0.11	5.66 ± 0.13
top	< 0.3	2.79 ± 0.06	5.02 ± 0.09	5.81 ± 0.10
quark	< 0.5	3.83 ± 0.07	5.74 ± 0.09	6.36 ± 0.10
leptonic	< 0.1	1.87 ± 0.07	3.56 ± 0.10	4.50 ± 0.12
top	< 0.3	2.88 ± 0.07	4.74 ± 0.09	5.89 ± 0.10
quark	< 0.5	3.60 ± 0.07	5.53 ± 0.09	6.64 ± 0.10

For six jet events, the fraction of well reconstructed events, which have a hadronic or leptonic top quark within a ΔR distance of 0.1 to the true one, can be approximately doubled if five jets are used. Still within a ΔR distance of 0.5 the improvement is roughly 50 %. If six jets are considered in the fit these improvements are even larger. Overall the combinatorial background results in relatively low fractions of events within good ΔR distances. But taking five or six jets in the kinematic fit into account improves the reconstruction of the top quark direction significantly.

Mass The invariant mass of the reconstructed hadronically (m_{jjj}) and leptonically (m_{evj}) decaying top quark are shown in Figure 6.24.

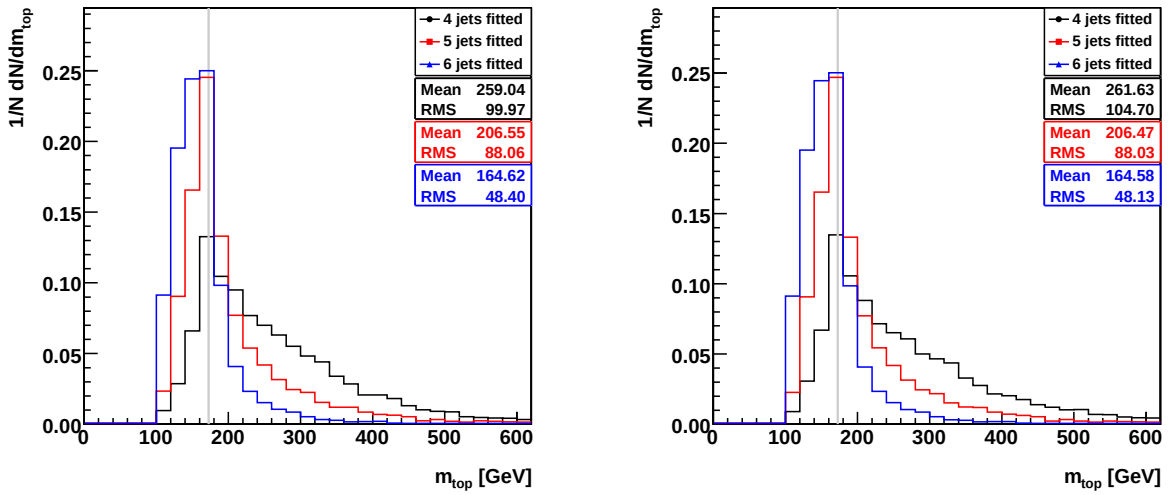

(a) hadronically decaying top quark

(b) leptonically decaying top quark

Figure 6.24.: The invariant mass distributions of the hadronically and leptonically decaying top systems with six jets in the event are shown. Either four jets (black), five jets (red) or six jets (blue) are selected for the fit and are permuted. The mass of 172.5 GeV, which is used in the MC simulation is drawn with a gray vertical line.

The mass value of 172.5 GeV, used in the MC simulation, is drawn as a gray vertical line. As expected, the distributions for the hadronically decaying top looks similar to the leptonically one. All distributions have well established peaks around 172.5 GeV. Both, the hadronic and the leptonic mass peaks are much more pronounced if five or six jets are used in the fit. Almost twice the number of events have a mass value within the bin of the mode. The width of the peaks, represented by the RMS, can be reduced to roughly the half. The mean value for five fitted jets is reduced to 206.55 GeV and 206.47 GeV compared to the mean value of 259.04 GeV and 261.63 GeV for four fitted jets in case of the hadronically and leptonically decaying top quark, respectively. If six jets are taken into account, the mean of the mass distributions is with approximately 165 GeV already smaller than the MC truth value and might indicate that the mass is slightly underestimated.

Transverse Momentum and Angular Variables The transverse momentum of both top quarks can be slightly better reconstructed if more jets are used in the fit, which is presented in Figure 6.25. For $p_T < 400$ GeV the ratio of reconstructed over true values is on average closer to one. Also for boosted top quarks with $p_T > 400$ GeV fitting five jets seems to lead more often to better values. But the statistics in this range is far too low, so that it is of little importance. The underestimation of the p_T is in general less visible for the hadronic top quark, but for the leptonic top quark this is still true and results in less reconstructed events with 200 GeV $< p_T <$ 400 GeV. Especially the dip around 150 GeV is for events with exactly six jets more pronounced than averaging over events with arbitrary jet multiplicity (compare Sec. 6.4). Indications for reasons of the worsening starting at around 200 GeV are given in Section 6.5.2.

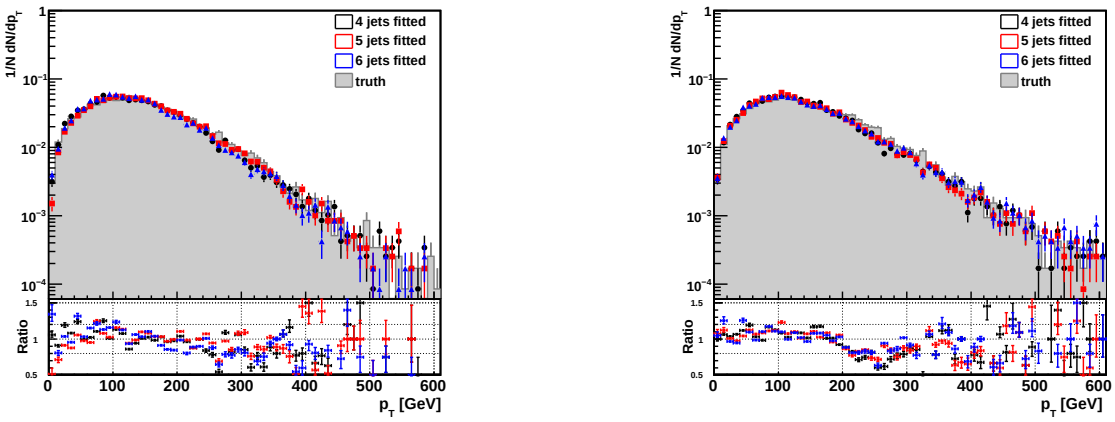

(a) hadronically decaying top quark

(b) leptonically decaying top quark

Figure 6.25.: The transverse momentum distributions of the hadronically and leptonically decaying top systems with six jets in the event are shown. Either four jets (black), five jets (red) or six jets (blue) are selected for the fit and are permuted. The distributions are compared to MC truth information (gray shaded) in a ratio plot of reconstructed over true value.

In general, the fluctuations are too large and the improvement is too small in order to give a quantified statement. Yet taking five or six jets into account can reduce the underestimation.

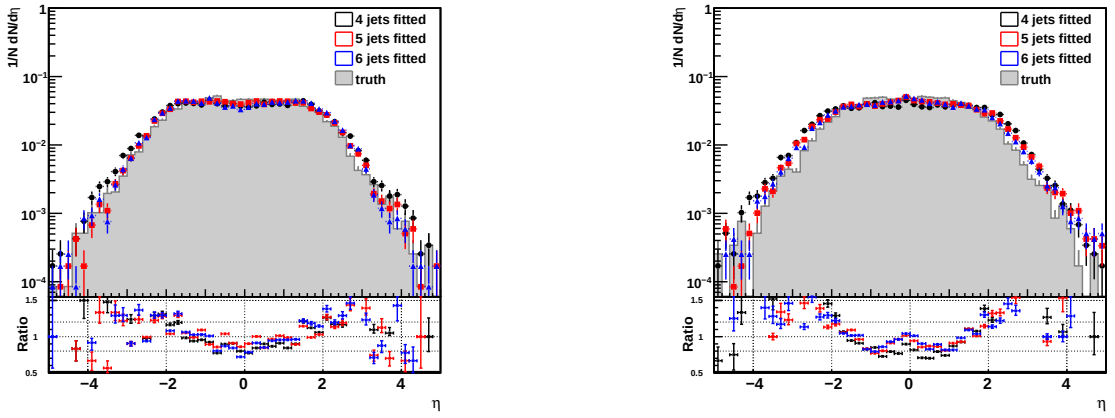

(a) hadronically decaying top quark

(b) leptonically decaying top quark

Figure 6.26.: The η-distributions of the hadronically and leptonically decaying top systems with six jets in the event are shown. Either four jets (black), five jets (red) or six jets (blue) are selected for the fit and are permuted. The distributions are compared to MC truth information (gray shaded) in a ratio plot of reconstructed over true value.

Also an improvement in the reconstruction of the η coordinate of both top quarks is visible in Figure 6.26. In particular if five jets are fitted, the reconstructed η-distribution of the hadronic top quark matches the truth distribution better in the central region of $-2 < \eta < 2$ and there is also a slightly better agreement in the forward region. The downward fluctuations in the central region can be reduced from a relative deviation of 30 % if four jets are used to 20 % if five jets are used. Also the tendency to reconstruct higher η values for the leptonically top quark is less pronounced, although the distribution is still worse reconstructed than for the hadronic top quark. This is due to the uncertainties coming from the free neutrino momentum component p_z. However, the minima at $\eta \approx \pm 0.7$ are less pronounced and in particular in the region around $\eta \approx 0$ the consideration of more jets leads to a more adequate reconstruction.
Since the ϕ coordinate is already well reconstructed if four jets are considered, the comparison is shown in the Appendix C.1.

$t\bar{t}$-System

In fact, using more than four jets in the fit improves most the reconstruction of the $t\bar{t}$-system. This is illustrated in Figure 6.27. The transverse momentum (left) of the $t\bar{t}$-system is completely

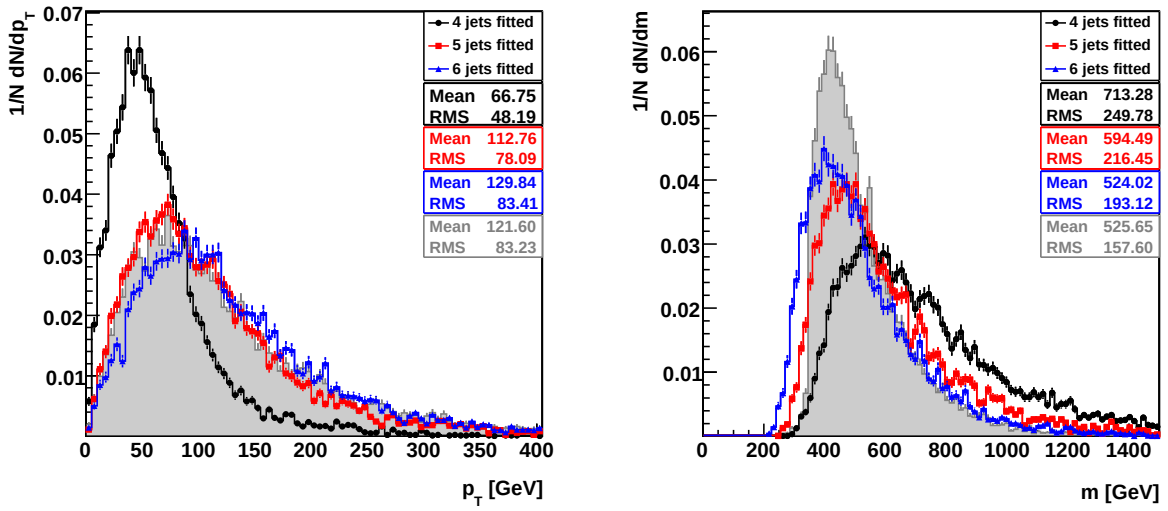

(a) transverse momentum

(b) invariant mass

Figure 6.27.: The transverse momentum and invariant mass distribution of the $t\bar{t}$-system with six jets in the event are shown. Either four jets (black), five jets (red) or six jets (blue) are selected for the fit and are permuted. The distributions are compared to MC truth information (gray shaded).

underestimated if only four jets are permuted in the fit, whereas the distributions for five and six jets matches better the MC truth information. The mean values of 112.76 GeV and 129.84 GeV for five and six jets fitted, respectively, are much closer to the truth value of 121.60 GeV than the mean value of 67.04 GeV, which is reconstructed if four jets are considered. Also the RMS values for five and six fitted jets (78.09 GeV and 83.41 GeV) are similar to the truth value of 83.23 GeV, while the RMS for four fitted jets is significantly too small (49.45 GeV). However, for six fitted jets the transverse momentum seems to be slightly worse reconstructed than for

five fitted jets as the values are marginally overestimated.
Likewise the reconstruction of the invariant mass (right) of the $t\bar{t}$-system can be refined if five or six jets are taken into account. There is still a noticeable discrepancy between the reconstructed and truth values, especially in the peak region, but the mean values show already the correct tendency. Instead of a mean of 713.28 GeV for four fitted jets, which is far off the true value of 525.65 GeV, the reconstruction with five and six fitted jets leads to mean values of 594.49 GeV and 524.02 GeV, respectively. Also the width of the peaks become more narrow and are thus closer to the width of the MC truth information.

6.7. Study of $W \to e\nu +$ jets Background Events

The reconstruction of a $t\bar{t}$ signal sample has been extensively studied in the Sections 6.1 - 6.6. Analyzing data would imply that also background events are used in the kinematic fit to reconstruct the $t\bar{t}$-system and thus would contribute to the studied signal distributions. The background whose kinematics is most similar to the signal is the $W \to e\nu +$ jets background. In the following it is studied whether the kinematic fit forces the $W \to e\nu +$ jets background to mimic the kinematics of the $t\bar{t}$ topology.

6.7.1. Description of the Data

In the lepton + jets channel the dominant background is $W + 4$ jets (see Sec. 2.2.3). In ATLAS mainly ALPGEN [74] is used as the MC generator in order to simulate this background [64]. HERWIG is then further used for the fragmentation and hadronization and JIMMY for simulating the underlying event. The matrix element calculations performed by ALPGEN need to be matched to the parton showers simulated by HERWIG. For this the MLM [75] algorithm performs a slightly more sophisticated matching in η-ϕ-space than described in Section 5.3. The fraction of the background which contains heavy quarks is treated separately in ALPGEN and is thus not included in these studies. The simulated cross section of the sample ($W \to e\nu +$ jets) is 16 163.8 pb. For these studies all simulated processes $W \to e\nu + n$ partons with $n \in [0, 5]$ are used with a correction K-factor of 1.22 applied for considering higher order calculations. The cross sections reported by ALPGEN and JIMMY, the number of events and the integrated luminosity $\mathcal{L}$ are summarized, split in parton numbers and without K-factor in Table 6.6 [64].

Table 6.6.: Summary of simulated cross sections before and after the MLM-matching, integrated luminosities and number of total events in all $W \to e\nu + n$ partons channels with $n \in [0, 5]$. The total number of events are given without any scaling or weighting applied.

channel	σ(ALPGEN) in pb	σ(JIMMY) in pb	$\mathcal{L}$ pb^{-1}	$\mathrm{N}_{\mathrm{events}}$
$W \to e\nu + 0$ partons	12 479.8	10 184.7	299.4	509 500
$W \to e\nu + 1$ partons	5 080.5	2 112.4	301.8	106 000
$W \to e\nu + 2$ partons	2 499.0	676.0	3 004.4	338 500
$W \to e\nu + 3$ partons	1 099.4	203.3	2 990.4	102 000
$W \to e\nu + 4$ partons	431.3	56.1	2 975.9	28 500
$W \to e\nu + 5$ partons	141.5	16.6	3 018.4	8 500

The difference between the cross sections calculated by ALPGEN and JIMMY is due to the MLM

matching algorithm. The ratio of the two numbers represents the MLM matching efficiency. During the matching procedure also a transverse momentum cut on the jets with $p_T > 20$ GeV is applied, thus the MLM matching efficiency is small for large parton multiplicities, e.g. for five partons the efficiency is only roughly 10 %. In order to correct the loss by the MLM matching procedure more events are generated by ALPGEN depending on the MLM matching efficiency for the specific number of partons. Since the cross sections for the parton multiplicities of zero and one are significantly larger than the others, less integrated luminosity is simulated in order to keep the simulation time reasonable. Thus, the relative scaling factor of ten has to be applied to these events if the different channels are used together.
In the MC reconstruction the same object definitions are used as defined in Section 5.1.

Event Selection

The same selection cuts as reported in Section 5.2 are applied to the background sample. The cut flow is presented in Table 6.7. The number of events and the cross section before the

Table 6.7.: Cut flow of the $W \to e\nu +$ jets background sample with all weights and correction factors applied given for number of events, cross section σ, relative ϵ_{rel} and absolute ϵ_{abs} cut efficiencies. The number of events are given for 200 pb^{-1}.

Cut	N_{events}	σ in pb	ϵ_{rel}	ϵ_{abs}
no	3 232 750	16 163.8	1.00	1.00
Pre-selection	1 042 540	5 212.7	0.32	0.32
1 isolated electron, $p_T > 20$ GeV, $\lvert\eta\rvert < 2.5$	770 488	3 852.5	0.74	0.24
> 3 jets, $p_T > 40$ GeV, $\lvert\eta\rvert < 2.5$				
> 1 additional jet, $p_T > 20$ GeV, $\lvert\eta\rvert < 2.5$	2 221	11.1	$2.88 \cdot 10^{-3}$	$0.68 \cdot 10^{-3}$
$\not{E}_T \geq 20$ GeV	1 921	9.6	0.86	$0.59 \cdot 10^{-3}$

selection are the corrected values after the showering process with simultaneous consideration of the MLM matching efficiency and the correction factor of 1.22 for higher order calculations. From originally roughly 3.2 million events only 1921 events pass the selection which means that roughly one out of two thousand events survive the selection cuts. The cross section is reduced from originally 16 163.8 pb to 9.6 pb. In comparison to the cross section of the selected events of the signal sample in Table 5.1 this results in a signal over background ($W + 4$ jets) ratio of 1.67.
In Figure 6.28 the jet multiplicities of the $W \to e\nu +$ jets sample before and after the selection are shown and the jet multiplicity after the selection is compared to the signal jet multiplicity, both normalized to an integrated luminosity of 200 pb^{-1}. As one can imagine from the numbers given in Table 6.7 before the selection most of the events have one, two or three jets. In the first bin alone are more than two million events, which would scale up the plot such that the jet multiplicity after the selection is not visible anymore. Most of the events which pass the cuts (approximately 1 150 events) are in the fourth bin. Only roughly 550 events have five and 150 events have six jets. In the right plot the comparison of the jet multiplicities of signal and background are shown after the selection. In general, the ratio of signal over background events increases for jet multiplicities of four to six jets, the more jets are in the event. In particular the number of events decreases significantly more for background from four to five jet events than for signal.

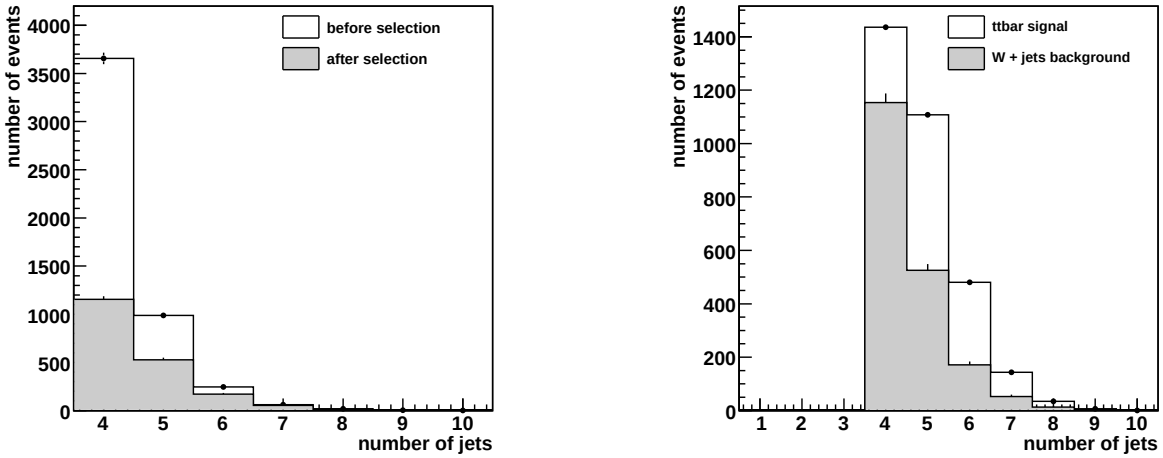

(a) before and after the selection cuts

(b) $t\bar{t}$-signal and $W \to e\nu +$ jets background sample normalized to 200 pb^{-1}

Figure 6.28.: A comparison of the jet multiplicities of the $W \to e\nu +$ jets sample before and after the selection cuts is shown in the left plot. In the right plot the jet multiplicities after the selection cuts of the $W \to e\nu +$ jets background sample and the $t\bar{t}$ signal sample are shown, both normalized to the same integrated luminosity.

6.7.2. Comparison to Signal

For the following studies the KLFitter is used with a free top pole mass to reconstruct the $W + 4$ jets background events. Always the four highest jets in p_T are selected regardless of the jet multiplicity. The electron is not required to be isolated due to a not considered object definition change in the software. The results are compared to reconstructed signal (see Sec. 6.1 - 6.6) results with the same settings for the KLFitter as for the background. Since matching a $t\bar{t}$ decay topology to background truth MC information does not make sense, all studies for which truth matching is required cannot be performed. In all following plots the signal distributions are drawn in black and the $W + 4$ jets background distributions are drawn in red. If a comparison to signal truth information from MC is made, these distributions are plotted shaded in gray. In order to study the effect of the kinematic fit on a non-signal sample and to compare how similar the output is, most of the following distributions are normalized to unity because only the shapes are of interest.

Likelihood Distribution

Generally one would expect notably lower likelihood values for the best permutation of the reconstructed background events. Though as seen in the cut flow of the selection (Sec. 6.7.1) only events with similar kinematics to the top pair decay are selected and most of the events are rejected. Thus the shape of the logarithmic likelihood distributions does not look very different if one compares the normalized distributions (Fig. 6.29).
However, there are visible differences. The main peak, which is in case of signal caused by well reconstructed events, is less pronounced if background is reconstructed. The amplitude of the peak is only 60 % of the one of the signal distribution. Instead, the second peak, which in case of

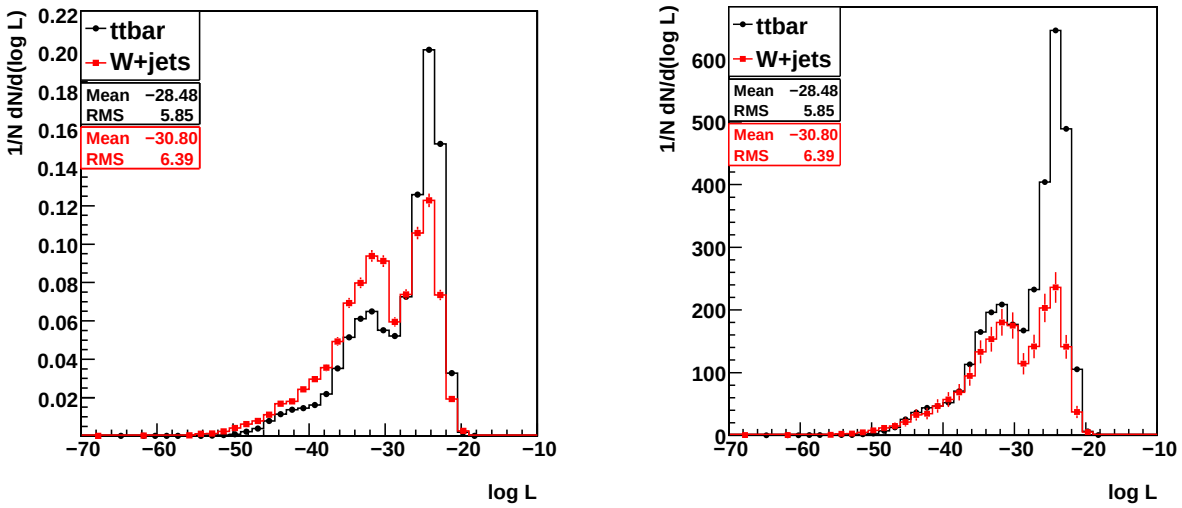

(a) normalized to unity

(b) scaled to 200 pb^{-1}

Figure 6.29.: The likelihood distributions of the best permutations are shown. The background distributions (red) is compared to the signal distribution (black).

signal is caused by combinatorial background, is distinctly stronger developed. These differences allow for some separation power of signal and background. In the right plot the same likelihood distributions are shown but normalized to a luminosity of 200 pb^{-1} in order to get an idea how in data the likelihood distribution might look like. The contribution of the background to the peak around -25 is only one third of the signal contribution.

Top Quark

Mass The top mass is certainly a property, which should only be measurable if a signal event is reconstructed, unless a background event fakes by accident almost perfectly the top pair decay topology. Of course this might happen randomly and especially by the few events which pass the selection cuts. Here not only the shapes of the distributions but also their relative contributions to the overall data are of interest, hence in Figure 6.30 the distributions are shown normalized to unity as well as normalized to an integrated luminosity of 200 pb^{-1}. Because the hadronically and leptonically masses are constrained to be similar and indeed behave also similarly (see Sec. 6.4.1) only the invariant mass distributions of the hadronically decaying top system are shown.
As expected, the invariant mass is poorly reconstructed in case of the $W + 4$ jets background sample. Normalized to unity (left), the distribution follows merely the combinatorial tail of the signal distribution as a broad shoulder. The jets of the background sample can have random properties within the cut criteria and have no relation to one another. No peak is visible around 172.5 GeV. This is even better illustrated if one compares the two distributions normalized to a certain luminosity (right), taking the signal over background ratio into account. The contribution of the background to an assumed overall distribution is rather flat. In a mixed sample the combinatorial tail would grow, but the reconstruction of the top mass via the peak value of the distribution would be hardly affected.

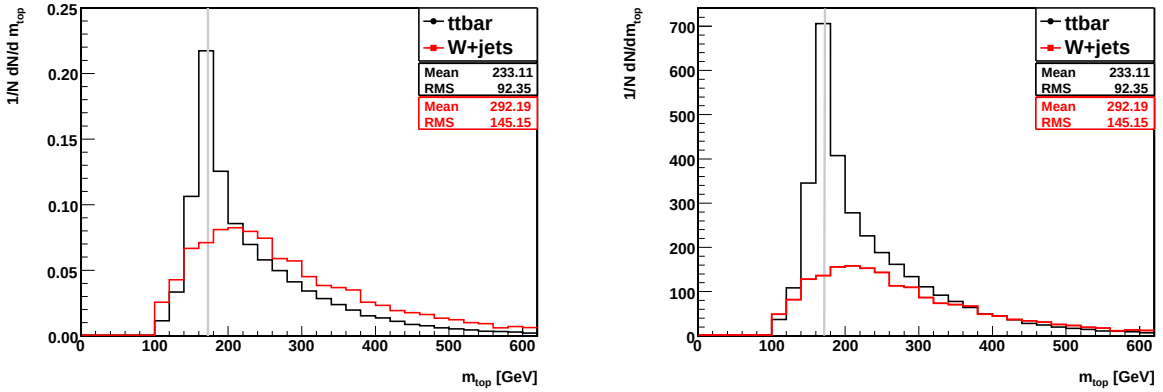

(a) m_{jjj} normalized to unity

(b) m_{jjj} scaled to 200 pb^{-1}

Figure 6.30.: In the left plot the invariant mass m_{jjj} of the three-jet system representing the hadronically decaying top is shown either reconstructed from signal or background. In the right plot the same is shown but normalized to 200 pb^{-1}. The distributions are compared to the top pole mass of MC truth information (gray line) from the signal sample.

Transverse Momentum and Angular Variables In the following it is studied how well the $W + 4$ jets events can imitate the kinematics of the two top quarks after fitting them with the KLFitter. The transverse momentum p_T of the reconstructed hadronically and leptonically decaying top system is depicted in Figure 6.31.

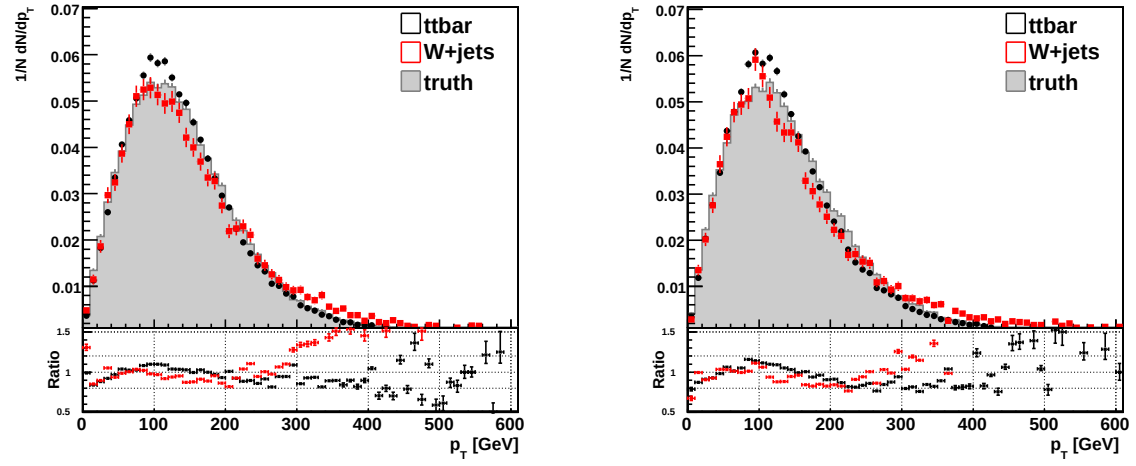

(a) hadronically decaying top quark

(b) leptonically decaying top quark

Figure 6.31.: The p_T-distributions of the hadronically and leptonically decaying top systems, reconstructed either from signal or background, are shown. The distributions are compared to MC truth information (gray shaded) from the signal sample and in a ratio plot of reconstructed over true value.

The KLFitter reconstructs from the background objects a p_T of the hadronically decaying top system, which is pretty close to the true distribution of the signal. For $p_T < 300$ GeV the ratio of reconstructed over true values is even closer to unity than the one of the signal sample, but more events are reconstructed with $p_T > 300$ GeV. Accordingly, high p_T jets created by QCD processes seem to fake the hadronically top decay quite well and the KLFitter further pushes the p_T to the true distribution. The transverse momentum of the leptonically decaying top system reconstructed from background differs slightly more from the true distribution, although the W boson decay in the background sample is the same physical process as the W boson decay in the top decay. But the broad transfer functions of the jets might increase the freedom in the kinematic fit for the reconstruction of the hadronically decaying top quarks. Again more events with high p_T are reconstructed, but the deviations of signal and background to the true distributions are quite comparable. In Figure 6.32 the η-distributions of the reconstructed hadronically and leptonically decaying top system are shown.

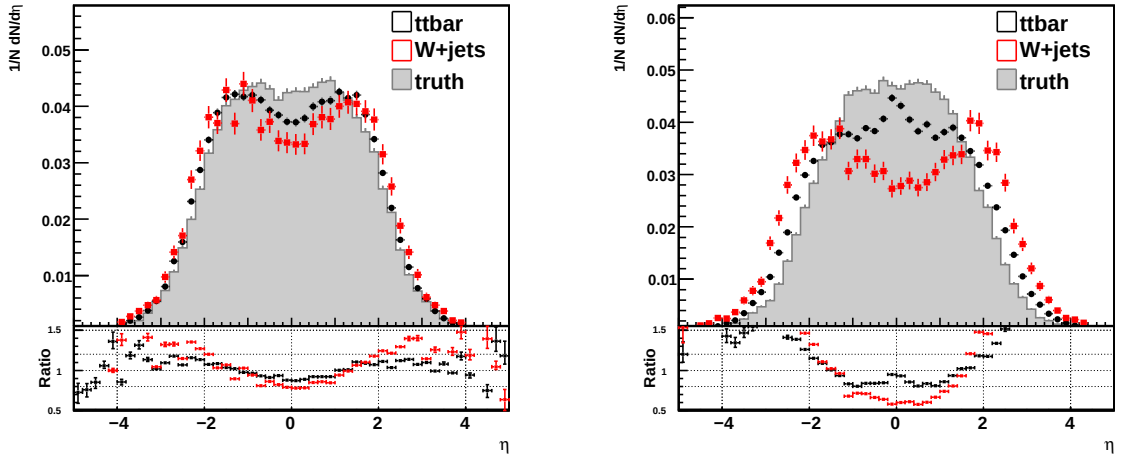

(a) hadronically decaying top quark

(b) leptonically decaying top quark

Figure 6.32.: The η-distributions of the hadronically and leptonically decaying top systems, reconstructed either from signal or background, are shown. The distributions are compared to MC truth information (gray shaded) from the signal sample and in a ratio plot of reconstructed over true value.

Clearly less events are reconstructed from background with top quark η in the central region of $-2 < \eta < 2$, especially in case of the leptonically decaying top quark system. On the contrary to the signal sample a dip is visible around $\eta = 0$, which results in differences of up to 50 % from the true distribution. Hence, more hypothetical top quarks are reconstructed in the forward region. Jets, which come from QCD background processes propagate in all directions and the $\not{E}_T$ -distribution of the $W + 4$ jets background events does not match the signal distribution. The reconstruction of the neutrino p_z is barely constrained, which results in a significantly broader distribution in case background is used. and thus might be arbitrary chosen in case of the background events. The ϕ distributions, which are as expected quite uniformly distributed, are compared in Appendix C.2.

$t\bar{t}$-System

The reconstruction of the $t\bar{t}$-system is like the top quark mass a good measure to evaluate the reconstruction of the background sample, because all objects have an effect on this complex system. The transverse momentum and the invariant mass of the $t\bar{t}$-system, reconstructed from background, are compared to the signal reconstruction and its truth MC information in figure 6.33.

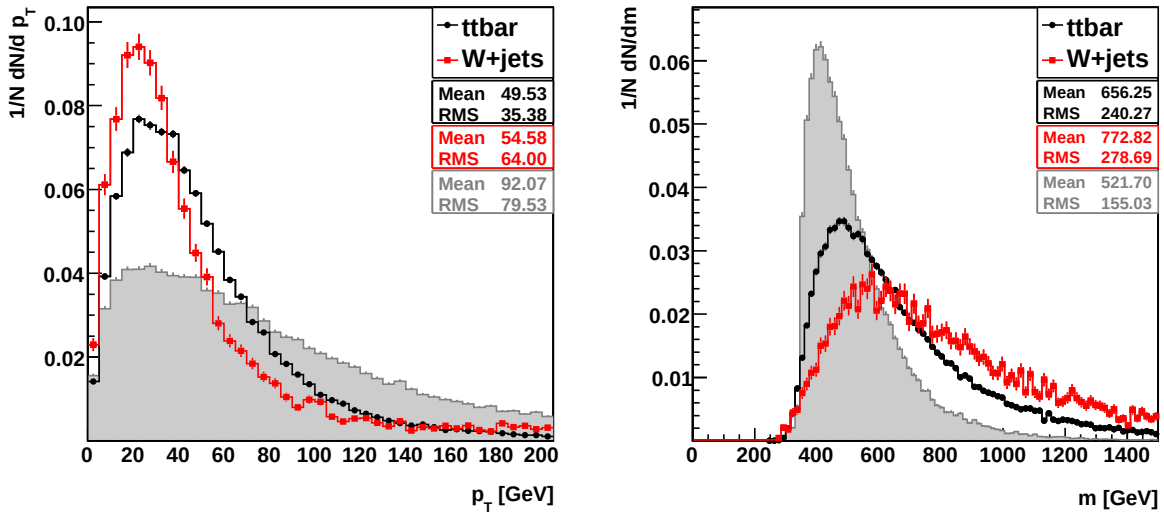

(a) transverse momentum

(b) invariant mass

Figure 6.33.: The transverse momentum and invariant mass distribution of the $t\bar{t}$-system, reconstructed either from signal or background, are shown. The distributions are compared to MC truth information (gray shaded) from the signal sample.

The distribution of the transverse momentum coming from the reconstruction of the background sample is reconstructed with even lower values than the signal, thus the difference to the true distribution is yet larger. Although the peak around 30 GeV is more pronounced than the signal, the mean (54.58 GeV) and the RMS (64.00 GeV) values are larger than the ones in the signal sample (49.53 GeV and 35.58 GeV), which means that also more events are reconstructed with high p_T values. The reconstructed invariant mass distribution has a mean value of 772.82 GeV, which is significant larger than the true value of 521.70 GeV. Moreover the distribution is much more spread as a consequence of forcing arbitrary jets, electrons and $\not{E}_T$ to a $t\bar{t}$ topology, which do not belong to each other and are mostly uncorrelated.

6.7.3. Reconstruction of Five Jet Events

In the same way the signal sample has been studied with different jet multiplicities in Section 6.6 this is done for the background sample. One might be concerned whether fitting more jets of the background sample allows for an even more similar reconstruction compared to the signal sample. Using the first five jets ordered in p_T was the most promising approach for the signal, consequently the reconstruction of the background sample is studied with a jet multiplicity of five jets as an example comparing four and five fitted jets. Besides the statistics for background

events with six jets after the selection is already slightly too low (see Fig. 6.28). Note that these studies complete the signal studies of Section 6.6 for five measured jets as well. The KLFitter is again used with the top pole mass as a free parameter and in all studies no matching is required. In all plots, depending on whether four or five jets are selected and permuted, the signal is drawn in black and dark-gray, while the $W \to e\nu +$ jets background is drawn in dark-red and red, respectively. If markers are used, they are filled for signal and empty for background. Four fitted jets are drawn as circles, whereas five fitted jets are drawn as rectangles. If a comparison to MC truth is made, this is plotted shaded in gray.

Likelihood Distribution

In Figure 6.34 the logarithmic likelihood distribution and the permutation probability are shown for the described configuration. The dark colours show the distributions for four fitted jets, in

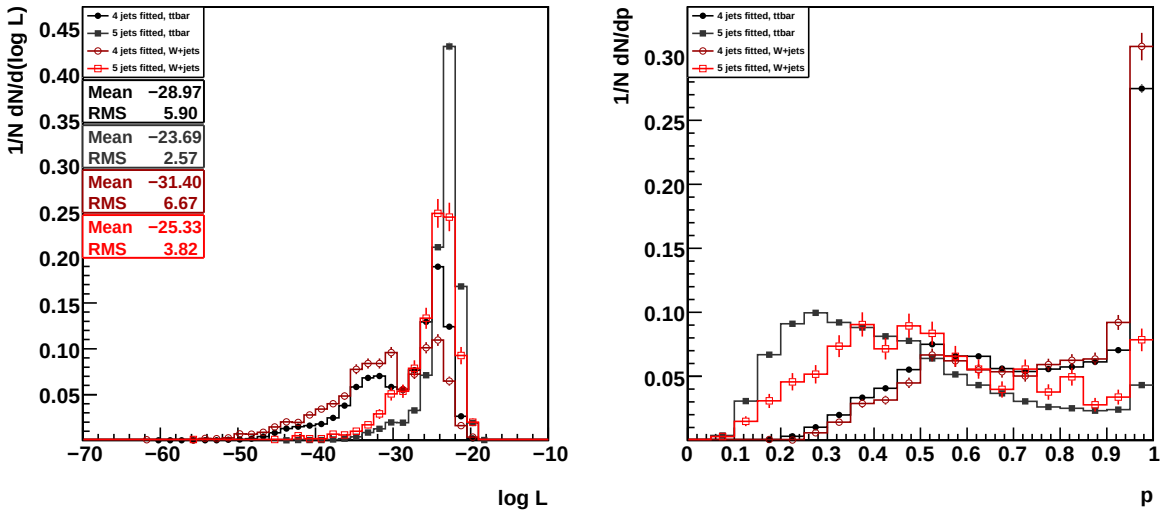

(a) likelihood distributions

(b) permutation probabilities

Figure 6.34.: The likelihood distributions and the permutation probability of the best permutations in five jets events are shown for the two different configurations of the KLFitter on a logarithmic scale. Either four jets (darker colours and circular markers) or five jets (lighter colours and rectangular markers) are selected for the fit and are permuted. The background distributions (red) is compared to the signal distribution (black), both are normalized to unity.

both cases of background and signal the second peak around -33 vanishes if five jets are fitted (lighter colours). Thus this peak probably only arises if really a bad configuration of jets is associated with the partons of the $t\bar{t}$ decay. Still for five fitted jets the background distribution is notably broader than the signal distribution and the peak around -24 is roughly 40 % less pronounced. Particularly, in consideration of the logarithmic scale there is still separation power in the likelihood distribution of signal and background.
The distributions of the permutation probabilities for the best permutation show that in case of signal the separation to the other permutations is slightly weaker than in case of background, especially if five jets are fitted. This means that already the second best permutation of the

background distribution returns a considerable worse likelihood value. Presumably, if a configuration is found for background, which mimics well the $t\bar{t}$ decay, it is unlikely to find another one with comparable properties. Permuting jets in the signal sample, for instance jets of the hadronically hemisphere, seems to be less critical.

Top Quark

Mass The invariant three-jet mass m_{jjj} of the three jets which build the topology of the hadronically decaying top quark is shown on the left-hand side, while the invariant mass of the remaining jet, electron and neutrino is shown on the right-hand side in Figure 6.35.

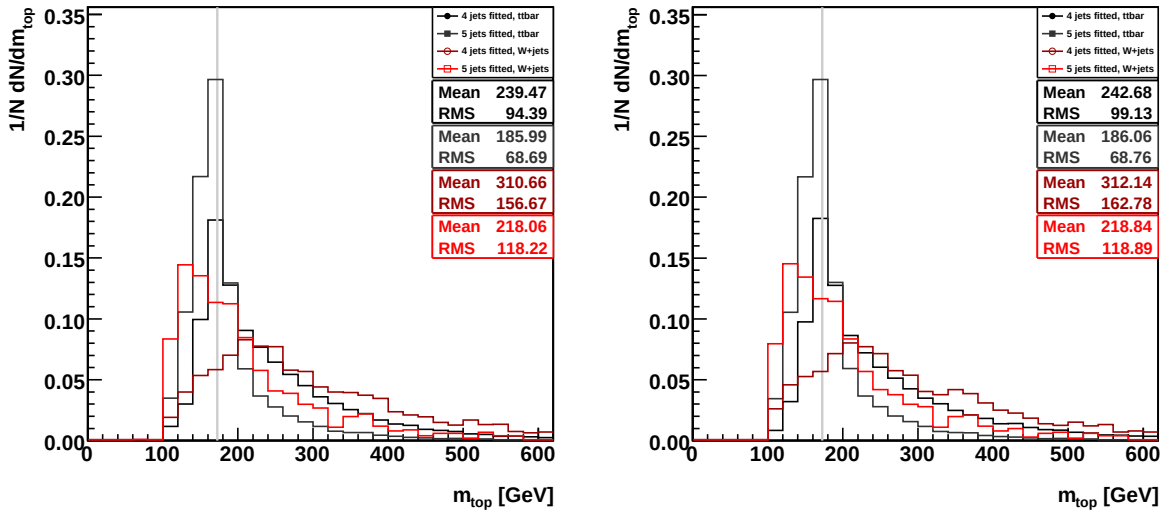

(a) hadronically decaying top quark system

(b) leptonically decaying top quark system

Figure 6.35.: The invariant mass m_{jjj} of the three-jet system representing the hadronically decaying top and of the corresponding invariant mass $m_{je\nu}$ representing the leptonically decaying top are shown for five jet events. Either four jets (darker colours and circular markers) or five jets (lighter colours and empty markers) are selected for the fit and are permuted. The background distributions (red) are compared to the signal distribution (black). Both are normalized to unity. The mass value of 172.5 GeV, which is used in the MC simulation is drawn as a gray vertical line.

As one might expect the invariant masses m_{jjj} and $m_{je\nu}$ look very similar in all cases. Whereas the shape of the background distribution for four fitted jets looks mainly like the part of the signal distribution which is dominated by combinatorics, for five fitted jets a small peak arises around the true mass value of 172.5 GeV. Still the peak of the signal is much more pronounced and even twice the amplitude of the background distribution if five jets are fitted. But indeed one can see that additional jets provide the KLFitter with more possibilities to reconstruct two fake top quarks with reasonable masses. However, taking the signal over background ratio into account this effect is not very dramatic.

Transverse Momentum and Angular Variables In Section 6.7.2 it was already stated that background events show the tendency to be reconstructed with higher top quark p_T. This

is even better visible in the logarithmically plotted transverse momentum of the hadronically and leptonically decaying top system in Figure 6.36.

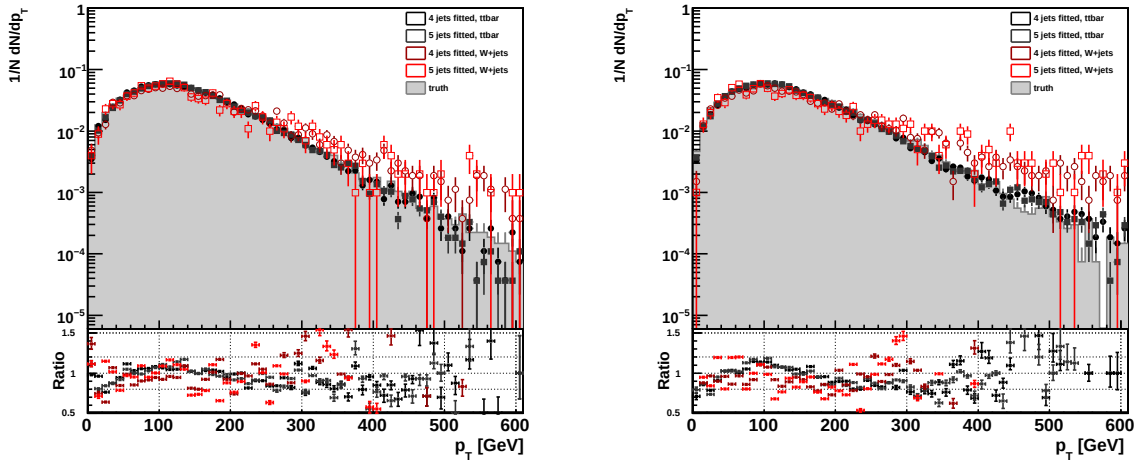

(a) hadronically decaying top quark system

(b) leptonically decaying top quark system

Figure 6.36.: The transverse momentum distributions of the hadronically and leptonically decaying top systems with five jets in the event are shown on a logarithmic scale. Either four jets (darker colours and circular markers) or five jets (lighter colours and rectangular markers) are selected for the fit and are permuted. The background distributions (red) are compared to the signal distribution (black), both normalized to unity, and to MC truth information (gray shaded) from the signal sample in a ratio plot of reconstructed over true value.

To be more precise, noticeably more events are reconstructed out of the background sample with $p_T > 250$ GeV compared to the signal truth information. If five jets are fitted the difference to the signal distribution is marginally smaller in these region. On the contrary the signal seems to be fairly well reconstructed if five jets are fitted at least up to p_T values of 500 and 400 GeV for the hadronically and leptonically decaying top quark system, respectively. In the region of $p_T < 250$ GeV the background sample is closer to the true signal distribution reconstructed if five jets are fitted instead of four jets, but still with large fluctuations. Whereas for signal the deviations of the reconstructed values is always smaller than 20 % compared to the true values and considering four or five jets in the kinematic fit results in similar distributions.
In Figure 6.37 the η distributions of the hadronically and leptonically decaying top system are shown reconstructed from $W \to e\nu +$ jets background and $t\bar{t}$ signal. The distribution for the hadronically decaying top quark shows less background events with η in the center region ($-2 < \eta < 2$), but fitting five jets can return ratio values closer to one. However, the fluctuations are stronger than for the signal sample. Too many events are reconstructed in the forward region, considering five jets leads to comparable results as considering four jets. As already mentioned in Section 6.7.2 the distribution for the leptonically decaying top quark shows a dip in the center region, fitting five jets results in no visible change for the background. In contrast, the signal distribution shows not only in the center region but also in the forward region a slightly better ratio of reconstructed over truth values.

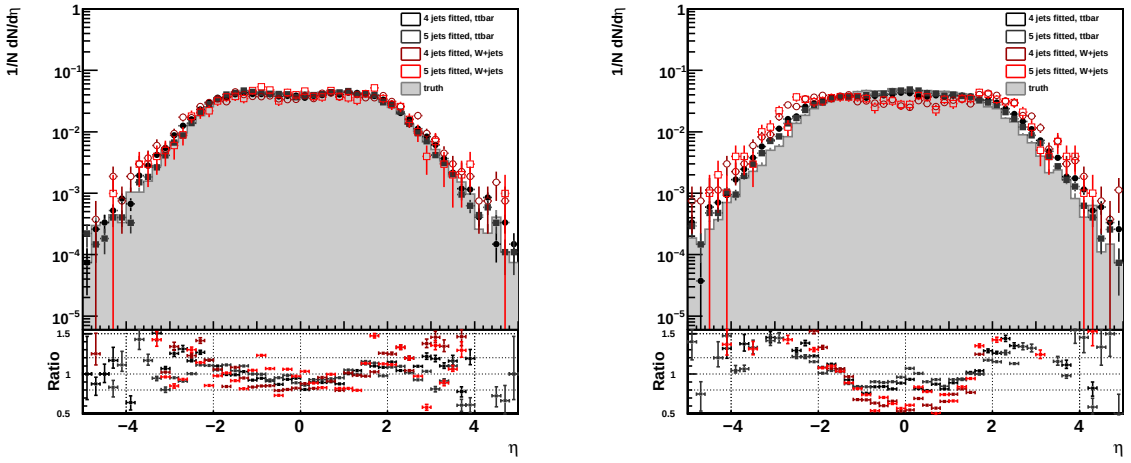

(a) hadronically decaying top quark system

(b) leptonically decaying top quark system

Figure 6.37.: The η-distributions of the hadronically and leptonically decaying top systems with five jets in the event are shown on a logarithmic scale. Either four jets (darker colours and circular markers) or five jets (lighter colours and rectangular markers) are selected for the fit and are permuted. The background distributions (red) are compared to the signal distribution (black), both normalized to unity, and to MC truth information (gray shaded) from the signal sample in a ratio plot of reconstructed over true value.

$t\bar{t}$-System

Finally, the reconstructed transverse momentum and invariant mass of the $t\bar{t}$-system are shown in Figure 6.38, obtained from either the background or the signal sample. Both, the background and the signal distributions of the transverse momentum differ significantly less from the signal's true distribution if five jets are permuted in the reconstruction. Even though the signal distribution show slightly better mean and RMS values compared to the true ones, the changes are comparable for the signal and for the background.
This is also true for the invariant mass of the $t\bar{t}$-system, but since the signal distribution is initially closer to the truth reconstructed if four jets are used in the fit, this holds still if five jets are fitted. These plots might suggest that the improvements in the reconstruction of the signal sample if more jets are used in the kinematic fit might only be the result of additional uninvolved jets, which match by accident the decay topology of the $t\bar{t}$ better than the former used jets. As a matter of fact, the kinematic fit can force the background events closer to the event topology of the $t\bar{t}$ decay if more jets are selected and permuted in the reconstruction, simply by having more adequate possibilities. But since the matching efficiency also increases remarkably, which cannot be only a random effect, the conclusion is still that jets coming from the $t\bar{t}$ decay are not selected in the signal sample if only exactly four jets are chosen. One should not forget that the kinematics of the $W \to e\nu +$ jets events is most similar to the one of $t\bar{t}$ events of all background events. Furthermore, less than one out of thousand $W \to e\nu +$ jets events passes the selection. These particular events might have originally already similar kinematics and especially if more jets with such specific kinematics are available, the reconstruction can result in

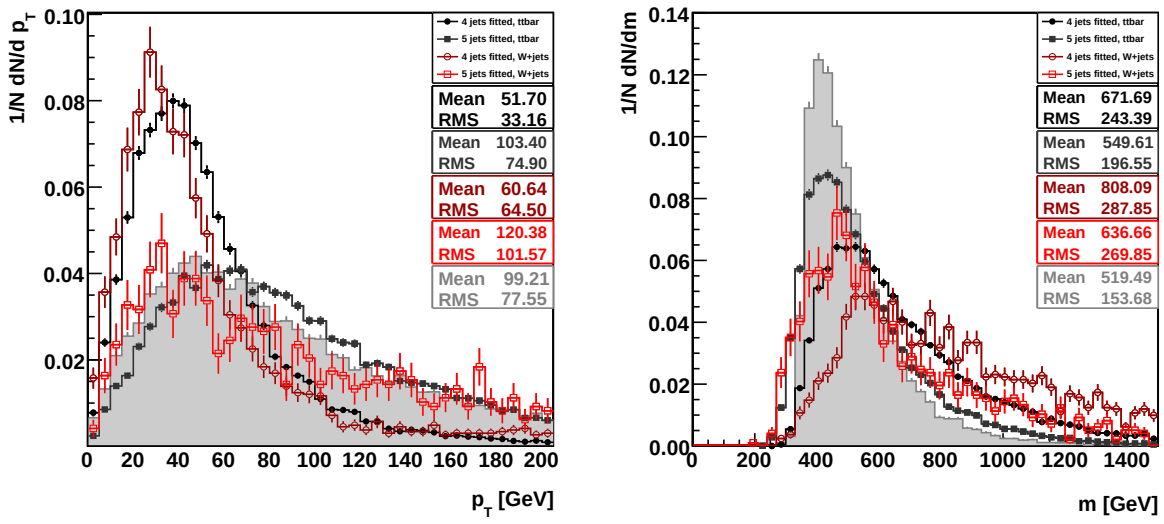

(a) transverse momentum

(b) invariant mass

Figure 6.38.: The transverse momentum and invariant mass distribution of the $t\bar{t}$-system with five jets in the event are shown. Either four jets (darker colours and circular markers) or five jets (lighter colours and empty markers) are selected for the fit and are permuted. The background distributions (red) is compared to the signal distribution (black), both normalized to unity, and with MC truth information (gray shaded) from the signal sample.

a similar topology to the one of the $t\bar{t}$ decay. On the other hand, important properties like the top mass or the invariant mass of the $t\bar{t}$ are as expected still significantly closer to the truth information reconstructed from $t\bar{t}$ signal events than from background events. Apart from this, the comparisons are made mainly without taking the signal over background ratio into account in order to evaluate the reconstruction of the KLFitter, meaning the shapes of the distribution. In Section 6.7.2 an idea was given how large the real contribution of the $W \to e\nu +$ jets events is to a mixed sample. As shown in Figure 6.28 the signal over background ratio is even larger for jet multiplicities of five and six. Certainly, the contribution is too small to play a major role for instance in the mass measurement.

7. Conclusion and Outlook

A proper $t\bar{t}$ reconstruction is crucial for understanding of the ATLAS detector, for measurements of the top quark properties and for further studies which aim to discover physics beyond the Standard Model. In the following the results of the $t\bar{t}$ reconstruction presented in this thesis are summarized and some ideas for further improvements of the reconstruction are given.

7.1. Summary and Conclusion

In this thesis a kinematic likelihood fitter, the KLFitter package, has been presented and has been applied to ATLAS Monte Carlo data for studying the reconstruction of the $t\bar{t}$ decay in the electron + jets channel. The KLFitter is a statistical tool, which uses the maximum likelihood method and energy-momentum conservation in the decay topology in order to find the correct assignment of jets to the final state particles of the hard scattering process and to find better estimators for the measured values. The likelihood approach allows for a general treatment of modeling the input distributions by using asymmetric transfer functions as well as for soft kinematic constraints with user-defined characteristics. A simple truth matching in η-ϕ-space has been performed in order to evaluate the performance of the KLFitter. The matching efficiency increases strongly with the number of jets considered and can thus vary between 7 % and 54 %. At first, the performance of the KLFitter has been studied for the case that the four jets with the highest transverse momentum are considered in the kinematic fit. The KLFitter has been used in the two different configurations of treating the top pole mass as a free and fixed parameter. As expected, the latter leads in general to a better reconstruction of the event. It has been shown that in approximately 54 % and 64 % of the matched events all jets are correctly assigned to their corresponding partons if the top pole mass is either free or fixed, respectively. The estimated energy resolutions of the hadronic and leptonic b-jets are by 21 % and 40 % sharper than the measured energy resolution if the top pole mass is fixed. If it is treated as a free parameter there are no significant improvements visible, but in any case the estimated resolutions are much more centered around zero compared to the measured values.
zero? The reconstruction of the kinematic top quark properties has been discussed. If the top pole mass is free the direction of the hadronically decaying top quark is generally better reconstructed than the one of the leptonically decaying top quark due to uncertainties in the reconstruction of the neutrino momentum. Fixing the top pole mass further improves the reconstruction of the direction. In case no matching is required the direction of the leptonic top quark is then more adequately reconstructed than the one of the hadronic top quark. If the top pole mass is treated as a free parameter the top quark mass can be estimated. As expected, the distributions of the hadronically and the leptonically decaying top quark mass look very similar and have a well pronounced peak around the mass value of 172.5 GeV, which has been used in the MC simulation. The reconstructed transverse momentum of the top quarks matches well the MC truth information in the range up to 400 GeV. The distribution of the pseudorapidity η is in good agreement with the true distribution in the center region ($-2 < \eta < 2$), but shows significant deviations in case of the leptonic top quark in the forward region ($|\eta| > 2$). This is due to uncertainties in the neutrino momentum reconstruction. The reconstructed azimuthal

angle ϕ is - as the true value - uniformly distributed with only variations (± 10 %) from the truth. The transverse momentum and the invariant mass of the $t\bar{t}$-system are only insufficiently reconstructed and show large discrepancies to the truth information.
The reconstruction of the hadronically and leptonically decaying hemispheres has been studied in more detail. As expected, permuting the jets coming from the hadronically decaying top quark does not affect the reconstructed direction of the top quark. It could be shown that using uninvolved jets or jets that have been deflected by FSR has only a minor effect on the reconstructed top quark direction as long as the other jets are correctly associated with their top quark hemisphere. Only if jets are interchanged between their hemispheres the reconstruction worsens dramatically. Thus generally, the reconstruction can be significantly improved if only events are considered, in which the two top quark hemispheres are well separated meaning with η values in the center region ($-2 < \eta < 2$) and with p_T larger than 150 GeV. Unfortunately, for top quarks with p_T larger than 250 GeV jets coming from the hadronically decaying top quark might be merged together and might be identified as a single jet. Consequently, uninvolved jets are used for the reconstruction which leads again to badly reconstructed events.
Next an alternative approach has been presented. It takes more than only the first four jets with the highest momentum into account in the kinematic fit. Although it becomes much more unlikely to find the correct assignment for the jets due to the raising number of permutations, the total number of correctly reconstructed events could be increased. The number of matched events increases significantly if more jets are taken into account, which indicates that jets which have their origin in the $t\bar{t}$ decay would not be selected if only the first four jets were used. The total efficiency, the product of matching efficiency and reconstruction efficiency, can be relatively improved by 23 % if five jets are considered in the kinematic fit for jet multiplicities of five and six.
The effect of considering more jets on the fitting results has been studied exemplary in events with six measured jets after the selection cuts. If more jets are considered in the fit, the resulting likelihood distribution is much sharper which suggest that less bad events are treated. In a few percent of the events the reconstructed W boson mass deviates significantly from the pole mass of the W boson if only the four highest jets in p_T are used in the reconstruction. The resulting side tails in the distributions can be suppressed if more jets are considered. Moreover, the reconstruction of the kinematic properties of the top quarks can be improved. In significantly more events the top quark directions are more adequately reconstructed. Also the top quark mass peaks are much more pronounced and sharper. Marginally improvements are visible in the reconstruction of the transverse momentum and the pseudorapidity of the top quarks. Overall this results in a remarkably better reconstructed top pair system. The transverse momentum is then in appropriate agreement with the MC truth information. The invariant mass is still slightly overestimated but better reconstructed than before. Considering six jets instead of five leads to no observable improvement in total efficiency or in the reconstruction of the objects compared to five jets. However, the computing time is much larger because 180 permutation have to be fitted for each event instead of 60 or 12 permutations for five and four jets, respectively.
Finally, the kinematic fit has been performed with $W \to e\nu +$ jets background events and the results have been compared to the reconstructed signal events. First, again only the four highest jets in p_T have been considered in the fit. The likelihood distribution for background events differs from the one for signal such that this can be used to separate signal from background. If the top quark mass is reconstructed from background this results in a broad shoulder to higher energies, which is comparable in the shape to the contribution coming from combinatorial background in the signal case. The distribution of the transverse momentum of the top quarks is

similar to the signal distribution for $p_T < 300$ GeV but differs significantly from the signal truth information for higher values. The η distributions of the hadronic top quark are comparable to the signal distribution with slightly less events reconstructed in the range of $-2 < \eta < 2$ and more events reconstructed in the forward region. Large differences compared to the signal are observable in the η distributions of the leptonic top quark in the center region, whereas both signal and background differ from the MC truth information for signal in the forward region. The reason for this is mainly the little constrained z-component of the neutrino's transverse momentum. The ϕ coordinate is, as for signal, uniformly distributed. Furthermore, the reconstructed $t\bar{t}$-system disagrees clearly with the truth information of the signal.
In the same manner the signal has been studied considering more jets, this has been performed for the background using five jet events. Also for background the likelihood distribution becomes sharper but is still well separable from the one of the signal. The distributions of the hypothetical top quark masses show a small but broad peak around the true value. There is no notable change visible in the reconstruction of the kinematic variables p_T, η and ϕ of the top quarks. The differences of the reconstructed transverse momentum and invariant mass of the $t\bar{t}$-system to the truth information is also for background significantly smaller if more jets are taken into account. The requirements of the selection cuts result in jets with similar properties to the $t\bar{t}$ events. Having more choices of jets which might match the $t\bar{t}$ topology leads thus to an even more indistinguishable imitation of the top pair decay. Since the signal over background ratio has to be taken into account, which is on average 1.67 and even larger for events with five or six jets, the total contribution should be still reasonably small.
In conclusion, the KLFitter is a powerful tool to reconstruct $t\bar{t}$ events with high reconstruction efficiencies and well estimated object properties. After extensively studying the performance, a new recommendation for using the KLFitter can be given. The four jets with the highest p_T should only be considered if exactly four jets are measured otherwise five jets should be taken into account. This does not only improve the total efficiency but also leads to much more appropriate reconstructed objects. However, depending on the specific analyses the systematical uncertainties might differ significantly if four or five jets are considered and thus need to be studied first. In some studies it might be important to have very pure and well reconstructed events. This can be achieved by cutting on η and p_T of the top quarks. The kinematic properties of $W \to e\nu +$ jets events which pass the selection cuts are quite similar to the ones of the signal. Using the likelihood output of the KLFitter allows for further discrimination of the signal from the background. However, taking more than four jets into account makes it more likely for the background to mimic the $t\bar{t}$ topology, but crucial properties like the top quark mass still differ significantly from the signal.

7.2. Outlook: Plans, Improvements and Comparisons

In this thesis the reconstruction of the $t\bar{t}$ decay with the KLFitter has been studied on a simulated MC sample. The next important step is to validate the obtained results in data by a detailed comparison. For this it is essential to understand separately the different effects of the input model, e.g. of the transfer functions and the constraints. The complex $t\bar{t}$ topology is simultaneously affected by many model assumptions, thus it might be useful to test different transfer functions and different constrained models in a simpler scenario. First studies show that there is quite a potential to further improve the reconstruction with more accurate modeled transfer functions.
The KLFitter has been already tested in the muon + jets channel of the $t\bar{t}$ decay and similar re-

sults as for the electron + jets channel could be obtained [76]. The reconstruction of comparable topologies in for instance supersymmetric decays can be easily implemented and are interesting to study in order get indications for potential issues.
Ongoing studies show that the likelihood is indeed a good variable to discriminate background from signal. Considering five jets further increases the discriminating power of the logarithmic likelihood [76]. First studies indicate that a simple cut on the likelihood can also improve the signal reconstruction of the objects.
Although the KLFitter performs already quite well, further improvements can be made. The neutrino momentum component p_z is little constrained, because in the W boson mass constraint both neutrino solutions are equivalent (see App. A.2). In case the top pole mass is treated as a free parameter, only the similar top quark mass constraint results in some sensitivity to the correct global minimum. Due to the large uncertainties in the jet energy measurements quite often the wrong neutrino p_z solution is chosen to be the best depending on the minimizing technique. This results in badly reconstructed events and also larger combinatorial background. This issue needs still to be studied in more detail.
As mentioned, b-tagging techniques can be used in the KLFitter to further improve the reconstruction efficiency and the properties of the reconstructed objects. Either jet weights, which are based on the impact parameter and the secondary vertex, can be used to define a b-tag depending on a specific cut value, or the distribution of the weights can be directly used as prior probabilities in the likelihood function. First studies indicate that in this way the reconstruction efficiency can be increased to values in the range of 70 % in case the four highest jets in p_T are used in the kinematic fit [77]. The use of b-tagging is expected to have an even more positive effect on the reconstruction if more than four jets are considered.
The KLFitter is being used in various $t\bar{t}$ analyses such as measuring the mass or the charge of the top quark, determining the W boson helicity in the decay of top quarks and for measurements of the $t\bar{t}$ production cross section. Since the structure of the KLFitter package enables the implementation of any decay process the potential of the KLFitter is immense and in particular interesting for complex signatures such as many supersymmetric decays. However, the modeling of the likelihood function has to be handled with care and extensive studies are necessary for each new implementation to obtain full confidence of the results.

A. Auxiliary Calculations

A.1. Derivation of the Constraints

The kinematic constraints are described by Breit-Wigner functions of the W boson and top quark masses. The invariant masses of the W bosons and of the top quarks need to be calculated from the four-momentum vectors p_i of the final state particles in order to be only dependent on the fitting parameters. The angle θ_{ij} between the momentum vectors $\vec{p_i}$ and $\vec{p_j}$ of two particles is obtained from the angular fitting parameters $\Omega_i = (\eta_i, \phi_i)$.

Hadronically Decaying W Boson The mass of the hadronically decaying W boson is reconstructed from the invariant mass of the two light quarks q and $\bar{q}$ and can be expressed by the fit parameters E_q, $E_{\bar{q}}$, Ω_q and $\Omega_{\bar{q}}$ and the energies of the two light quarks:

$$\begin{aligned} m_{q\bar{q}}^2 &= (p_q + p_{\bar{q}})^2 \\ &= m_q^2 + m_{\bar{q}}^2 + 2E_qE_{\bar{q}} - 2|\vec{p}_q||\vec{p}_{\bar{q}}|\cos\theta_{q\bar{q}} \\ &\approx 2E_qE_{\bar{q}}\,(1 - \cos\theta_{q\bar{q}}) \quad , \end{aligned} \tag{A.1}$$

with negligible light quark masses m_q, $m_{\bar{q}}$.

Leptonically Decaying W Boson The mass of the leptonically decaying W boson needs to be expressed by the lepton energy E_l and direction Ω_l and the momentum components of the neutrino $p_{x,y,z}$:

$$\begin{aligned} m_{l\nu_l}^2 &= (p_l + p_{\nu_l})^2 \\ &= m_l^2 + m_{\nu_l}^2 + 2E_lE_{\nu_l} - 2|\vec{p}_l||\vec{p}_{\nu_l}|\cos\theta_{l\nu_l} \\ &\approx 2E_l\sqrt{p_{x_{\nu_l}}^2 + p_{y_{\nu_l}}^2 + p_{z_{\nu_l}}^2}\,(1 - \cos\theta_{l\nu_l}) \quad , \end{aligned} \tag{A.2}$$

where $\theta_{l\nu_l}$ depends on the neutrino momentum components and the direction of the charged lepton Ω_l. The lepton masses are neglected.

Hadronically Decaying Top Quark The mass of the hadronically decaying top quark can be expressed by the energies and directions of the b-quark E_b, Ω_b and the two light quarks E_q, $E_{\bar{q}}$, Ω_q, $\Omega_{\bar{q}}$.

$$\begin{aligned} m_{q\bar{q}b}^2 &= (p_q + p_{\bar{q}} + p_b)^2 \\ &= m_q^2 + m_{\bar{q}}^2 + m_b^2 \\ &\quad + 2E_qE_{\bar{q}} - 2|\vec{p}_q||\vec{p}_{\bar{q}}|\cos\theta_{q\bar{q}} + 2E_qE_b - 2|\vec{p}_q||\vec{p}_b|\cos\theta_{qb} + 2E_{\bar{q}}E_b - 2|\vec{p}_{\bar{q}}||\vec{p}_b|\cos\theta_{\bar{q}b} \\ &\approx m_b^2 + 2E_qE_{\bar{q}}\,(1 - \cos\theta_{q\bar{q}}) \\ &\quad + 2E_qE_b\left(1 - \frac{|\vec{p}_b|}{E_b}\cos\theta_{qb}\right) + 2E_{\bar{q}}E_b\left(1 - \frac{|\vec{p}_b|}{E_b}\cos\theta_{\bar{q}b}\right) \end{aligned} \tag{A.3}$$

with negligible light quark masses m_q, $m_{\bar{q}}$:

Leptonically Decaying Top Quark The mass of the leptonically decaying top quark can be expressed by the energies and directions of the b-quark E_b, Ω_b and the energy of the leptons E_l and the neutrinos momentum components $p_{x,y,z}$:

$$\begin{aligned} m^2_{l\nu_l b} &= (p_l + p_{\nu_l} + p_b)^2 \\ &= m_l^2 + m_{\nu_l}^2 + m_b^2 \\ &\quad +2E_l E_{\nu_l} - 2|\vec{p}_l||\vec{p}_{\nu_l}|\cos\theta_{l\nu_l} + 2E_l E_b - 2|\vec{p}_l||\vec{p}_b|\cos\theta_{lb} + 2E_{\nu_l}E_b - 2|\vec{p}_{\nu_l}||\vec{p}_b|\cos\theta_{\nu_l b} \\ &\approx m_b^2 + 2E_l E_{\nu_l}(1-\cos\theta_{l\nu_l}) \\ &\quad +2E_l E_b\left(1 - \frac{|\vec{p}_b|}{E_b}\cos\theta_{lb}\right) + 2E_{\nu_l}E_b\left(1 - \frac{|\vec{p}_b|}{E_b}\cos\theta_{\nu_l b}\right) \end{aligned} \tag{A.4}$$

where the neutrinos energy is given by $E_{\nu_l} = \sqrt{p^2_{x_{\nu_l}} + p^2_{y_{\nu_l}} + p^2_{z_{\nu_l}}}$ and the masses of the leptons are neglected.

A.2. Neutrino Momentum Solutions

The neutrino p_z is only quadratically constrained by the W boson mass from which follows that two neutrino p_z solutions are equivalent. They can be calculated by

$$\begin{aligned} m_W^2 &= (p_l + p_{\nu_l})^2 = 2E_l|\vec{p}_{\nu_l}| - 2\vec{p}_l \cdot \vec{p}_{\nu_l} \\ \underbrace{m_W^2 + 2\vec{p}_{T_l}\cdot\vec{p}_{T_{\nu_l}}}_{\alpha} &= 2E_l|\vec{p}_{\nu_l}| - 2p_{z_l}p_{z_{\nu_l}} \\ \alpha^2 + 4p_{z_l}p_{z_{\nu_l}}\alpha + 4p^2_{z_l}p^2_{z_{\nu_l}} &= 4E_l^2(\vec{p}^{\,2}_{T_{\nu_l}} + p^2_{z_{\nu_l}}) \\ \underbrace{\left(p^2_{z_l} - E_l^2\right)}_{a} p^2_{z_{\nu_l}} + \underbrace{p_{z_l}\alpha}_{b} p_{z_{\nu_l}} + \underbrace{\frac{\alpha^2}{4} - E_l^2\vec{p}^{\,2}_{T_{\nu_l}}}_{c} &= 0 \\ \Rightarrow p^{1,2}_{z_{\nu_l}} &= -\frac{b}{2a} \pm \sqrt{\frac{b^2}{4a^2} - \frac{c}{a}}\ . \end{aligned} \tag{A.5}$$

The W boson mass constraint pushes the parameters to one of these solutions, but has no sensitivity on the choice of the two p_z solution. Only the top mass constraint leads then to different likelihood values for the two solutions. Since the returned likelihood depends on the simultaneously varied parameters and the measured values which partly have large uncertainties, it is not unlikely that the wrong minimum is chosen in the minimizing procedure.

A.3. Derivation of the Momentum Resolution of Particle Tracks

The momentum resolution due to the spatial uncertainty of particle tracks can be obtained via the determination of the sagitta of the curved trajectory (Fig. A.1).
The sagitta s is calculated by [53]

$$\cos\frac{\vartheta}{2} = \frac{r-s}{r} \Leftrightarrow s = r\left(1 - \cos\frac{\vartheta}{2}\right)\ , \tag{A.6}$$

where r is the radius of the curvature and ϑ is the deflection angle. With simple trigonometric relations this yields to

$$s = 2r\sin^2\frac{\vartheta}{4} \approx \frac{r\vartheta^2}{8}\ , \tag{A.7}$$

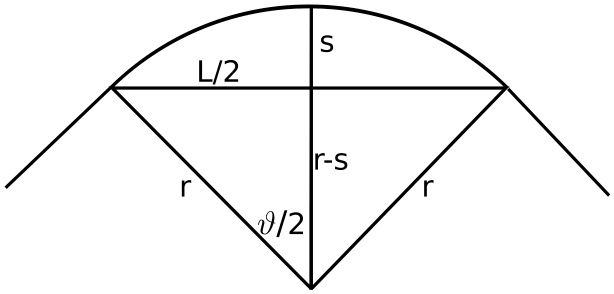

Figure A.1.: Illustration of the sagitta method in order to determine the particle momentum

the last approximation can be made because $\vartheta \ll 1$. Within the magnetic field B the Lorentz force equals the centrifugal force of the particle with mass m, charge e, velocity v and momentum $p = mv$:

$$\frac{mv^2}{r} = evB \Leftrightarrow r = \frac{p}{eB} \tag{A.8}$$

Generally the length L of the magnetic field is much larger than the radius r of the curvature, so the approximation

$$\vartheta \approx \frac{L}{r} = \frac{LeB}{p} \tag{A.9}$$

holds. With Equations A.8 and A.9 the sagitta s of Equation A.7 is determined by

$$s = \frac{eBL^2}{8p} = 0.3\frac{BL^2}{8p} \ , \tag{A.10}$$

where the last equation hold if B is given in Tesla, r in meter and p in GeV/c. Because the uncertainty of the sagitta $\sigma(s)$ can be obtained for N equidistant tracks with the same spatial uncertainty $\sigma(x)$ by

$$\sigma^2(s) = \frac{1}{N-1}\sum_{i=1}^{N}\sigma^2(x) \tag{A.11}$$

and because

$$\frac{\sigma(p)}{p} = \frac{\sigma(s)}{s} \tag{A.12}$$

it was shown by Glückstern [54] that the momentum resolution finally is given by

$$\frac{\sigma(p)}{p} = \frac{\sigma(x)\cdot p}{0.3\cdot L^2\cdot B}\sqrt{\frac{720}{N+4}} \ , \tag{A.13}$$

where $\sigma(x)$ is the spatial uncertainty, L the length of the track, B the magnetic field of the solenoid and N the number of measured track points.

B. Transfer Functions

In the following a few additional transfer functions of the electron (Fig. B.1), light quark (Fig. B.2) and b-quark (Fig. B.3) are shown for various energy and η intervals in order to get a better impression of the shape of the objects' energy resolutions [71].

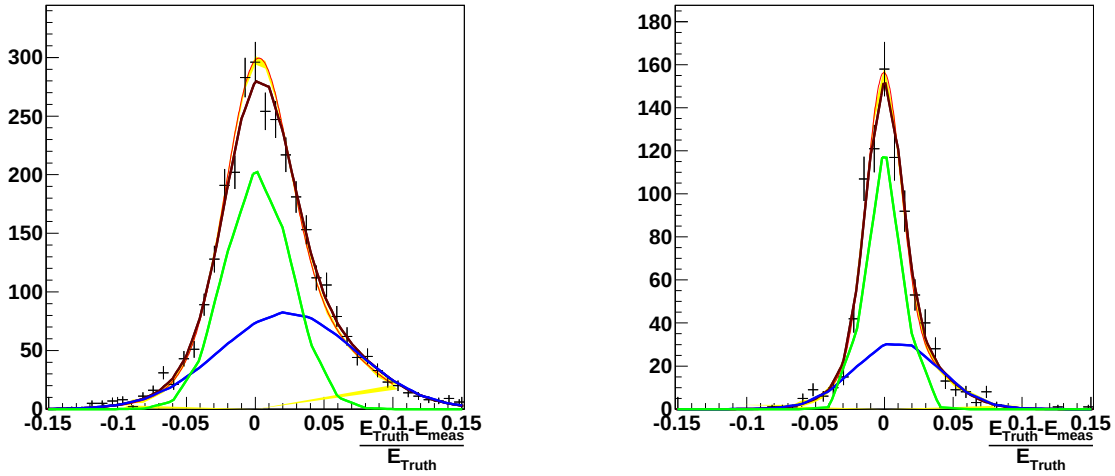

(a) Transfer function of light quark in $1.0 < \eta < 1.7$ and energy 69 GeV < E < 82 GeV

(b) Transfer function of electron in $1.7 < \eta < 2.5$ and energy 262 GeV < E < 288 GeV

Figure B.1.: In both plots the parametrization with a double Gaussian (brown), its subcomponents divided into the two Gaussians (green, blue) and the global fit (red) with error band (yellow) of the transfer function can be seen.

After fitting the energy resolutions in the specific energy and η bins, the obtained parameters are plotted versus the truth energy for all η ranges. The global fits of the parameter p_i are shown in the following plots for electrons (Fig. B.4), light quarks (Fig. B.5) and b-quarks (Fig. B.6) in some selected η intervals. As one can see not all parameters are sufficiently well fitted. Ongoing studies aim to optimize the fitting model and the binning of the energy and η intervals.

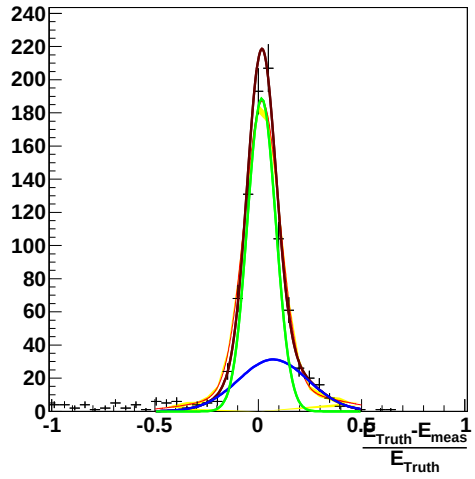

(a) Transfer function of light quark in $1.0 < \eta < 1.7$ and energy 250 GeV < E < 280 GeV

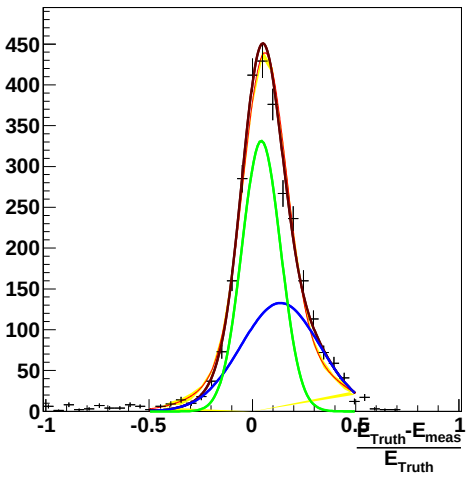

(b) Transfer function of b-quark in $1.7 < \eta < 2.5$ and energy 144 GeV < E < 174 GeV

Figure B.2.: In both plots the parametrization with a double Gaussian (brown), its subcomponents divided into the two Gaussians (green, blue) and the global fit (red) with error band (yellow) of the transfer function can be seen.

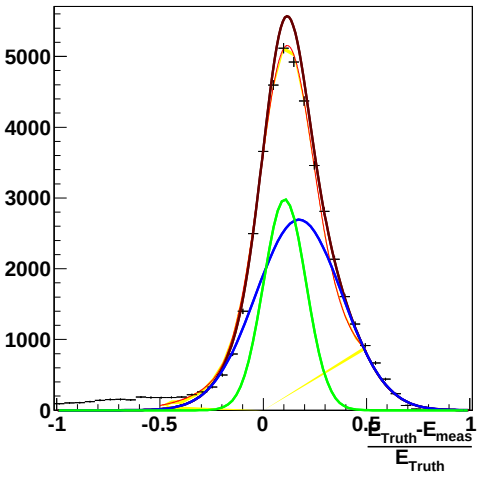

(a) Transfer function of light quark in $0 < \eta < 1.0$ and energy 38 GeV < E < 55 GeV

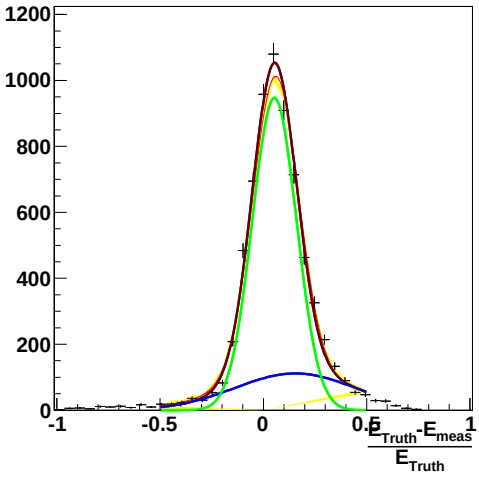

(b) Transfer function of b-quark in $1.0 < \eta < 1.7$ and energy 101 GeV < E < 130 GeV

Figure B.3.: In both plots the parametrization with a double Gaussian (brown), its subcomponents divided into the two Gaussians (green, blue) and the global fit (red) with error band (yellow) of the transfer function can be seen.

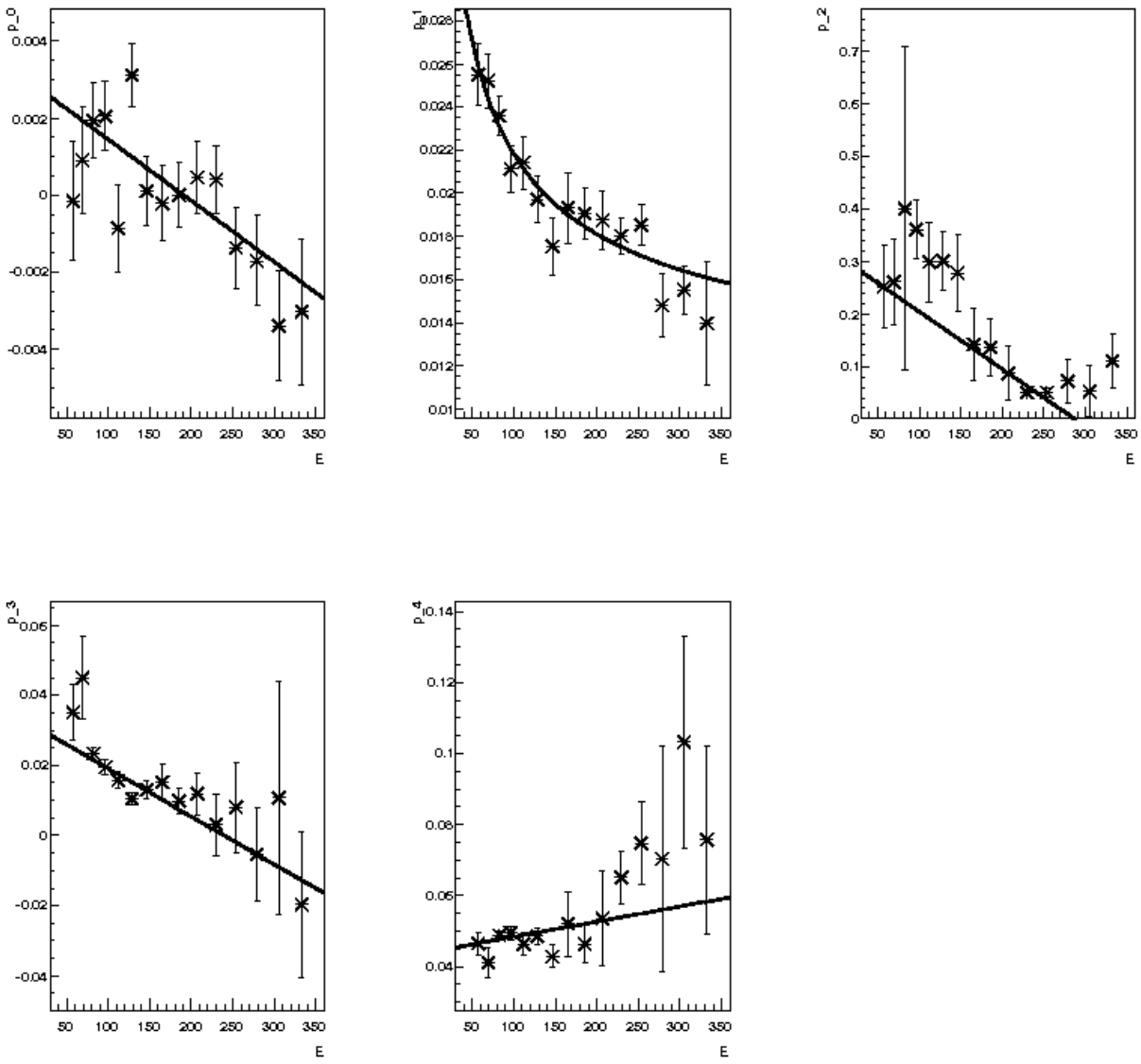

Figure B.4.: The parameters p_i for the electrons transfer function in $1.0 < \eta < 1.7$ depending on the truth energy are shown with the global fit.

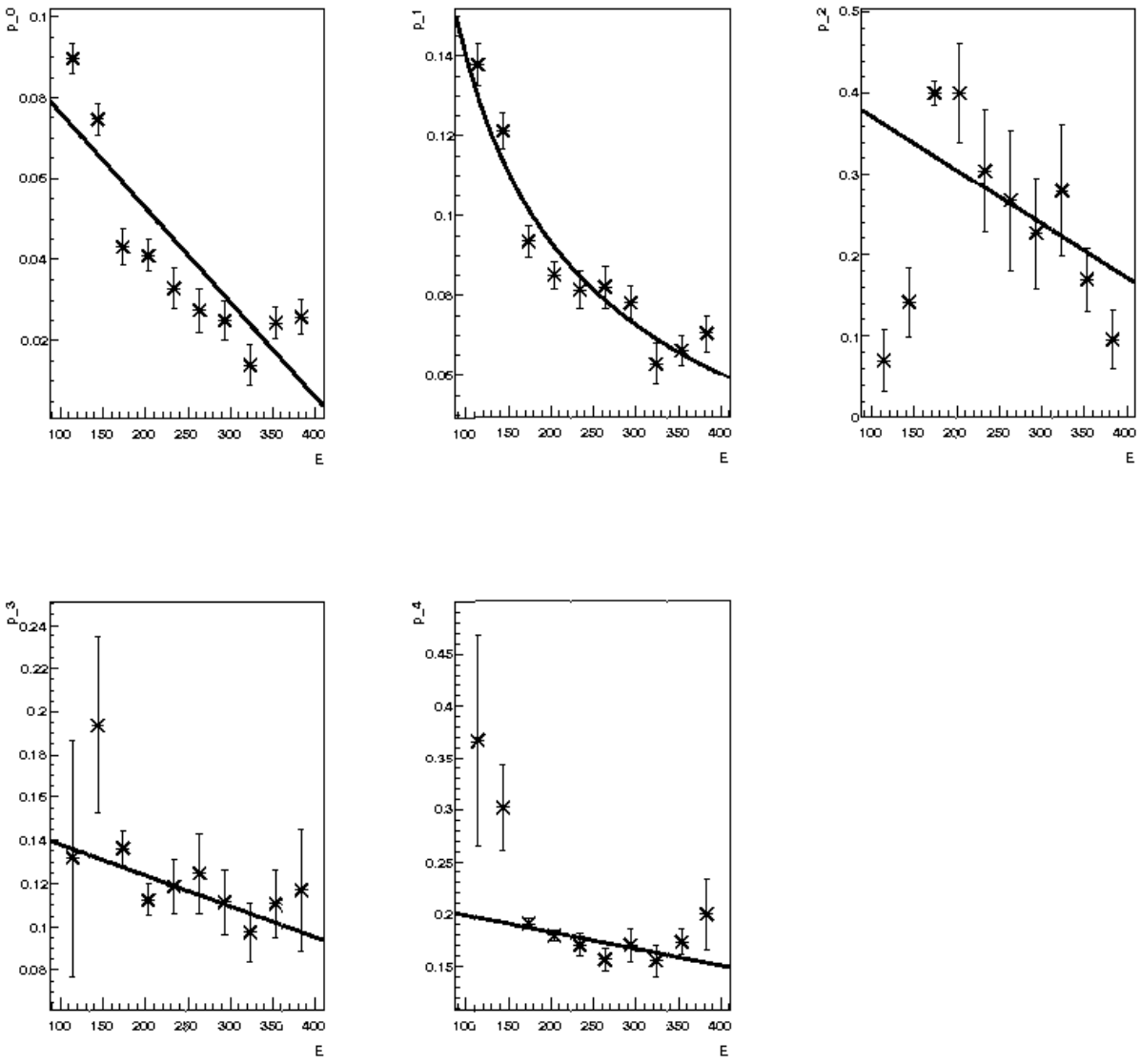

Figure B.5.: The parameters p_i for the light quarks transfer function in $1.7 < \eta < 2.5$ depending on the truth energy are shown with the global fit.

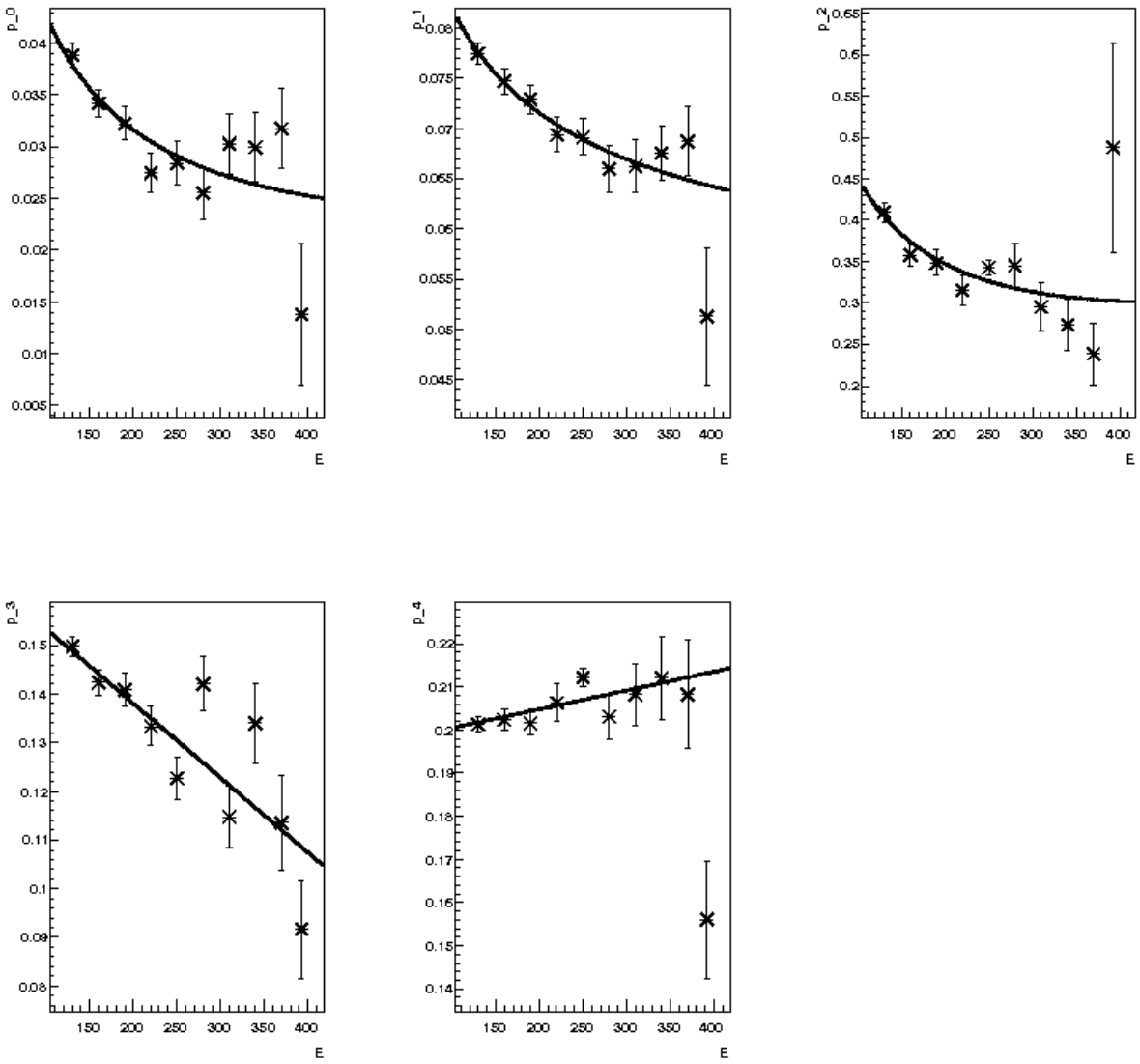

Figure B.6.: The parameters p_i for the b-quarks transfer function in $0 < \eta < 1.0$ depending on the truth energy are shown with the global fit.

C. Supplementary Performance Plots

In the following some plots are shown which supplement the performance studies of the KLFitter.

C.1. Different Jet Multiplicities

There is no visible differences in the ϕ distribution of the top quarks if four, five or six jets are considered in the kinematic fit of six jet events. In any case the distributions match within relative deviations of 20 % the MC truth information

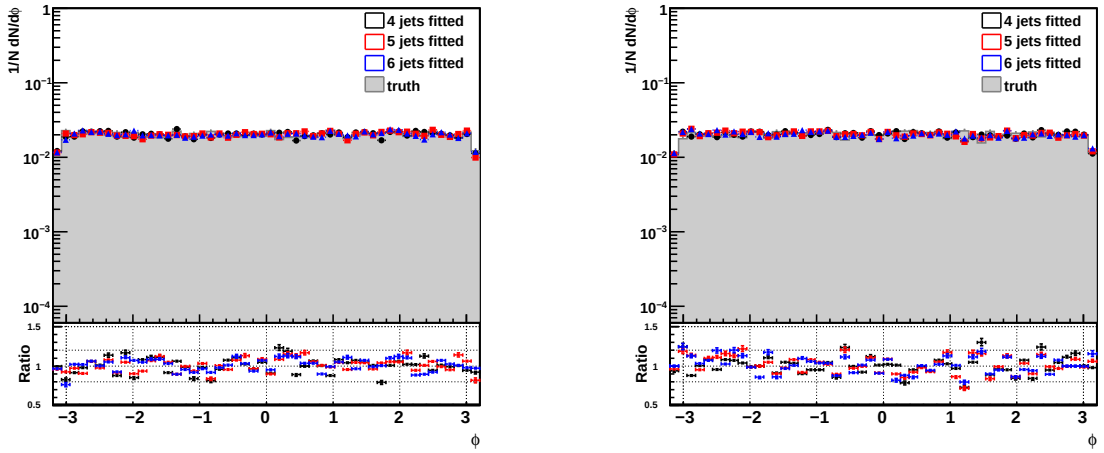

(a) hadronically decaying top quark

(b) leptonically decaying top quark

Figure C.1.: The ϕ-distributions of the hadronically and leptonically decaying top systems with 6 jets in the event are shown. Either four (black), five (red) or six (blue) jets are selected for the fit and are permuted. The distributions are compared to MC truth information (gray shaded) in a ratio plot of reconstructed over true value.

C.2. $W \to e\nu +$ jets Background

The ϕ distributions of the top quarks obtained with $W + 4$ jets background events differ not significantly from the signal distribution. Although compared to MC truth information the relative differences are on average larger no qualitative statement can be made because the statistical error for the background events is much larger.

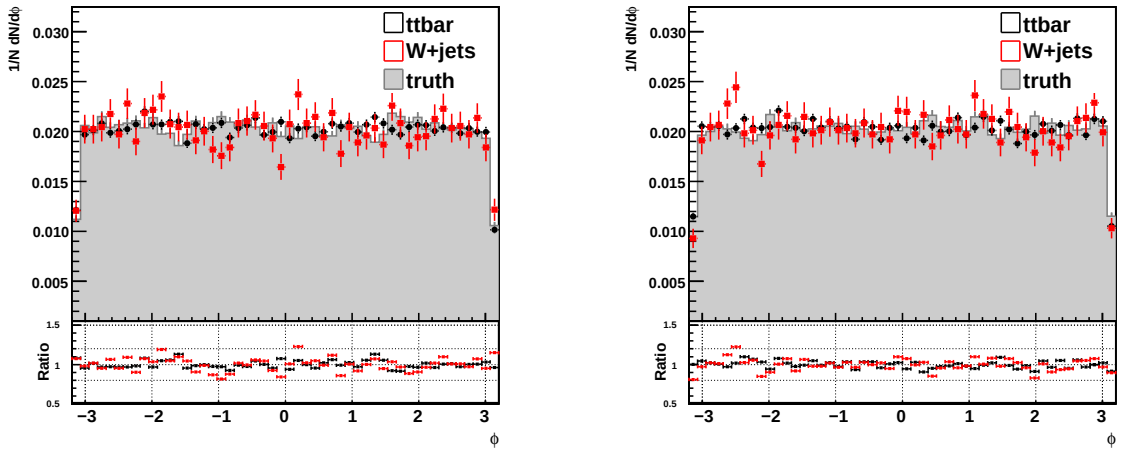

(a) hadronically decaying top quark

(b) leptonically decaying top quark

Figure C.2.: The ϕ-distributions of the hadronically and leptonically decaying top systems, reconstructed either from signal or background, are shown. The distributions are compared to MC truth information (gray shaded) from the signal sample in a ratio plot of reconstructed over true value.

Bibliography

[1] D. Griffiths, *Introduction to Elementary Particles*, WILEY-VCH Verlag, (2008).

[2] The Super-Kamiokande Collaboration, Y. Ashie et al., *Evidence for an oscillatory signature in atmospheric neutrino oscillation*, Physical Review Letters **93** (2004) 101801, `hep-ex/0404034`.

[3] M. C. Gonzalez-Garcia and Y. Nir, *Developments in neutrino physics*, Rev. Mod. Phys. **75** (2003) 345, `hep-ex/0202058`.

[4] C. Amsler et al., *Review of Particle Physics*, Physics Letters B667, 1 (2008), `arXiv:physics.data-an/0808.2552v1`.

[5] C. Berger, *Elementarteilchenphysik*, Springer-Verlag, (2006).

[6] M. Gell-Mann, P. Ramond and R. Slansky, *Supergravity* (1980) 315.

[7] T. Yanagida, *in Proceedings of the Workshop on the Unified Theory and the Baryon Number in the Universe* (1979) 95.

[8] S. L. Glashow, *The future of elementary particle physics*, Plenum Press (1980) 687.

[9] H. Weyl, *The Classical Groups: Their Invariants and Representations*, Westview Press, (1995).

[10] M. W. Peskin and D. V. Schroeder, *An Introduction to Quantum Field Theory*, Princeton University Press, (1997).

[11] F. Halzen, A. D. Martin, *Quarks & Leptons*, John Wiley & Sons, (1984).

[12] P. W. Higgs, *Broken Symmetries, Massless Particles and Gauge Fields*, Phys. Rev. Lett. **12** (1964) 132.

[13] P. W. Higgs, *Broken Symmetries and the Masses of Gauge Bosons*, Phys. Rev. Lett. **13(16)** (1964) 508.

[14] P. W. Higgs, *Spontaneous Symmetry Breakdown without Massless Bosons*, Phys. Rev. Lett. **145** (1966) 1156.

[15] Electroweak Working Group et al, *Precision Electroweak Measurements and Constraints on the Standard Model* (2009), `hep-ex/0911.2604`.

[16] M. Peskin, Nature **419** (2002) 24.

[17] F. Zwicky, Helvetica Physics Acta **6** (1933) 124.

[18] M. S. Turner and D. Huterer, Journal of the Physical Society of Japan **76** (2007) 111015.

[19] G. Ross, *Grand Unified Theories*, Perseus, Reading (1985).

[20] P. H. Chankowski et al., *Cosmological fine tuning, supersymmetry and the gauge hierarchy problem*, Phys. Lett. B **452** (1998) 28.

[21] The Tevatron Electroweak Working Group for the CDF and DØ Collaborations, *Combination of CDF and DØ Results on the Mass of the Top Quark* (2009), hep-ex/0903.2503.

[22] S. Abachi et al., The DØ Collaboration, *Observation of the Top Quark*, Phys. Rev. Lett. **74** (1995) 2632, hep-ex/9503003.

[23] F. Abe et al., The CDF Collaboration, *Observation of Top Quark Production in $p\bar{p}$ Collision with Collider Detector at Fermilab*, Phys. Rev. Lett. **74** (1995) 2626, hep-ex/9503002.

[24] M. Kobayashi and T. Maskawa, *CP-Violation in the Renormalizable Theory of Weak Interaction*, Progress of Theoretical Physics **49** (1973) 652.

[25] S.W. Herb et al., *Observation of Dimuon Resonance at 9.5 GeV in 400-GeV Proton-Nucleus Collisions*, Physical Review Letters **39** (1977) 252.

[26] V.M. Abazov et al. for the DØ Collaboration , *Experimental Discrimination between Charge 2e/3 Top Quark and Charge 4e/3 Exotic Quark Production Scenarios*, Phys. Rev. Lett. **98** (2007) 041801.

[27] Z. Gunay Unalan and the CDF Collaboration, *First CDF Measurement of the Top Quark Charge using the Top Decay Products*, Nucl. Phys. Proc. Suppl. **297** (2008) 177.

[28] CDF Collaboration, *Measurement of the Top Quark Charge with Soft Lepton Tags*, CDF conference note **9939** (2010).

[29] The CDF Collaboration, *A Measurement of $t\bar{t}$ Spin Correlations Coefficient in* 2.8 fb^{-}1 *Dilepton Candidates*, CDF conference note **9824** (2009).

[30] The DØ Collaboration, *Spin correlations in $t\bar{t}$ production in dilepton final states*, DØ conference note **5950** (2009).

[31] G. L. Kane, G. A. Ladinsky, C.-P. Yuan, *Using the top quark for testing standard-model polarization and CP predictions*, Phys. Rev. **D45** (1992) 124.

[32] J. Pumplin, D. R. Stump, J. Huston, H. L. Lai, P. Nadolsky, W. K. Tung, *New Generation of Parton Distributions with Uncertainties from Global QCD Analysis* (2002), hep-ph/0201195.

[33] S. Moch and P. Uwer, *Heavy-quark pair production at two loops in QCD*, Nucl. Phys. Proc. Suppl. **183** (2008) 75, hep-ph/arXiv:0807.2794v1.

[34] The CDF Collaboration, *Measurement of the $t\bar{t}$ production cross section in $p\bar{p}$ collisions at $\sqrt{s}$ = 1.8 TeV*, Phys. Rev. D **67** (2003) 119901, arXiv:hep-ex/0101036.

[35] The CDF Collaboration, *Combination of CDF top quark pair production cross section measurements with up to* 4.6 fb^{-1}, CDF conference note **9913** (2009).

[36] The DØ Collaboration, *$t\bar{t}$ production cross-section in $p\bar{p}$ collisions at $\sqrt{s}$ = 1.8 TeV*, Phys. Rev. D **67** (2003) 012004, arXiv:hep-ex/0205019.

[37] The DØ Collaboration, *Combination of ttbar cross section measurements and constraints on the mass of the top quark and its decays into charged Higgs bosons*, Phs. Rev. D **80** (2009) 071102, arXiv:hep-ex/0903.5525.

[38] M. Cacciari, S. Frixione, M. L. Mangano, P. Nason and G. Ridolfi, *The t anti-t cross-section at 1.8-TeV and 1.96-TeV: A study of the systematics due to parton densities and scale dependence*, JHEP **0404** (2004) 068, arXiv:hep-ex/0303085.

[39] R. Bonciani, S. Catani, M. L. Mangano and P. Nason, *NLL resummation of the heavy-quark hadroproduction cross-sectione*, Nucl. Phys. B **529** (1998) 424, arXiv:hep-ex/9801375.

[40] V. M. Abazov et al., *Observation of Single Top Quark Production*, Phys. Rev. Lett. **103** (2009) 092001, hep-ex/0903.0850.

[41] T. Aaltonen et al., The CDF Collaboration, *First Observation of Electroweak Single Top Quark Production*, Phys. Rev. Lett. **103** (2009) 092002, hep-ex/0903.0885.

[42] Tevatron Electroweak Working Group for the CDF Collaboration, the DØ Collaboration, *Combination of CDF and DØ Measurements of the Single Top Production Cross Section* (2009), arXiv:0908.2171v1 [hep-ex].

[43] T. Aaltonen et al., The CDF Collaboration, *Observation of Single Top Quark Production and Measurement of Vtb with CDF*, Phys. Rev. D (2010), arXiv:1004.1181v1 [hep-ex].

[44] B. Clement et al., *Search for Single-Top Events at 10 TeV in ATLAS at the LHC*, ATL-COM-PHYS-2009-572 (2010).

[45] L. Evans, P. Bryant et al., *LHC Machine*, JINST **3** (2008) S08001.

[46] The ATLAS Collaboration, *ATLAS Detector and Physics Peformance Technical Design Report* **1** (1999).

[47] The LHCf Collaboration, *Technical Proposal for the CERN LHCf Experiment* (2005).

[48] The CMS Collaboration, *CMS Physics Technical Design Report* **1** (2006).

[49] The TOTEM Collaboration, *TOTEM Technical Design Report* (2004).

[50] The ALICE Collaboration, *Technical Proposal for A Large Ion Collider Experiment at the CERN LHC* (1995).

[51] The LHCb Collaboration, *LHCb Technical Proposal* (1998).

[52] G. Aad et al., *The ATLAS Experiment at the CERN Large Hadron Collider*, JINST **3** (2008) S08003.

[53] C. Grupen, *Teilchendetektoren*, BI Wissenschaftsverlag, (1993).

[54] R. L. Glückstern, *Uncertainties in Track Momentum and Direction due to Multiple Scattering and Measurement Errors*, Nucl. Instrum. Methods **24** (1963) 381.

[55] L. Lyons, *Statistics for nuclear and particle physicists*, Cambridge Univ. Press, (1986).

[56] R. Barlow, *Statistics*, John Wiley & Sons, (1989).

[57] M. Stein, *Kinematic Fit of $t\bar{t}$ Events in the Semi-Leptonic Decay Channel with a χ^2 Method at the ATLAS Experiment*, Diploma thesis - University of Göttingen (2008).

[58] J. Erdmann, K. Kröninger, O. Nackenhorst and A. Quadt, *Kinematic fitting of ttbar-events using a likelihood approach: The KLFitter package*, ATL-COM-PHYS-2009-551 (2009).

[59] R. Brun, F. Rademakers, P. Canal, I. Antcheva and D. Buskulic, *ROOT - An Object-Orientated Data Analysis Framework*, Users Guide 5.26 (December 2009), `http://root.cern.ch`.

[60] A. Caldwell, D. Kollar and K. Kröninger, *BAT - The Bayesian Analysis Toolkit*, `arXiv:physics.data-an/0808.2552v1`.

[61] F. James and M. Roos, *Minuit: A System for Function Minimization and Analysis of the Parameter Errors and Correlations*, Comput. Phys. Community **10** (1975) 343.

[62] B. Abbott et al., *Study on reconstructed object definition and selection for top physics*, ATL-COM-PHYS-2009-633 (2009).

[63] S. Frixione, P. Nason, B. R. Webber , *Matching NLO QCD and parton showers in heavy flavour production*, JHEP **08** (2003) 007, `hep-ph/0305252`.

[64] M. Bosman, R. Hawkings, A. Shibata, U. Husemann, *Understanding Monte Carlo Generators for Top Physics*, ATL-COM-PHYS-2009-334 (2009).

[65] J. M. Butterworth, J.R. Forshaw, M.H. Seymour, *Multiparton interactions in photoproduction at HERA* (1996), `hep-ph/9601371`.

[66] G. Corcella, I. G. Knowles, G. Marchesini, S. Moretti, K. Odagiri, P. Richardson, M. H. Seymour, B. R. Webber, *Herwig 6.5: an event generator for Hadron Emission Reactions With Interfering Gluons (including supersymmetric processes)*, JHEP **01** (2000) 010, `hep-ph/0011363v3`.

[67] G. Aad et al., The ATLAS Collaboration, *Expected Performance of the ATLAS Experiment - Detector, Trigger and Physics* (2008), `arXiv:0901.0512 [hep-ex]`.

[68] G. C. Blazey et al., *Run II Jet Physics: Proceedings of the Run II QCD and Weak Boson Physics Workshop* (11.02.2010), `arXiv:hep-ex/0005012v2`.

[69] W. Lampl et al., *Calorimeter Clustering Algorithms: Description and Performance*, ATLAS-LARG-PUB-2009-002 (2008).

[70] M. Bunse, *Truth Matching in Tt Events* (11.02.2010), `Talk in the Top Reconstruction Meeting`.

[71] B. Lemmer, *note in preparation*, Göttingen University (2010).

[72] M. Cacciari, G. P. Salam and G. Soyez, *The anti-Kt jet clustering algorithm*, JHEP. **04** (2008) 063, `1126-6708`.

[73] Reconstruction of High Mass $t\bar{t}$ Resonances in the Lepton+Jets Channel, *The ATLAS Collaboration*, ATL-PHYS-PUB-2009-081 (2009).

[74] M. L. Mangano et al., *ALPGEN, a generator for hard multiparton processes in hadronic collisions*, JHEP. **001** (2003) 0307, `hep-ph/0206293`.

[75] J. Alwall et al., *Comparative study of various algorithms for the merging of parton showers and matrix elements in hadronic collisions*, Eur.Phys.J. **C53** (2008) 473, `arXiv:0706.2569v2 [hep-ph]`.

[76] S. Ebert, *BSc. thesis in preparation*, Göttingen University (2010).

[77] P. Stolte, *BSc. thesis in preparation*, Göttingen University (2010).

Acknowledgements

This thesis would not have been possible without the support and guidance of many people to whom I owe my gratitude.

First and foremost I would like to express my gratitude to Prof. Arnulf Quadt for giving me the opportunity to write my diploma thesis in the high energy physics group of the University of Göttingen. His fascinating lectures encouraged me during my studies to get a deeper insight into the exciting field of particle physics. I am grateful for his good advices and suggestions during my research and for him taking time being my academic supervisor and the referee to this thesis. I would also like to show my gratitude to Prof. Ariane Frey for being co-referee to this thesis.

A special thank goes to Dr. Kevin Kröninger for his incredible patience answering all my questions and helping me with technical issues whenever it was necessary. He spent much time discussing my work and guiding me with countless new ideas through the time of my studies. Without his helpful and constructive advises and the time he has taken for proofreading, this thesis would not have been possible. His extraordinary supervision is certainly more than one can expect.

I would especially like to thank Johannes Erdmann, who has made available his support in a number of ways. He has provided continuously help with technical questions and has been open for physics and non-physics discussions at any time, which have helped me to understand the subtleties of some related topics. His extensive assist and proofreading skills contributed to this work.

Furthermore, I would like to thank all members of the HEP group in Göttingen who welcomed me so warmly and created a relaxed atmosphere. Everyone has been exceptionally willing to help whenever possible with any kind of concerns.

I would also like to thank all my friends who helped me to diverse my mind or supported me during the entire time of my studies. I am heartily thankful to my girlfriend Nadja for her patience, sympathy and for understanding me and my character. She always cared about me and cheered me up when I needed it most.

Last but not least, I owe my deepest gratitude to my family not only for any kind of support during my time as a student but especially for their guidance through my life. My parents Rainer and Margrit and my sister Tanja have always been supportive of my enthusiasm for physics and are always there for me if I need help, advise or motivation.